



## 저작자표시-비영리-변경금지 2.0 대한민국

이용자는 아래의 조건을 따르는 경우에 한하여 자유롭게

- 이 저작물을 복제, 배포, 전송, 전시, 공연 및 방송할 수 있습니다.

다음과 같은 조건을 따라야 합니다:



저작자표시. 귀하는 원저작자를 표시하여야 합니다.



비영리. 귀하는 이 저작물을 영리 목적으로 이용할 수 없습니다.



변경금지. 귀하는 이 저작물을 개작, 변형 또는 가공할 수 없습니다.

- 귀하는, 이 저작물의 재이용이나 배포의 경우, 이 저작물에 적용된 이용허락조건을 명확하게 나타내어야 합니다.
- 저작권자로부터 별도의 허가를 받으면 이러한 조건들은 적용되지 않습니다.

저작권법에 따른 이용자의 권리는 위의 내용에 의하여 영향을 받지 않습니다.

이것은 [이용허락규약\(Legal Code\)](#)을 이해하기 쉽게 요약한 것입니다.

[Disclaimer](#)

이학박사 학위논문

**Studies on the magnetoelectric effects of the  
Co<sub>2</sub>Y-type hexaferrites**

**Ba<sub>2-x</sub>Sr<sub>x</sub>Co<sub>2</sub>(Fe<sub>1-y</sub>Al<sub>y</sub>)<sub>12</sub>O<sub>22</sub> and 2D van der  
Waals materials CuCrP<sub>2</sub>X<sub>6</sub> (X=S and Se)**

Co<sub>2</sub>Y-타입 육방정계 철산화물 Ba<sub>2-x</sub>Sr<sub>x</sub>Co<sub>2</sub>(Fe<sub>1-y</sub>Al<sub>y</sub>)<sub>12</sub>O<sub>22</sub>과  
이차원 반데르발스 물질 CuCrP<sub>2</sub>X<sub>6</sub> (X=S, Se)의  
자기전기효과에 관한 연구

2020 년 7 월

서울대학교 대학원

물리천문학부

박 창 배

**Studies on the magnetoelectric effects of the Co<sub>2</sub>Y-type  
hexaferrites Ba<sub>2-x</sub>Sr<sub>x</sub>Co<sub>2</sub>(Fe<sub>1-y</sub>Al<sub>y</sub>)<sub>12</sub>O<sub>22</sub> and 2D van der Waals  
materials CuCrP<sub>2</sub>X<sub>6</sub> (X=S and Se)**

**Co<sub>2</sub>Y-타입 육방정계 철산화물 Ba<sub>2-x</sub>Sr<sub>x</sub>Co<sub>2</sub>(Fe<sub>1-y</sub>Al<sub>y</sub>)<sub>12</sub>O<sub>22</sub>과  
이차원 반데르발스 물질 CuCrP<sub>2</sub>X<sub>6</sub> (X=S, Se)의  
자기전기효과에 관한 연구**

지도교수 김 기 훈

이 논문을 이학박사 학위논문으로 제출함

2020 년 7 월

서울대학교 대학원

물리천문학부

박 창 배

박창배의 이학박사 학위논문을 인준함

2020 년 6 월

위 원 장 박 제 근

부 위 원 장 김 기 훈

위 원 노 태 원

위 원 이 진 호

위 원 박 재 훈

(인)  
(인)  
(인)  
(인)  
(인)

**Studies on the magnetoelectric effects of the  
Co<sub>2</sub>Y-type hexaferrites  
Ba<sub>2-x</sub>Sr<sub>x</sub>Co<sub>2</sub>(Fe<sub>1-y</sub>Al<sub>y</sub>)<sub>12</sub>O<sub>22</sub> and 2D van der  
Waals materials CuCrP<sub>2</sub>X<sub>6</sub> (X=S and Se)**

Chang Bae Park

Supervised by  
Professor Kee Hoon Kim

A Dissertation Submitted to the Faculty of  
Seoul National University  
in Partial Fulfillment of the Requirements for  
the Degree of Doctor of Philosophy

July 2020

*Department of Physics and Astronomy  
Graduate School  
Seoul National University*



# Contents

List of Figures	v
List of Tables	xv
Abstract	xvi
<b>1 Introduction</b>	<b>1</b>
1.1 Types of multiferroics . . . . .	3
1.1.1 Type-I multiferroics . . . . .	3
1.1.2 Type-II multiferroics . . . . .	4
1.2 The origins of spin-induced ferroelectricity . . . . .	5
1.2.1 Exchange striction model . . . . .	5
1.2.2 Spin current model . . . . .	6
1.2.3 Spin-dependent $p$ - $d$ hybridization model . . . . .	7
1.3 Outline of Thesis . . . . .	9
<b>2 Experimental Methods</b>	<b>11</b>
2.1 Single crystal growth . . . . .	12
2.1.1 Flux method . . . . .	12
2.1.2 Thermal annealing . . . . .	13
2.1.3 Chemical vapor transport method . . . . .	15

2.2	Measurements . . . . .	16
2.2.1	Magnetization . . . . .	16
2.2.2	Dielectric constant . . . . .	17
2.2.3	Direct magnetoelectric effect . . . . .	18
2.2.4	Converse magnetoelectric effect . . . . .	20
<b>3</b>	<b>Co<sub>2</sub>Y-type hexaferrites Ba<sub>2-x</sub>Sr<sub>x</sub>Co<sub>2</sub>(Fe<sub>1-y</sub>Al<sub>y</sub>)<sub>12</sub>O<sub>22</sub></b>	<b>21</b>
3.1	Introduction . . . . .	21
3.2	Experimental results . . . . .	25
3.2.1	Crystallographic structure of Co <sub>2</sub> Y-type hexaferrites . . . . .	25
3.2.2	Enhancement of magnetoelectric coupling by the Sr and Al substitution . . . . .	27
3.2.3	The metastability of the transverse conical state . . . . .	33
3.2.4	Magnetic properties of Co <sub>2</sub> Y-type hexaferrites . . . . .	39
3.2.5	Ferroelectricity and its phase diagram . . . . .	45
3.2.6	Observation of converse ME effect . . . . .	46
3.3	Discussion . . . . .	52
3.4	Conclusion . . . . .	56
<b>4</b>	<b>2D van der Waals materials CuCrP<sub>2</sub>X<sub>6</sub> (X=S and Se)</b>	<b>57</b>
4.1	Introduction . . . . .	57
4.2	Experimental results . . . . .	61
4.2.1	The growth of single crystals . . . . .	61
4.2.2	Crystallographic structure of CuCrP <sub>2</sub> X <sub>6</sub> . . . . .	62
4.2.3	Magnetic properties in CuCrP <sub>2</sub> S <sub>6</sub> . . . . .	64
4.2.4	Magnetoelectric properties in CuCrP <sub>2</sub> S <sub>6</sub> . . . . .	67
4.3	Discussion . . . . .	71

4.3.1	The mechanism of ME coupling in $\text{CuCrP}_2\text{S}_6$ . . . . .	71
4.3.2	Symmetry analysis in $\text{CuCrP}_2\text{S}_6$ . . . . .	76
4.4	Conclusion . . . . .	79
<b>5</b>	<b>Summary and conclusion</b>	<b>80</b>
<b>6</b>	<b>References</b>	<b>82</b>
<b>7</b>	<b>Appendix</b>	<b>89</b>
7.1	The additional experiments on the series of the $\text{Co}_2\text{Y}$ -type hexa- ferrites . . . . .	89
7.1.1	Direct ME coupling in the $\text{Ba}_{2-x}\text{Sr}_x\text{Co}_2(\text{Fe}_{1-y}\text{Al}_y)_{12}\text{O}_{22}$ ( $y$ $= 0.04$ and $0.08$ ) series . . . . .	89
7.1.2	Magnetostriction of the $\text{Co}_2\text{Y}$ -type hexaferrites . . . . .	91
7.1.3	Electric polarization along $c$ -axis induced by the exchange striction mechanism . . . . .	93
7.2	Studies on the ME coupling in the $\text{CoZnY}$ -type hexaferrites single crystal . . . . .	97
7.3	Studies on the ME coupling in the $\text{Co}_2\text{Z}$ -type hexaferrites $\text{Ba}_{3-x}\text{Sr}_x\text{Co}_2\text{Fe}_{24}\text{O}_{41}$ poly crystals . . . . .	99
7.4	Studies on the hybrid improper ferroelectricity in $(\text{Ba},\text{Sr},\text{Ca})_3\text{Sn}_2\text{O}_7$	103
7.5	Investigation of the topological quantum state via lithium interca- lation in a 2D ferromagnet $\text{CrSiTe}_3$ . . . . .	109
7.5.1	Sample preparation . . . . .	110
7.5.2	Metal-insulator transition under high pressure . . . . .	114
7.6	The preparation of X-ray diffraction at low temperature . . . . .	116

<b>8</b>	<b>Publication List</b>	<b>120</b>
8.1	List of publications . . . . .	120
<b>9</b>	<b>Korean abstract</b>	<b>122</b>
<b>10</b>	<b>Acknowledgements</b>	<b>125</b>

# List of Figures

1.1	Schematic diagram of (a) multiferrics and (b) magnetoelectric coupling. . . . .	1
1.2	(a) The chain with spin $\uparrow\uparrow\downarrow\downarrow$ configuration. Arrows indicates the spin direction. Blue and red spheres depict two different magnetic atoms A and B with charge $Q_A$ and $Q_B$ , respectively. (b) The emergence of electric polarization by exchange striction mechanism. . . . .	6
1.3	(a) The spin chain with the spiral spin ordering. Blue arrows indicate the spin direction. Blue and red spheres indicates magnetic and oxygen ions, respectively. $\vec{e}$ is an unit vector parallel to the direction of spin propagation and $\vec{x}$ is a displacement vector of oxygen ion from the the center of the line connecting to two neighboring magnetic ions. . . . .	7
1.4	The selected non-collinear spin structures and application of the spin current model. . . . .	8
1.5	Schematic illustration of $p$ - $d$ hybridization when (a) the spin is perpendicular to the bonding direction and (b) parallel to the bonding direciton. Blue arrows indicate the spin direction. The blur blue and red areas represent the $d$ - and $p$ - orbitals of magnetic ions and ligand ions, respectively. $e_{il}$ is along bonding direction. . . . .	9

2.1	The temperature sequence to grow Co <sub>2</sub> Y-type single crystals. . . .	13
2.2	The picture of the chamber for annealing in high pressure . . . . .	14
2.3	The resistivity as a function of temperature after the thermal an- nealing under oxygen atmosphere. . . . .	14
2.4	The schematic illustration of chemical vapor transport method. . .	15
2.5	Magnetization curve of the standard palladium sample to calibrate the magnetic field near zero field. . . . .	16
2.6	The schematic picture of magnetoelectric current measurement. . .	19
3.1	Summary of $dP/dH$ in various Y-type hexaferrites single crystal and poly crystal [52, 55–57]. . . . .	23
3.2	The crystal structure of Co <sub>2</sub> Y-type hexaferrites (left) and a zoomed- up structure around the interface of the magnetic blocks (right). Both Fe and Co ions are located in the center of the oxygen octa- hedra or tetrahedra. Orange and blue colors represent the Fe or Co ions located in the magnetic $L$ and $S$ blocks, respectively while purple spheres represent the Ba or Sr sites. The yellow triangle indicates the geometrical spin frustration related to helical spin ordering in the Co <sub>2</sub> Y-type hexaferrites. . . . .	25
3.3	(a) An X-ray diffraction pattern of the ground Ba <sub>0.2</sub> Sr <sub>1.8</sub> Co <sub>2</sub> Fe <sub>12</sub> O <sub>22</sub> single crystal powder and its Rietveld refinement result, which ver- ifies the $R\bar{3}m$ structure. (b) The evolution of $a$ - and $c$ -axes lattice constants with Sr ( $x$ ) and Al ( $y$ ) substitution ratios as determined from the X-ray diffraction data and the Rietveld refinement result.	27
3.4	(a) Electric-field poling $E_P$ dependence of polarization at 10 K. (b) Summary of the polarization at 10 K, 100 K, and 200 K. . . . .	28

3.5	(a) Magnetic-field dependent electric polarization of $\text{Ba}_{2-x}\text{Sr}_x\text{Co}_2(\text{Fe}_{1-y}\text{Al}_y)_{12}\text{O}_{22}$ single crystals. $\Delta P_{max}$ indicates the difference between extreme values, $P_{max}-P_{min}$ . Electric polarization is calculated from the integration of the ME current. (b) Temperature-dependence of $\Delta P_{max}$ and maximum $dP/dH$ values. (c) Summary of $\Delta P_{max}$ and maximum $dP/dH$ as a function of $y$ at 10 K and 300 K, demonstrating that the specimen with $x = 1.8$ and $y = 0.04$ has the largest magnetic field induced polarization at both temperatures.	30
3.6	(up) ME current and (down) electric polarization of $x=1.8$ and $y=0.06$ compound at low magnetic field region above 150 K. . . .	32
3.7	A pictorial representation of spin configuration of the $\text{Co}_2\text{Y}$ -type hexaferrites without (left) and with (right) application of an in-plane magnetic field ( $H_{ab}$ ). ALC refers to an alternative conical spin ordering pattern and TC represents a transverse conical spin ordering pattern. . . . .	34
3.8	In-plane magnetization $M_{ab}$ data of $\text{Ba}_{0.2}\text{Sr}_{1.8}\text{Co}_2(\text{Fe}_{0.96}\text{Al}_{0.04})_{12}\text{O}_{22}$ from 10 K to 350 K measured at 20 mT after field cooling with various magnetic field applications conditions, demonstrating the metastable nature of competing phases in the $\text{Co}_2\text{Y}$ -type hexaferrites. $M_{ab}$ measured during the warming process under the bias magnetic field $\mu_0 H_M = 20$ mT after cooling with finite (FC) and zero (ZFC) magnetic field. . . . .	35
3.9	The $M_{ab}$ for various doping ratio. The red curve and black curves are $M_{ab}$ of $\text{Ba}_{0.2}\text{Sr}_{1.8}\text{Co}_2(\text{Fe}_{1-y}\text{Al}_y)_{12}\text{O}_{22}$ measured under $\mu_0 H_M = 20$ mT during the warming process after various magnetic field applications conditions. . . . .	37

3.10	Pictorial descriptions for a dominant spin configurations and. $L$ and $S$ mean the magnetic $L$ and $S$ blocks as shown in Fig. 3.7. The spin state of $S$ block is omitted for clarity. . . . .	37
3.11	The change of the Bragg peak intensities under warming the sample in zero field after applying 3.0 T along $ab$ -plane at 10 K. . . .	39
3.12	AC ME susceptibility $\alpha_{MES}$ as a function of time under static 9 mT (up) and 1.5 T (down) after the poling procedure. . . . .	40
3.13	Magnetization curve along $ab$ - (orange) and $c$ - (blue) direction measured in the application of $\mu_0 H_M = 20$ mT during the warming process after ZFC. . . . .	42
3.14	Magnetic phase diagram constructed from the magnetization curve. Red arrows represent the spin structures in the phases. Long and short arrows denotes the spin in $L$ and $S$ blocks, respectively. ALC, $ab$ -FiM1, and $c$ -FiM1 phases are painted in green, red, and blue colors to coincide with the Fig. 3.13. The black dashed line denotes the paramagnetic phase for guides to the eye. . . . .	44
3.15	(a) Variation of dielectric constant and electric polarization as a function of magnetic fields at 320 K in the $\text{Ba}_{0.2}\text{Sr}_{1.8}\text{Co}_2(\text{Fe}_{1-y}\text{Al}_y)_{12}\text{O}_{22}$ crystal. (b) Magnetic-field dependent dielectric constant variation at wide temperatures in the same crystal. The red (black) curve was measured while magnetic field is increasing (decreasing). Blue dotted lines are for guides to the eye. . . . .	45
3.16	Phase diagram of $\text{Ba}_{0.2}\text{Sr}_{1.8}\text{Co}_2(\text{Fe}_{0.96}\text{Al}_{0.04})_{12}\text{O}_{22}$ single crystal constructed from the dielectric constant, magnetic field-induced polarization, and magnetization measurement. . . . .	45



3.17	ME current at low magnetic field region in (left) $y = 0.04$ and (right) $y = 0.00$ compounds. . . . .	47
3.18	Phase diagram of $\text{Ba}_{0.2}\text{Sr}_{1.8}\text{Co}_2(\text{Fe}_{1-y}\text{Al}_y)_{12}\text{O}_{22}$ single crystal. . . .	47
3.19	Electric field dependence of magnetization at 0 T and 10 K in $\text{Ba}_{0.2}\text{Sr}_{1.8}\text{Co}_2(\text{Fe}_{0.96}\text{Al}_{0.04})_{12}\text{O}_{22}$ . . . . .	48
3.20	Electric field dependence of magnetization at 0 T in various temperatures in $\text{Ba}_{0.2}\text{Sr}_{1.8}\text{Co}_2(\text{Fe}_{0.96}\text{Al}_{0.04})_{12}\text{O}_{22}$ . . . . .	49
3.21	Electric field dependence of magnetization at 0 T in various temperatures in $\text{Ba}_{0.2}\text{Sr}_{1.8}\text{Co}_2(\text{Fe}_{0.96}\text{Al}_{0.04})_{12}\text{O}_{22}$ . . . . .	50
3.22	The reversal of magnetization by the electric field with finite magnetic field -6 mT in $\text{Ba}_{0.2}\text{Sr}_{1.8}\text{Co}_2(\text{Fe}_{0.96}\text{Al}_{0.04})_{12}\text{O}_{22}$ . . . . .	51
3.23	The profiles of $\Delta M$ vs $E$ in $\text{Ba}_{0.2}\text{Sr}_{1.8}\text{Co}_2(\text{Fe}_{1-y}\text{Al}_y)_{12}\text{O}_{22}$ . . . . .	52
3.24	The reciprocal of $ M_{ab} - M_c /2$ (left tick label) and $(M_{ab} + M_c)/2$ (right tick label) as a function of Al substitution $y$ at 300 K. The reciprocal is taken to each values to emphasize the lowest values in the $y = 0.04$ specimen. . . . .	53
4.1	The image of the grown $\text{CuCrP}_2\text{S}_6$ single crystal. . . . .	61
4.2	XRD peak of $\text{CuCrP}_2\text{S}_6$ indexed by the space group suggested in Ref. [90]. . . . .	62
4.3	(a) The crystal structure of $\text{CuCrP}_2\text{S}_6$ including the six $\text{CrS}_6$ octahedron (blue) and the six $\text{CuS}_3$ triangle (red) below 150 K. $\text{P}^{4+}$ ions (orange) forms pairs. Orange dashed line indicates the NNN interaction $J$ (b) The illustration projected onto $ab$ -plane. It shows the $\text{CuS}_6$ and $\text{CrS}_6$ have honeycomb network (dashed line). . . .	63

4.4	The comparison between $\text{CuCrP}_2\text{S}_6$ and $\text{CuCrP}_2\text{Se}_6$ structure including only Cu and Cr atoms. The white and red mixed ball indicates the disordered distribution of Cu atom at two different positions. In contrast with $\text{CuCrP}_2\text{Se}_6$ compound, $\text{CuCrP}_2\text{S}_6$ has a buckled structure (left). Also $\text{CrS}_6$ octahedron of $\text{CuCrP}_2\text{S}_6$ is much distorted than that of $\text{CuCrP}_2\text{Se}_6$ (right) [93]. . . . .	64
4.5	The temperature dependent magnetization $M$ along $a$ -, $b$ -, and $c$ -directions after zero field cooling process (ZFC). The Néel temperature $T_N$ is 32 K and Curie-Weiss temperature $\theta_{CW}$ is 28 K. . . . .	65
4.6	(a) Spin structure of $\text{CuCrP}_2\text{S}_6$ overlapped in the crystal structure displayed in Fig. 4.3. Green arrows indicates the spin direction. (b) The projection onto $ab$ -plane. . . . .	66
4.7	(a) Magnetization $M$ along $a$ -, $b$ -, and $c$ - directions as a function of magnetic field with $-9 \text{ T} \leq \mu_0 H \leq 9 \text{ T}$ (left) and $-0.9 \text{ T} \leq \mu_0 H \leq 0.9 \text{ T}$ (right) ranges. FIF and SF indicate the magnetic field induced ferromagnetic transition and spin-flop transition, respectively. . .	67
4.8	(a) Magnetization $M$ along $a$ -, $b$ -, and $c$ - directions as a function of magnetic field with $-9 \text{ T} \leq \mu_0 H \leq 9 \text{ T}$ (left) and $-0.9 \text{ T} \leq \mu_0 H \leq 0.9 \text{ T}$ (right) ranges. FIF and SF indicate the magnetic field induced ferromagnetic transition and spin-flop transition, respectively. . .	68
4.9	ME current measured under $E$ -bias at 5 K for $P//c^*$ and $H//ab$ configuration. . . . .	69
4.10	(a) Electric polarization as a function of magnetic field at various temperatures. (b) the selected $\Delta P_{c^*}$ at 5 T and $H_{FIF}$ at each temperatures. . . . .	70

4.11	Magnetic and electric phase diagram of $\text{CuCrP}_2\text{S}_6$ for $H//ab$ . The boundary points are obtained from the dielectric constant $\epsilon$ , electric polarization $\Delta P_{c*}$ , and magnetization $M$ . . . . .	71
4.12	(a) Temperature dependent magnetization curve under $H = 5$ kOe along $ab$ -plane (b)magnetic field dependent magnetization curve under along $ab$ -plane at 5 K. . . . .	72
4.13	Electric polarization of $\text{CuCrP}_2\text{S}_6$ (red line) and $\text{CuCrP}_2\text{Se}_6$ (black line) along $c$ -direction at 5 K for $H // ab$ . . . . .	73
4.14	(a) Magnetic field dependence of electric polarization at each azimuthal angle $\theta^\circ \leq \theta \leq 90^\circ$ (first row), $90^\circ \leq \theta \leq 180^\circ$ (second row), $180^\circ \leq \theta \leq 270^\circ$ (third row), and $270^\circ \leq \theta \leq 360^\circ$ (fourth row). (b) The experimental electric polarization $\Delta P_{c*}$ at 10 K (upper) and calculated electric polarization from $p$ - $d$ hybridization mechanism (lower) as a function of azimuthal angle $\theta$ . . . . .	75
4.15	Electric polarization by the experiment (black line) and the calculation (red line) in $\text{CuCrP}_2\text{S}_6$ . . . . .	77
7.1	Magnetic-field dependent electric polarization of (left) $\text{Ba}_{2-x}\text{Sr}_x\text{Co}_2(\text{Fe}_{0.96}\text{Al}_{0.04})_{12}\text{O}_{22}$ and (right) $\text{Ba}_{2-x}\text{Sr}_x\text{Co}_2(\text{Fe}_{0.92}\text{Al}_{0.08})_{12}\text{O}_{22}$ single crystals. $\Delta P_{max}$ indicates the difference between extreme values, $P_{max}$ - $P_{min}$ and $H_c$ indicates the critical magnetic field where $dP/dH$ is maximum. . .	90
7.2	(a) In-plane and (b) out-of-plane magnetostriction under magnetic field parallel to in-plane direction in $\text{Ba}_{0.2}\text{Sr}_{1.8}\text{Co}_2(\text{Fe}_{0.96}\text{Al}_{0.04})_{12}\text{O}_{22}$ . .	92
7.3	Summary of magnetostriction, magnetization, and electric polarization by the in-plane magnetic field in $\text{Ba}_{0.2}\text{Sr}_{1.8}\text{Co}_2(\text{Fe}_{0.96}\text{Al}_{0.04})_{12}\text{O}_{22}$ . .	93

7.4	(Top) ME current and (Bottom) electric polarization along $c$ -direction by the application of the magnetization along $c$ -direction at 100 K in $\text{Ba}_{0.2}\text{Sr}_{1.8}\text{Co}_2(\text{Fe}_{0.94}\text{Al}_{0.06})_{12}\text{O}_{22}$ . . . . .	94
7.5	(a) Electric polarization along $c$ -direction and (b) phase diagram constructed from the dielectric constant and ME current measurement in $\text{Ba}_{0.2}\text{Sr}_{1.8}\text{Co}_2(\text{Fe}_{0.94}\text{Al}_{0.06})_{12}\text{O}_{22}$ . . . . .	95
7.6	Electric polarization along $c$ -direction by the application of the magnetization along $c$ -direction at 150 K in $\text{Ba}_{0.2}\text{Sr}_{1.8}\text{Co}_2(\text{Fe}_{1-y}\text{Al}_y)_{12}\text{O}_{22}$ . . . . .	95
7.7	(a) Magnetic-field dependent electric polarization of $\text{Ba}_{2-x}\text{Sr}_x\text{CoZn}(\text{Fe}_{1-y}\text{Al}_y)_{12}\text{O}_{22}$ single crystals at 10 K and 150 K. . . . .	97
7.8	The summary of magnetic field-induced polarization at 10 K and 150 K in $\text{Ba}_{0.2}\text{Sr}_{1.8}\text{CoZn}(\text{Fe}_{1-y}\text{Al}_y)_{12}\text{O}_{22}$ . . . . .	98
7.9	An X-ray diffraction pattern of $\text{Ba}_{3-x}\text{Sr}_x\text{Co}_2\text{Fe}_{24}\text{O}_{41}$ poly crystals and its Rietveld refinement result. . . . .	99
7.10	The evolution of $a$ - and $c$ -axis lattice constants with Sr $x$ substitution ratio as determined from the X-ray diffraction data and the Rietveld refinement result of $\text{Ba}_{3-x}\text{Sr}_x\text{Co}_2\text{Fe}_{24}\text{O}_{41}$ poly crystals. . . . .	100
7.11	(a) Voltage driven by the electric current with two-probe method at 300 K in $\text{Ba}_{3-x}\text{Sr}_x\text{Co}_2\text{Fe}_{24}\text{O}_{41}$ . (b) Summary of the resistivity at 300 K in $\text{Ba}_{3-x}\text{Sr}_x\text{Co}_2\text{Fe}_{24}\text{O}_{41}$ poly crystals. . . . .	101
7.12	Summary of the maximum $dP/dH$ and $P$ as a function of Sr ratio $x$ at 10 K, demonstrating that the specimen with $x = 2.4$ has the largest magnetic field induced polarization in $\text{Ba}_{3-x}\text{Sr}_x\text{Co}_2\text{Fe}_{24}\text{O}_{41}$ poly crystals. . . . .	102
7.13	Crystal structure of $\text{Sr}_3\text{Sn}_2\text{O}_7$ projected onto (a) $ab$ -plane and (b) $bc$ -plane. . . . .	103

7.14	(a) The evolution of $c$ -axis lattice constants with Ba substitution $x$ and Ca substitution $y$ ratio calculated from the the Rietveld refinement of $(\text{Ba}, \text{Sr}, \text{Ca})_3\text{Sn}_2\text{O}_7$ poly crystals. (b) Orthorhombicity $(b - a)/(b + a)$ as a function of $x$ and $y$ . . . . .	104
7.15	Raman shift of (top) $(\text{Sr}_{1-y}\text{Ca}_y)_3\text{Sn}_2\text{O}_7$ and (bottom) $(\text{Sr}_{1-x}\text{Ba}_x)_3\text{Sn}_2\text{O}_7$ at 300 K . . . . .	105
7.16	The schematic illustration of R-block contraction by selectively substitution of (a) Ba and (b) Ca in $(\text{Ba}, \text{Sr}, \text{Ca})_3\text{Sn}_2\text{O}_7$ at 300 K .	106
7.17	The XRD data fitted by the Rietveld refinement by assuming that cations are preferring specific site in (a) $(\text{Sr}_{1-y}\text{Ca}_y)_3\text{Sn}_2\text{O}_7$ and (b) $(\text{Sr}_{1-x}\text{Ba}_x)_3\text{Sn}_2\text{O}_7$ . . . . .	107
7.18	Polarization induced by the external electric field measured with the various frequency in $(\text{Sr}_{0.94}\text{Ca}_{0.06})_3\text{Sn}_2\text{O}_7$ at 300 K. Capacitance of the reference is 80 nF and the Sawyer-Tower method with single-loop is used. . . . .	107
7.19	Temperature-dependent ( $10 \text{ K} < T < 600 \text{ K}$ ) dielectric constant of $(\text{Sr}_{1-x}\text{Ca}_x)_3\text{Sn}_2\text{O}_7$ . The excitation frequency is 1 kHz. . . . .	108
7.20	(a) Temperature sequence and pictorial illustration of how $\text{CrSiTe}_3$ single crystal is prepared. [96] (b) Real image of $\text{CrSiTe}_3$ single crystals . . . . .	110
7.21	Variation of resistance of the $\text{CrSiTe}_3$ single crystal as a function of time in the n-Butyllithium. . . . .	111
7.22	Hole carrier density, mobility, and resistivity as a function of temperature from 100 K to 300 K in $\text{Li}_x\text{CrSiTe}_3$ . . . . .	112
7.23	Temperature-dependent (top) magnetization and (bottom) resistivity in the $\text{CrSiTe}_3$ and $\text{Li}_x\text{CrSiTe}_3$ . . . . .	112

7.24	(a) The set-up for liquefying the ammonia and the intercalation of Li <sup>+</sup> ion. (b) The dissolving Li metal into the liquid ammonia. . .	113
7.25	Resistivity of the alkali metal-intercalated CrSiTe <sub>3</sub> single crystal below room temperature. . . . .	113
7.26	(a) Temperature-dependent resistivity of the Li <sub>x</sub> CrSiTe <sub>3</sub> single crystal under hydrostatic pressure ( $0 \text{ GPa} \leq P \leq 2.57 \text{ GPa}$ ) at the zero field. (b) Temperature-dependent resistivity in 2.57 GPa at 0 T (blue line) and 9 T (red line). . . . .	114
7.27	Magnetic field-dependent resistivity of the Li <sub>x</sub> CrSiTe <sub>3</sub> single crystal under hydrostatic pressure at (top) 10 K and (bottom) 30 K. .	115
7.28	Temperature dependence of resistivity in the Cr(Si <sub>1-x</sub> As <sub>x</sub> )Te <sub>3</sub> single crystals. . . . .	115
7.29	a) Z scan and (b) $\omega$ scan to align the sample position in the cryostat.	116
7.30	XRD result analyzed by profiling fitting of Pd <sub>0.07</sub> -TaSe <sub>2</sub> at 13 K. R <sub>wp</sub> is 11.0. . . . .	117
7.31	Summary of the thermal coefficient of Pd <sub>0.07</sub> -TaSe <sub>2</sub> along <i>c</i> -direction as a function of temperature. The red line follows the Debye fitting with $\theta_D = 200 \text{ K}$ . . . . .	118
7.32	XRD results of CaFe <sub>3</sub> O(PO <sub>4</sub> ) <sub>3</sub> at $13 < T < 300 \text{ K}$ . . . . .	119

# List of Tables

2.1	The molar ratio of chemicals to grow $\text{Ba}_{2-x}\text{Sr}_x\text{Co}_2(\text{Fe}_{1-y}\text{Al}_y)_{12}\text{O}_{22}$	12
3.1	Nominal chemical formula and EPMA results. . . . .	28
4.1	Exchange constant $J$ of $\text{CuCrP}_2\text{S}_6$ estimated from the DFT calculation. $J_1$ - $J_5$ indicates the intralayer exchange constant and $J_6$ - $J_7$ is interlayer exchange constant as depicted to Fig. 4.6. . . . .	65
4.2	The distinct atomic positions of Cr atom in one unit cell [90]. . .	76
4.3	Transformational properties of $Pc$ space group. . . . .	76

# ABSTRACT

Studies on the magnetoelectric effects of the  
Co<sub>2</sub>Y-type hexaferrites  
Ba<sub>2-x</sub>Sr<sub>x</sub>Co<sub>2</sub>(Fe<sub>1-y</sub>Al<sub>y</sub>)<sub>12</sub>O<sub>22</sub> and 2D van der  
Waals materials CuCrP<sub>2</sub>X<sub>6</sub> (X=S and Se)

**Chang Bae Park**

Department of Physics and Astronomy  
Graduate School, Seoul National University, Seoul, Korea

For more than a decade, multiferroic or magnetoelectric (ME) materials, in which magnetic and ferroelectric orders coexist and are strongly coupled each other, have been studied extensively. Both their scientific novelty related to the mechanism of ME coupling and application potentials for realizing multifunctional electronic devices have been major driving forces for resulting in the extensive worldwide research activity. Although various new mechanisms and emergent materials have been found during the research activity, it is still rare to find a strong ME coupling at room temperature and in low dimensional system. In particular, the discovery of multiferroic materials with a strong ME coupling at room temperature and in the low dimensional system can open up a new route for nano-scale electronic devices. As candidates of materials with strong ME coupling at room temperature and in low dimension, we report two multiferroics, Co<sub>2</sub>Y-type hexaferrites Ba<sub>2-x</sub>Sr<sub>x</sub>Co<sub>2</sub>(Fe<sub>1-y</sub>Al<sub>y</sub>)<sub>12</sub>O<sub>22</sub> and van der Waals materials CuCrP<sub>2</sub>X<sub>6</sub> (X=S and Se), in this thesis.



In order to control the magnetoelectric coupling strength in the  $\text{Co}_2\text{Y}$ -type hexaferrites, we have investigated comprehensively magnetic, ferroelectric, and magnetoelectric properties of  $\text{Ba}_{2-x}\text{Sr}_x\text{Co}_2(\text{Fe}_{1-y}\text{Al}_y)_{12}\text{O}_{22}$  single crystals in broad doping ranges of Sr and Al ( $1.0 \leq x \leq 1.9$  and  $0.00 \leq y \leq 0.08$ ). We find that most of the investigated compounds exhibit intriguing coexistence of the two competing phases, transverse conical (TC) and alternating longitudinal conical (ALC) spin structures, of which volume fractions are sensitive to the history of both applied temperature and magnetic field conditions. The TC phase tends to become dominant at low temperatures and under in-plane magnetic fields whereas the ALC phase becomes more stabilized at high temperatures and under out-of-field conditions. In particular, the crystal with  $x = 1.8$  and  $y = 0.04$  with a maximized volume fraction of TC phase at room temperature exhibits the highest electric polarization  $\sim 60 \mu\text{C}/\text{m}^2$  at 300 K and  $\sim 430 \mu\text{C}/\text{m}^2$  at 10 K under small in-plane magnetic fields of  $\sim 10$  mT, resulting in the most sensitive ME coupling. Our findings show that the thermal stability of the TC phase closely associated with the control of easy-plane anisotropy and exchange interaction is one of key factors to optimize the ME coupling at room temperature in the  $\text{Co}_2\text{Y}$ -type hexaferrites.

In addition, we report our discovery of magnetic field-induced electric polarization in a two-dimensional (2D) van der Waals material  $\text{CuCrP}_2\text{S}_6$  forming a monoclinic lattice, in which Cu, Cr, and P-P pairs are forming a honeycomb network. We have observed that electric polarization under magnetic fields occurs below 32 K and is modulated by magnetic field while it is suppressed with the spin-flop transition located around 6.1 T. Based on magnetization and electric polarization measurements, electric and magnetic phase diagram has been constructed. We also claim that the magnetic field-induced electric polarization is closely associated with the  $p$ - $d$  hybridization mechanism originated from

---

the off-centered  $\text{Cr}^{3+}$  cations within the octahedral sites. Furthermore, with the symmetry analysis between the antiferromagnetic layers, we could explain the shape of the electric polarization curve qualitatively. The  $p-d$  hybridization mechanism is further corroborated by the observation of vanishing polarization in the  $\text{CuCrP}_2\text{Se}_6$  compound in which  $\text{Cr}^{3+}$  is positioned at the octahedral center, further supporting that the off-centered cation plays an important role in the magnetoelectric coupling. Our results thus point to one general route to induce magnetoelectric coupling in 2D layered materials, *i.e.*, via the off-centered cation.

---

**Key words :** multiferroics, magnetoelectrics, ferroelectrics, hexferrites, van der Waals material

**Student number :** 2013-20369

# Chapter 1

## Introduction

Multiferroics and magnetoelectric (ME) materials have been intensively investigated due to their potential to realize the next generation devices [1]. As depicted in Fig 1.1, multiferroics indicate the materials in which at least two ferroic orders such as ferromagnetic, ferroelectric, and ferroelastic orders coexist. We deal with the combination of ferroelectricity and magnetism in this thesis.

The coexistence of magnetism and ferroelectricity in one material was con-

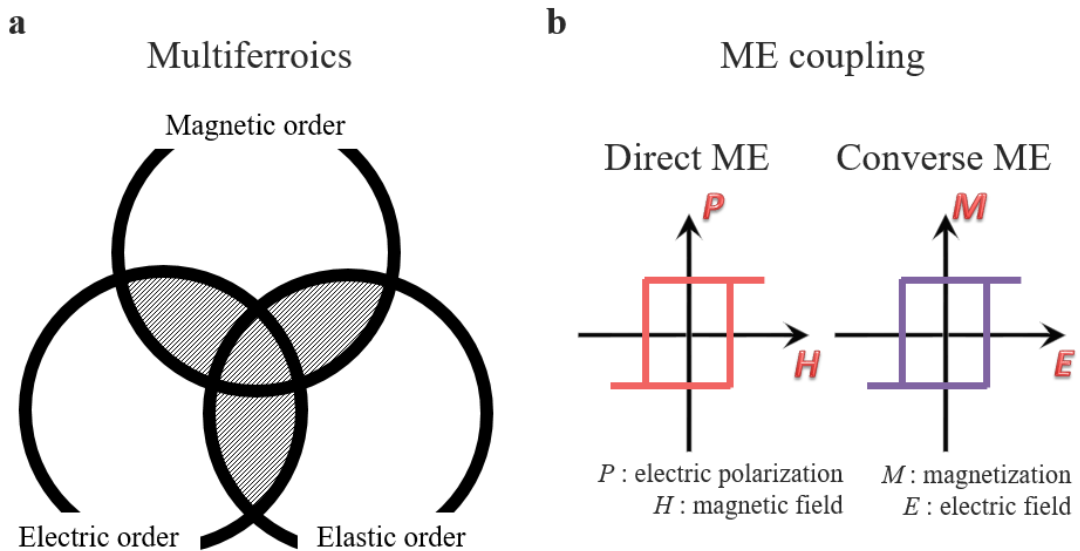


Figure 1.1: Schematic diagram of (a) multiferroics and (b) magnetoelectric coupling.

sidered as a challenge because the origins of two order parameters are mutually exclusive [2]. For example, ferroelectric properties in most of the perovskite materials are originated from the structural distortion stabilized from the strong covalent bonding between empty  $d$ -orbitals of the transition metal and filled  $p$ -orbitals of oxygen [3]. On the other hand, magnetism results from the partially occupied  $d$ -orbital, which means that ferroelectricity and magnetism are difficult to be compatible with each other.

Apart from the multiferroics, ME coupling means the control of electric polarization (magnetization) by magnetic (electric) field. Therefore, the coexistence of ferroelectricity and magnetism does not ensure the strong ME coupling if the mechanisms of coexisting phases are different [4]. To overcome the issues, spin-induced ferroelectricity has been suggested as a solution and a modulation of electric polarization by magnetic field has been observed in various types of materials with complex spin structures [5,6]. In these materials, not only spatial-inversion but also time-reversal symmetry is broken by the complex spin structure, resulting in the emergence of an electric polarization [7,8].

I will briefly introduce multiferroics and ME materials in this chapter. In particular, the origins of spin induced ferroelectricity and relevant materials will be explained.

## 1.1 Types of multiferroics

Multiferroics are categorized into two types depending on the relation between ferroelectricity and magnetism [9, 10].

### 1.1.1 Type-I multiferroics

Type-I multiferroics include materials with the distinct sources of ferroelectricity and magnetism. As a result, the ferroelectric Curie temperature  $T_c$  is different from the antiferromagnetic Néel temperature  $T_N$  and the ME coupling is weak. In general,  $T_c$  is quite high above room temperature and the magnitude of electric polarization is sizable. BiFeO<sub>3</sub> and YMnO<sub>3</sub> are well-known examples of type-I multiferroics.

BiFeO<sub>3</sub> with a perovskite structure is one of the promising multiferroics. Ferroelectricity of BiFeO<sub>3</sub> is originated from 6s lone pair electrons of Bi<sup>3+</sup> cations, while antiferromagnetic ordering is induced by partially-filled 3d electrons in Fe<sup>3+</sup> cations [11]. Thus, BiFeO<sub>3</sub> belongs to the class of type I multiferroics with  $T_c$  of 1100 K and  $T_N$  of 643 K. The large magnitude of electric polarization has been observed in both bulk and film forms of BiFeO<sub>3</sub> reaches to  $\sim 90 \mu\text{C}/\text{cm}^2$  [13, 25]. However, the ME coupling is relatively weak because the ferroelectricity and antiferromagnetic ordering are coming from the different origins, thus the ME susceptibility  $dP/dH$  which quantifies the magnitude of ME coupling is small  $\sim 55 \text{ ps/m}$  [14]

Another example is a hexagonal manganite YMnO<sub>3</sub>. The tilting of MnO<sub>5</sub> polyhedra cause the noncentrosymmetric position of Y<sup>3+</sup> and induces a ferroelec-

tric transition at 914 K [15]. Furthermore, the coupled ferroelectric and magnetic domains in  $\text{YMnO}_3$  was observed by the second harmonic generation [16]. However, the geometrical ferroelectricity is not directly associated with the magnetism of  $\text{Mn}^{3+}$  cations which orders antiferromagnetically at 76 K and ME coupling is weak as well.

### 1.1.2 Type-II multiferroics

In contrast, the class of type-II multiferroics contains materials with an electric polarization generated by the complex spin structures. This type of ferroelectricity, so-called improper ferroelectricity, gives rise to a small electric polarization because the electric polarization is not a main order parameter of the ferroelectric transition but a by-product of magnetic ordering [2]. Therefore, the ferroelectricity always accompanies the magnetic ordering, leading to the same  $T_c$  and  $T_N$ . As a result, they are strongly coupled to each other and the ME susceptibility is expected to be large.

Type-II multiferroic material was first discovered in orthorhombic  $\text{TbMnO}_3$  [7].  $\text{TbMnO}_3$  undergoes two antiferromagnetic transitions below  $T_{N1} = 41$  K and  $T_{N2} = 28$  K. Below  $T_{N2}$ , finite electric polarization is induced with the incommensurate spiral spin ordering and they are strongly coupled [17, 18].  $\text{TbMn}_2\text{O}_5$  is another example of type-II multiferroics [8]. The origin of electric polarization is known as the exchange striction mechanism between the  $\text{Mn}^{4+}$ - $\text{Mn}^{3+}$  spin chain at 37 K [89]. Lastly, Y- and Z-type hexaferrites materials are type-II multiferroic with giant ME coupling [20, 21, 24].

The mechanism of spin-induced ferroelectricity is summarized into the three major models depending on spin structures and microscopic origins. The three models are discussed in the next section.

## 1.2 The origins of spin-induced ferroelectricity

Most of the spin-induced ferroelectricity drive the electric polarization  $P$  by following one of the three major models; exchange striction model, spin current model, spin-dependent  $p$ - $d$  hybridization model. In this section, we explain the mechanisms and the relevant materials.

### 1.2.1 Exchange striction model

In the exchange striction mechanism,  $P$  generated from the symmetric exchange interaction between the neighboring magnetic ions, denoted by  $i^{th}$  and  $j^{th}$  ions, with spin operator  $S_i$  and  $S_j$  is expressed by

$$P_{ij}^{ES} = \Pi_{ij} \langle S_i \cdot S_j \rangle, \quad (1.1)$$

where  $\Pi_{ij}$  is the unit vector that points from the ligand site to the center of the line connecting to two neighboring magnetic ions [25]. The macroscopic  $P$  can be observed if the summation of  $P_{ij}^{ES}$  between neighboring ions over every bonding has a finite value.

The exchange striction mechanism arises in spin  $\uparrow\uparrow\downarrow\downarrow$  configuration which can be stabilized from the competitive interaction between nearest and next-nearest neighboring ions. Fig. 1.2 shows the spin  $\uparrow\uparrow\downarrow\downarrow$  configuration in magnetic chain with two alternating charges. The ions attract (repulse) each other when the direction of the neighboring spins are parallel (antiparallel) to reduce exchange energy, resulting in the spatial-inversion symmetry breaking and the emergence of  $P$ .

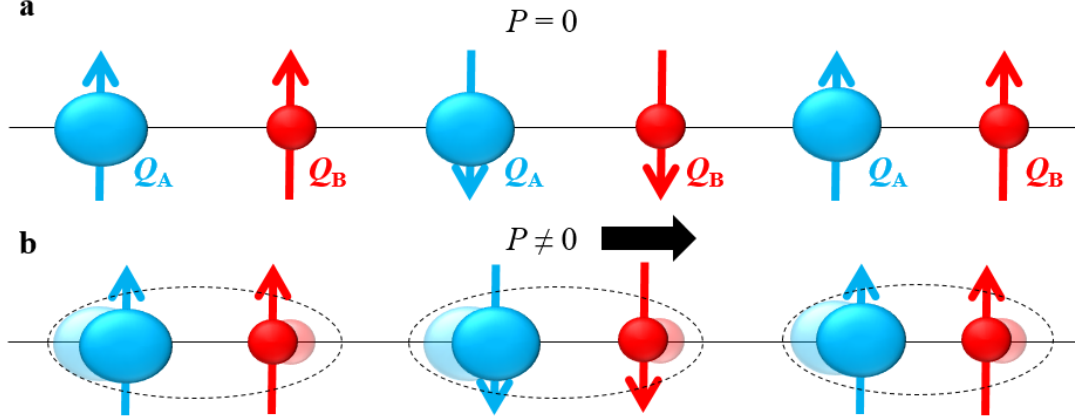


Figure 1.2: (a) The chain with spin  $\uparrow\uparrow\downarrow\downarrow$  configuration. Arrows indicate the spin direction. Blue and red spheres depict two different magnetic atoms A and B with charge  $Q_A$  and  $Q_B$ , respectively. (b) The emergence of electric polarization by exchange striction mechanism.

Rare-earth orthorhombic manganites  $\text{RMnO}_3$  ( $R = \text{Ho} - \text{Lu}$ ) with  $E$ -type AFM order [26,27], the  $\text{Mn}^{3+}$ - $\text{Mn}^{4+}$  mixed manganites  $\text{RMn}_2\text{O}_5$  [28], and  $\text{Ca}_3\text{CoMnO}_6$  with spin  $\uparrow\uparrow\downarrow\downarrow$  ordering [29] are widely known as having the ME coupling originated from the exchange striction.

### 1.2.2 Spin current model

The spin current model or inverse Dzyaloshinskii-Moriya mechanism [30] arising from the antisymmetric spin exchange interaction is formulated by

$$P_{ij}^{SC} \propto e_{ij} \times j_s = e_{ij} \times \langle S_i \times S_j \rangle \quad (1.2)$$

$e_{ij}$  is a unit vector pointing from  $S_i$  to  $S_j$  and  $j_s = \langle S_i \times S_j \rangle$  is termed the spin current. In this mechanism, the collinear spin order is not expected to generate the  $P$  because spin current  $\langle S_i \times S_j \rangle$  is estimated to be zero. Thus, the spin current model is only applicable to the canted spin magnet such as cycloidal and transverse conical spin structure. Plenty of previous studies verify



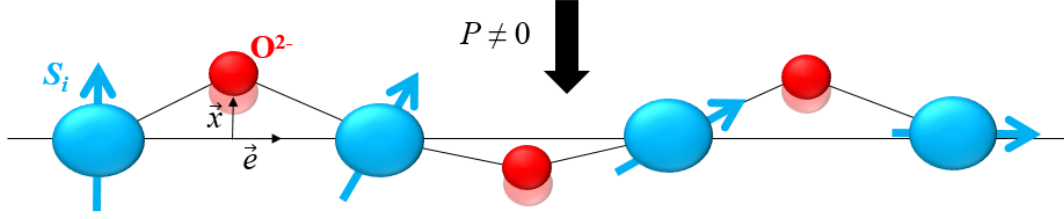


Figure 1.3: (a) The spin chain with the spiral spin ordering. Blue arrows indicate the spin direction. Blue and red spheres indicates magnetic and oxygen ions, respectively.  $\vec{e}$  is an unit vector parallel to the direction of spin propagation and  $\vec{x}$  is a displacement vector of oxygen ion from the the center of the line connecting to two neighboring magnetic ions.

that the spin frustration competing against exchange interaction is a key feature for cycloidal spin ordering [31, 32].

Fig. 1.3 displays  $P$  driven by the spin current model in spiral spin ordering. The spin current model is derived from the Dzyaloshinskii-Moriya (DM) interaction. The Hamiltonian of DM interaction between the canted spins is formulated by

$$H_{DM} = D_{ij} \cdot (S_i \times S_j) \quad (1.3)$$

$D_{ij}$  is DM vector defined as  $\vec{e} \times \vec{x}$ . Once spiral spin ordering is stabilized in a system, oxygen atoms move to minimize the  $H_{DM}$  as depicted in Fig. 1.3.

However, the canted spin does not guarantee to induce  $P$  via the spin current mechanism. Fig. 1.4 presents several spin structures with the spiral spin order and it is found that the cycloidal and transverse conical spin structure are allowed to have  $P$ .

### 1.2.3 Spin-dependent $p$ - $d$ hybridization model

In the spin-dependent  $p$ - $d$  hybridization mechanism, local  $P$  is generated from

electronic bonding between  $p$ -orbital of a ligand ion and  $d$ -orbital of a transition metal magnetic ion (Fig. 1.5) [5]. The electronic hybridization depends on the spin direction of magnetic ion due to spin–orbit coupling forms

$$P_{ij}^{PD} \propto e_{il}(S_i \cdot e_{il})^2 \quad (1.4)$$

where  $e_{il}$  is parallel to bonding direction connecting the magnetic  $i^{th}$  ion and ligand ion  $l$ . For example, the origin of ME coupling in  $\text{CuFeO}_2$  with incom-

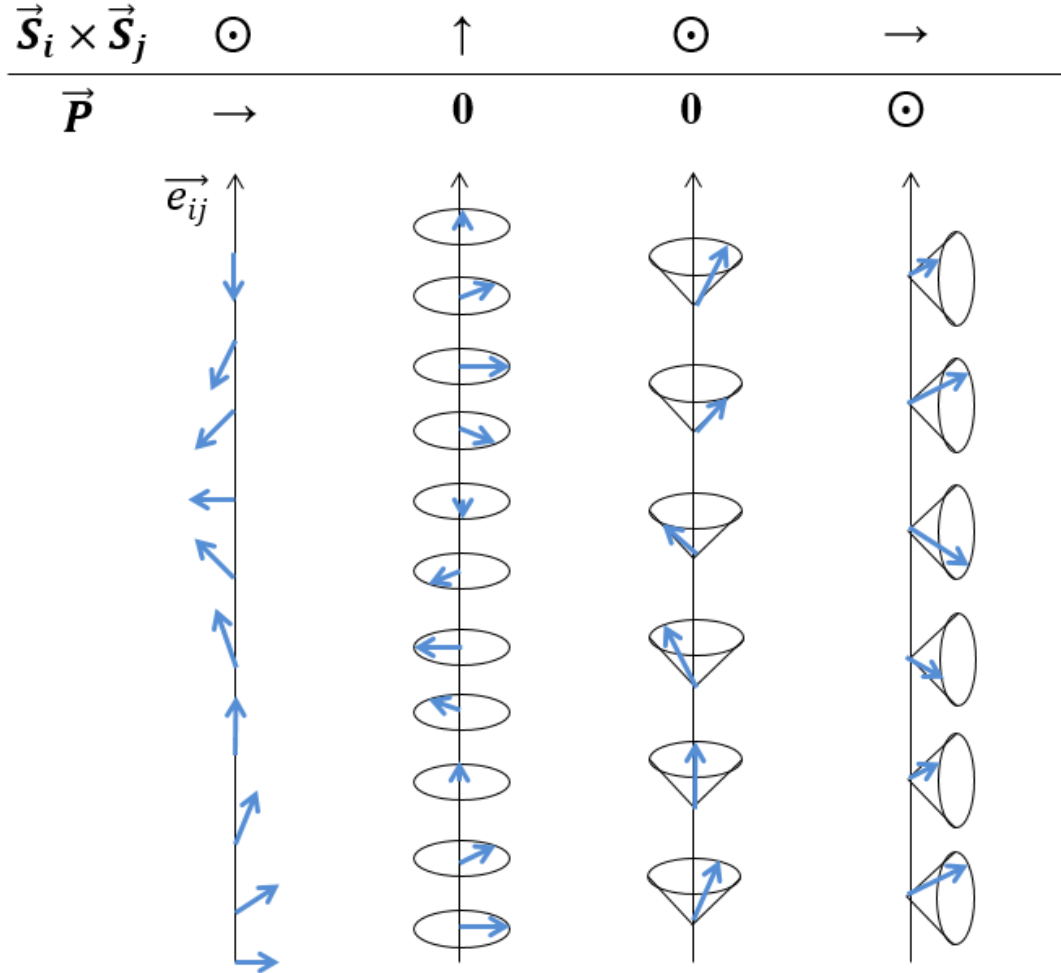


Figure 1.4: The selected non-collinear spin structures and application of the spin current model.

mensurate spiral spin ordering has been turned out the spin-direction dependent hybridization between  $d$ -orbital of  $\text{Fe}^{3+}$  ions and  $p$ -orbital of  $\text{O}^{2-}$  ions [33].  $\text{Ba}_2\text{CoGe}_2\text{O}_7$  also has magnetic field-induce polarization originated from spin-dependent  $p-d$  hybridization [34,35].

### 1.3 Outline of Thesis

The industrial application of multiferroics and ME coupling will open up a new prospect to the multifunctional device. It would be realized if new material showing the giant ME effect at room temperature and two-dimensional (2D) material of a nano-scale are discovered. As the candidates of ME materials with

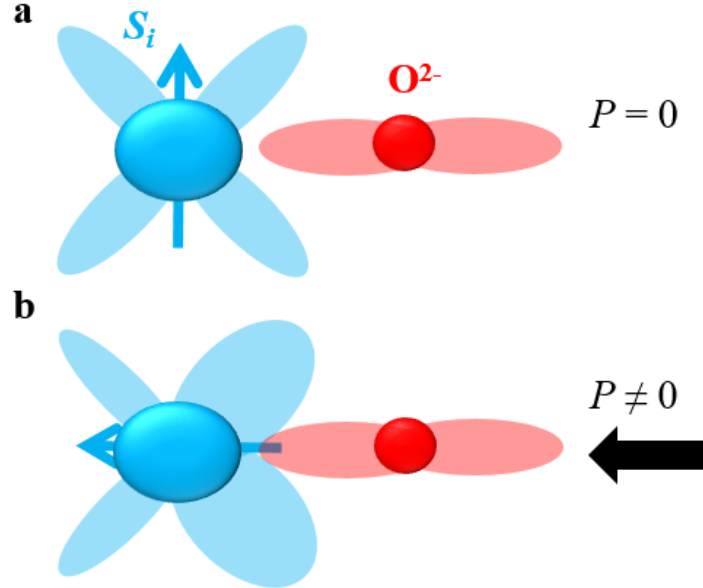


Figure 1.5: Schematic illustration of  $p$ - $d$  hybridization when (a) the spin is perpendicular to the bonding direction and (b) parallel to the bonding direction. Blue arrows indicate the spin direction. The blue and red areas represent the  $d$ - and  $p$ - orbitals of magnetic ions and ligand ions, respectively.  $e_{il}$  is along bonding direction.

the large ME effect at room temperature and in the 2D, we mainly discuss the two kinds of type-II multiferroics,  $\text{Co}_2\text{Y}$ -type hexaferrites and van der Waals materials  $\text{CuCrP}_2\text{X}_6$  ( $\text{X} = \text{S}$  and  $\text{Se}$ ) in this thesis.

First, the family of  $\text{Co}_2\text{Y}$ -type hexaferrites  $(\text{Ba}, \text{Sr})_2\text{Co}_2\text{Fe}_{12}\text{O}_{22}$  has been widely investigated because it exhibits the giant ME coupling [36]. However, the systematic doping study to optimize the ME effect in single crystals has not been done. Sr- and Al- substitutions are known as controlling the magnetic anisotropy and spin frustration and eventually they modulate the magnitude of ME coupling in Y-type hexaferrites [21]. Thus, we report the study on the ME coupling of  $\text{Ba}_{2-x}\text{Sr}_x\text{Co}_2(\text{Fe}_{1-y}\text{Al}_y)_{12}\text{O}_{22}$  with various  $x$  and  $y$  values. Furthermore, the role of Sr and Al doping and the mechanism on how the ME effect can be optimized are discussed.

Next, the newly discovered ME effect in van der Waals material  $\text{CuCrP}_2\text{S}_6$  is presented. ME effect in 2D van der Waals materials is rare even in bulk crystals. Even though the study has been performed in the bulk material, we believe that the observation of ME coupling in  $\text{CuCrP}_2\text{S}_6$  will be a driving force to realize the ME effect in monolayer-limit. At the end of the section, we study the microscopic mechanism of spin-induced ferroelectricity and symmetry analysis to investigate the origin of ME coupling. Particularly, the spin-dependent  $p$ - $d$  hybridization model will be thoroughly inspected.

## Chapter 2

# Experimental Methods

In this chapter, we describe the experimental methods utilized to investigate the ME effect in this thesis. This section is divided into two main categories, the single crystal growth and measurement of ME effect. The single crystal growth part contains the flux method, thermal annealing, chemical vapor transport method, which has been used to grow  $\text{Co}_2\text{Y}$ -type hexaferrites and  $\text{CuCrP}_2\text{X}_6$  respectively. Measurement part includes the magnetization, dielectric constant, and ME current measurements at low temperature ( $T \sim 1.8 \text{ K}$  ).

## 2.1 Single crystal growth

### 2.1.1 Flux method

Co<sub>2</sub>Y-type hexaferrites Ba<sub>2-x</sub>Sr<sub>x</sub>Co<sub>2</sub>(Fe<sub>1-y</sub>Al<sub>y</sub>)<sub>12</sub>O<sub>22</sub> single crystal has been grown by the flux method. Na<sub>2</sub>O-Fe<sub>2</sub>O<sub>3</sub> are used as a flux. The chemicals is weighed as shown in Table 2.1. The chemicals is put into a platinum crucible and capped with platinum lid to prevent from the overflow. The platinum crucible is placed into the well-calibrated box furnace and the mixed chemicals are melted at 1350 °C. A series of temperature steps including several thermal cyclings and slow cooling is entered into the program of temperature controller as displayed in Fig. 2.1. The oscillation around CoFe<sub>2</sub>O<sub>4</sub> nucleation point, 1350 °C, fades away with time to remove the spinel impurity [37], and then temperature is cooled down. The solidified products are detached from the platinum crucible mechanically and shiny crystals are collected from them. When single crystals are not separated from the flux perfectly, the mixture of nitric acid and water (1 : 1) is occasionally used. The mixture is boiled at 80 °C for 10 minutes with single crystals. However, the chemical method can damage single crystals by nitric acid and water, thus the mechanical method is always preferred.

Grown single crystals are checked with X-ray diffractometer (XRD) and electron probe micro-analyzer (EPMA). XRD data is compared with the known struc-

Chemicals	BaCO <sub>3</sub>	SrCO <sub>3</sub>	CoO	Fe <sub>2</sub> O <sub>3</sub>	Al <sub>2</sub> O <sub>3</sub>	Na <sub>2</sub> O
Ratio	19.69(1-x)	19.69x	19.69	53.61(1-y)	53.61y	7.01

Table 2.1: The molar ratio of chemicals to grow Ba<sub>2-x</sub>Sr<sub>x</sub>Co<sub>2</sub>(Fe<sub>1-y</sub>Al<sub>y</sub>)<sub>12</sub>O<sub>22</sub> single crystal

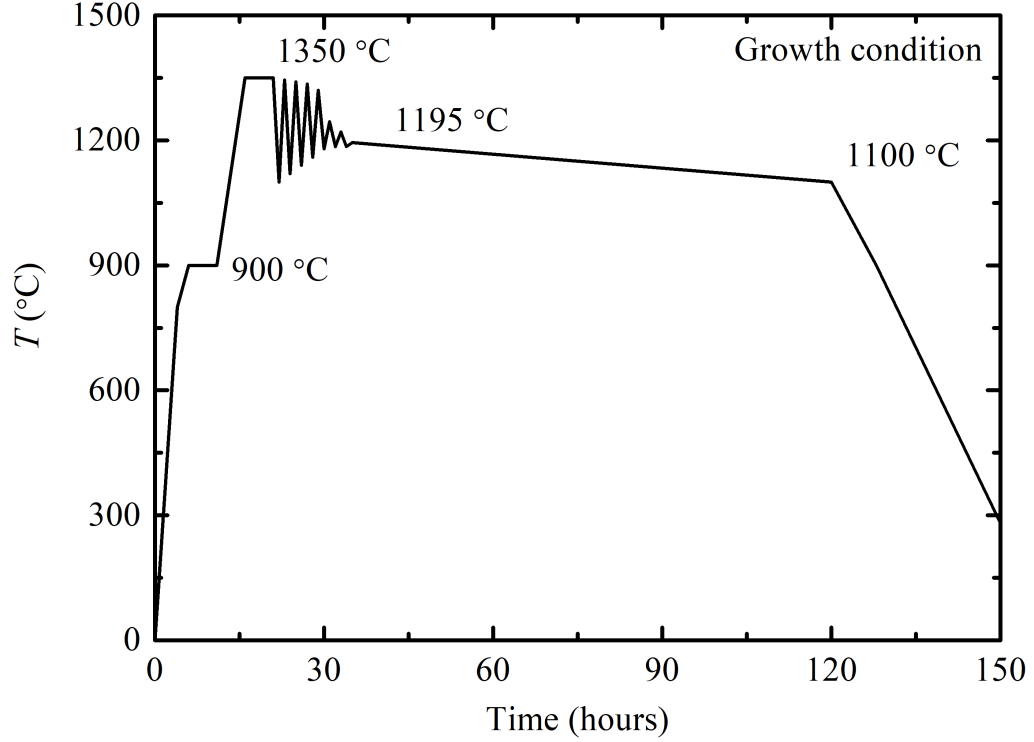


Figure 2.1: The temperature sequence to grow  $\text{Co}_2\text{Y}$ -type single crystals.

ture published in [38] and lattice parameters are estimated by Rietveld refinement method. EPMA is used to confirm whether the actual amount of Sr and Al substitution corresponds to the target value.

### 2.1.2 Thermal annealing

The thermal annealing under oxygen atmosphere removes the possible oxygen vacancy, resulting in the high resistivity by decreasing electron carriers. The high resistivity reduces a leakage current while ME effect measurement is performed and enables to investigate the intrinsic ME properties. In this thesis, Thermal annealing in the high pressure has been carried out. Ni-based superalloy from MTI Corporation (Fig. 2.2) is used as a sample chamber for high pressure annealing. Fig. 2.3 shows the change of resistivity depending on the annealing

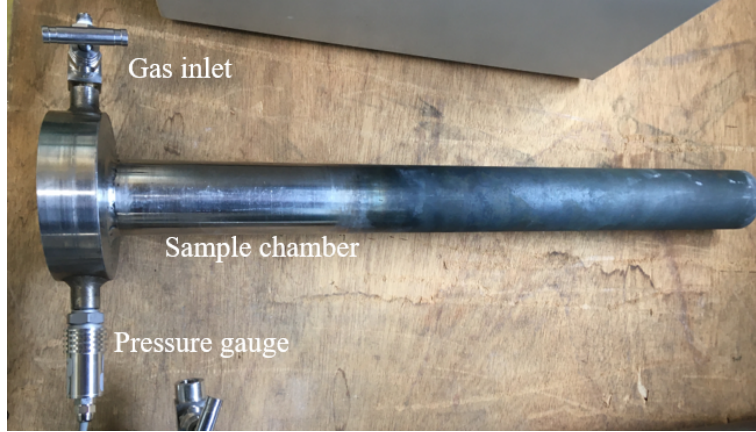


Figure 2.2: The picture of the chamber for annealing in high pressure

condition. It is concluded that two hours are enough to make crystals insulate at 5 MPa oxygen atmosphere. The general tube furnace is also used if high pressure furnace is not available. The annealing in ambient pressure follows the condition from Chai *et al.* [39].

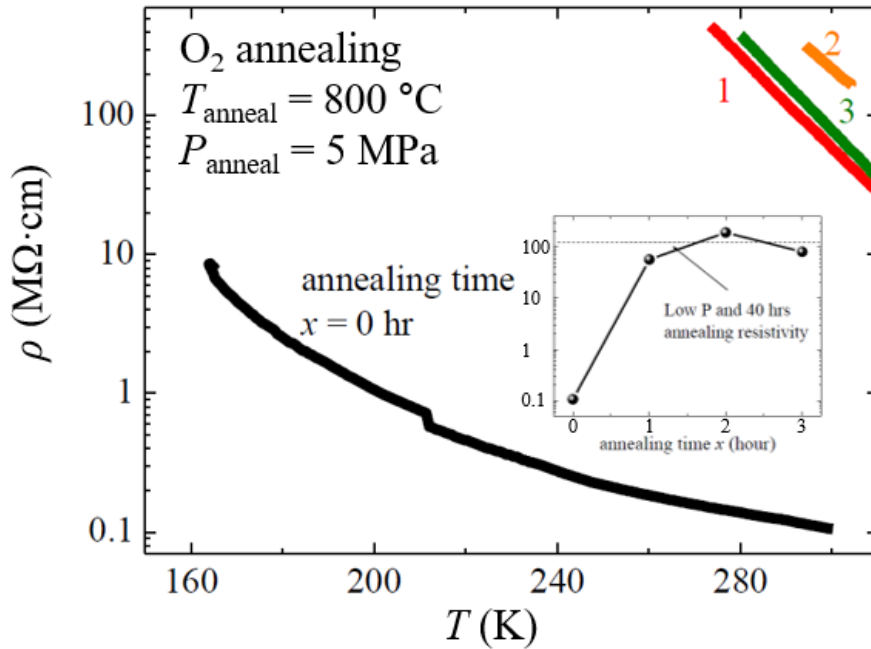


Figure 2.3: The resistivity as a function of temperature after the thermal annealing under oxygen atmosphere.



### 2.1.3 Chemical vapor transport method

$\text{CuCrP}_2\text{X}_6$  ( $\text{X}=\text{S}$  and  $\text{Se}$ ) single crystal has been prepared by Dr. A. Shahee and Dr. D. R. Patil. Chemical vapor transport (CVT) method has been used to grow single crystal [40]. The starting materials are weighed with stoichiometric ratio and contained to an evacuated quartz tube. S and  $\text{SeCl}_4$  are used as transport agent of  $\text{CuCrP}_2\text{S}_6$  and  $\text{CuCrP}_2\text{Se}_6$ , respectively. The sealed quartz tube is put into the tube furnace and the seed powder is positioned at the hot zone. Plate crystals are formed at the cold zone.

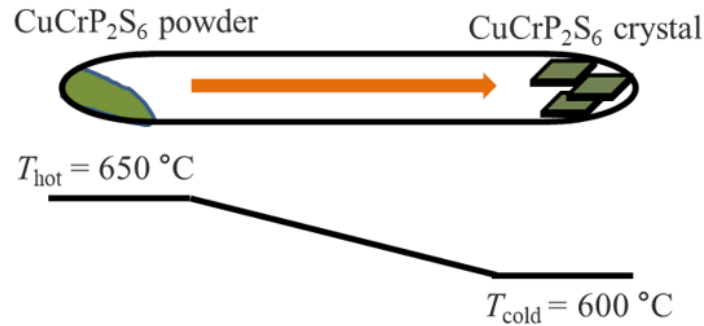


Figure 2.4: The schematic illustration of chemical vapor transport method.

## 2.2 Measurements

### 2.2.1 Magnetization

The vibrating sample magnetometer (VSM) option utilized in Physical Property Measurement System (PPMS<sup>TM</sup>, Quantum Design) and Magnetic Property Measurement System (MPMS<sup>TM</sup>) are used to characterize the magnetic properties. The typical resolution of VSM is around  $10^{-5}$  emu. The superconducting magnet always have a remnant magnetic field by inherent pinning of the magnetic flux and it makes an error in the magnetic field near zero field. The magnetic

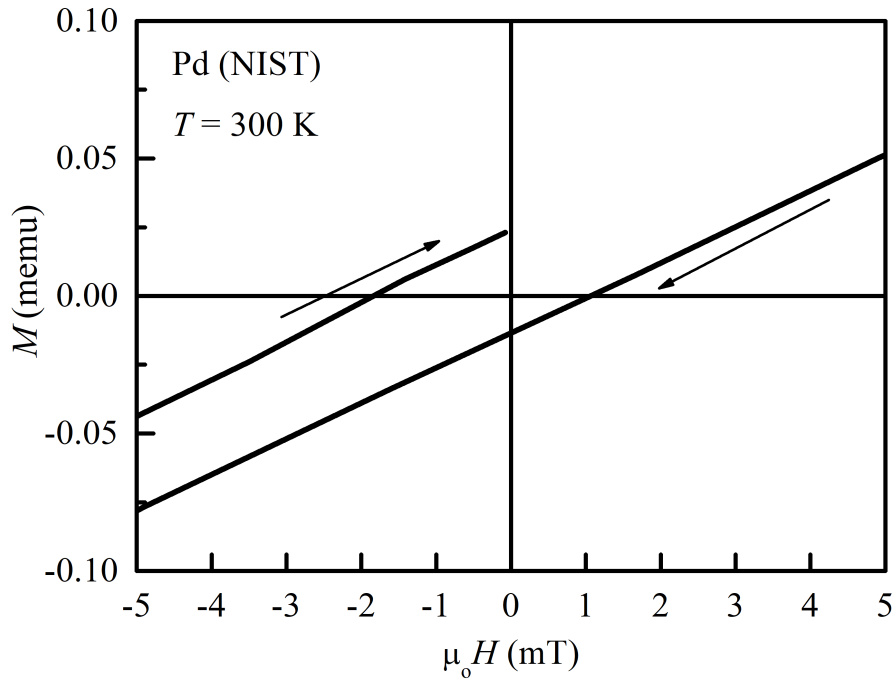


Figure 2.5: Magnetization curve of the standard palladium sample to calibrate the magnetic field near zero field.

field error can be removed by turning off the field with the oscillation mode from the high field. However, it is impossible to use oscillation mode when field cooling (FC) measurement is being done and the precise calibration of magnetic field near zero field is essential. The magnetic field is calibrated by measuring the paramagnetic palladium sample from National Institute of Standards and Technology (NIST). Data is shown in Fig. 2.5. It clear shows that there exist an error of -2 mT (1 mT) while increasing (decreasing) the field near 0 T. The actual magnetic field value is corrected based on the calibration.

Furthermore, sample is cut into needle shape to decrease the demagnetization effect by shape anisotropy. The demagnetization factor  $N$  reduces the magnetic field sample feels. The relation between external magnetic field and actual magnetic field expressed by

$$H_{actual} = H_{external} - NM, \quad (2.1)$$

where  $M$  is magnetization of the sample. Thus, to suppress the demagnetization effect is crucial when measuring the big magnetization. All of samples are attached on the sample holder using GE Varnish or cotton string.

Magnetization also can be measured at high temperature ( $300 \text{ K} \leq T \leq 800 \text{ K}$ ) with lab-made probe.

### 2.2.2 Dielectric constant

To measure the dielectric constant, single crystal is cut and polished into the plate. Two electrodes are attached on the each side of the plate to make a capacitor. Silver epoxy (Epotek H20E) is used as a conducting glue, attaching the electrodes and heated at  $150 \text{ }^\circ\text{C}$  for 5 minutes to solidify the silver epoxy. However, silver reacts with chalcogen on heating and the insulating layers, such

as  $\text{Ag}_2\text{S}$ , are created. The unexpected products prevent from investigating the intrinsic properties, thus silver paste is used for the chalcogenide because heating is not needed to cure the silver paste.

The capacitor sample is loaded on the lab-made probe which is utilized in the PPMS. Actually we measure the capacitance, not dielectric constant. The dielectric constant  $\epsilon$  is converted from the capacitance by the relation as below:

$$C = \epsilon \frac{A}{d} \quad (2.2)$$

where  $C$  is a capacitance,  $A$  is an area of the sample and  $d$  is a thickness of the capacitor. The capacitance is measured with capacitance bridge and LCR meter. In this thesis, we have used capacitance bridge AH2550 at the frequency of 1 kHz.

Dielectric constant is a complex number because we measure the capacitance with AC voltage. The imaginary part of dielectric constant is called dielectric loss and related to the leakage current. Electric current flows across the sample because our sample has a finite resistivity, indicating that it is not a perfect capacitor in reality. The dielectric loss should be considered whenever electric field is applied not to break sample.

### **2.2.3 Direct magnetoelectric effect**

The same sample configuration with the dielectric constant measurement is used for the direct ME effect measurement. Direct ME effect means the control of electric polarization by the magnetic field. The electric polarization of the sample generates the electric field which binds the charges to the boundary between the silver epoxy and the sample surface. Once the electric polarization disappears due to the ferroelectric to paraelectric phase transition by sweeping the magnetic field or temperature, the accumulated charges flow through the circuit. The

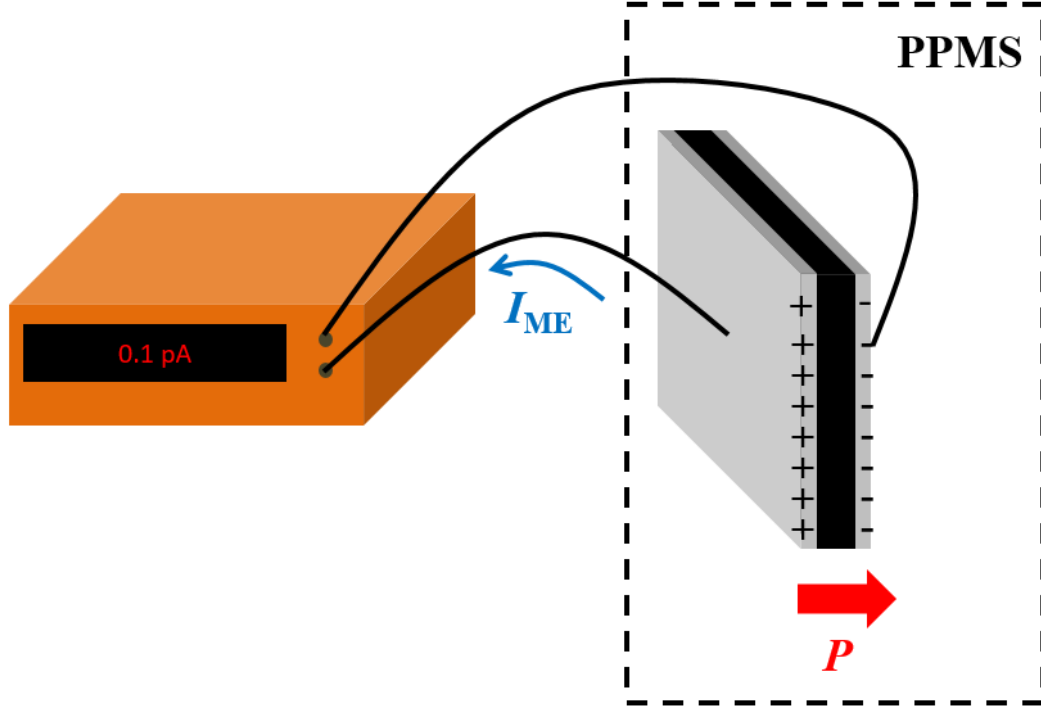


Figure 2.6: The schematic picture of magnetoelectric current measurement.

flowing current is called ME current and electric polarization is proportional to the accumulated charges. The charges are estimated by integrating the current with a time. Therefore, electric polarization is calculated by the equation below :

$$\Delta P = \int I_{ME} dt \quad (2.3)$$

where  $\Delta P$  is a change of the electric polarization by passing the ferroelectric phase to paraelectric phase and  $I_{ME}$  is a ME current. The current is measured with a sensitive electrometer such as Keithley 617 with a resolution of  $10^{-15}$  A, because a typical ME current signal is quite small. Therefore, the wires should be shielded well from the external noise by using coaxial wires and a clean ground.

Before performing the ME current measurement, a process to make ferroelectric domain an unity, so-called an ME poling, is proceeded. All of ferroelectric

materials form ferroelectric domains to minimize the energy by reducing the stray electric field diverging to the outside of sample. If various ferroelectric domains exist, the macroscopic polarization is cancelled out, resulting in an absence (or decreasing) of ME current. To pole the sample, electric field is applied at the paraelectric phase and then the paraelectric phase is turned into ferroelectric phase by changing the magnetic field or temperature. Finally, the electric field is turned off and ME poling procedure is finished.

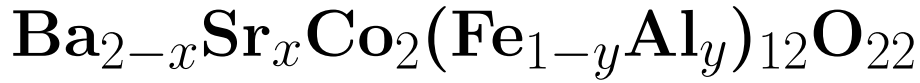
In addition, ME current also can be measured under the biased-electric field especially for poly crystals [41]. The biased electric field removes the internal electric field effect induced by the trap charges in the grain boundary.

#### **2.2.4 Converse magnetoelectric effect**

Converse ME effect indicates the control of magnetization by the electric field. The magnetization is measured with a VSM option in PPMS and simultaneously electric field is applied by an external voltage source. In order to make the application of the electric field possible, modified sample probe has been utilized [42].

# Chapter 3

## Co<sub>2</sub>Y-type hexaferrites



### 3.1 Introduction

For more than a decade, multiferroic or magnetoelectric (ME) materials, in which magnetic and ferroelectric orders coexist and are strongly coupled each other, have been studied extensively. Both their scientific novelty related to the mechanism of strong magnetoelectric coupling [3, 43–45] and application potentials for realizing multifunctional electronic devices [1, 8] have been major driving forces for resulting in the extensive worldwide research activity. Although various new mechanisms and emergent materials have been found during the research activity [2, 3, 21, 43, 44], it is still rare to find ME materials with strong ME coupling at room temperature. Only a limited number of materials such as BiFeO<sub>3</sub>, Cr<sub>2</sub>O<sub>3</sub>, and the hexaferrites with Y- or Z-type structure have exhibited sizable ME coupling at room temperature. However, the ME coupling strength of those compounds is yet too small for practical applications; for example, the ME susceptibility, defined here as derivative of electric polarization ( $P$ ) with respect to magnetic field ( $H$ ),  $dP/dH$ , shows a maximum of 3 ps/m for Cr<sub>2</sub>O<sub>3</sub> [46] and

$\sim 55$  ps/m for  $\text{BiFeO}_3$  [14] at 300 K. Therefore, it is currently of high interests to explore new multiferroics that can exhibit higher ME coupling at room temperature.

In order to achieve strong ME coupling near room temperature, several ferrites with the hexagonal crystal structure have been studied. In particular, those Z- and Y-type hexaferrites having spinel and tetragonal structural units stacked along the  $c$ -axis have indeed exhibited giant ME coupling ( $dP/dH > 500$  ps/m). The geometric frustration existing at the interface of the two structural units has indeed resulted in a non-collinear spin structure such as a conical spin order, which is a key to generation of spin-driven ferroelectricity via the inverse Dzyaloshinskii-Moriya (DM) mechanism [20, 21, 47, 48]. More importantly, those hexaferrites exhibit several intrinsic material properties that can allow strong ME coupling near room temperature. First of all, the conical spin ordering temperatures in some of hexaferrites are located above room temperature [49, 50, 50, 52]. For example, a transverse conical ordering temperature ( $T_{con}$ ) of the  $\text{Co}_2\text{Z}$ -type hexaferrite  $\text{Ba}_{0.52}\text{Sr}_{2.48}\text{Co}_2\text{Fe}_{24}\text{O}_{41}$  is located at 413 K [47], allowing room temperature operation of the ME effects. Secondly, a critical magnetic field for switching on  $P$  is mostly quite low [39, 53–55], presumably due to soft nature of the conical spin structure. As a result, the direction of electric polarization can be easily reversed at a very small  $H$  bias of  $\sim 1$  mT as demonstrated in one of the  $\text{Zn}_2\text{Y}$ -type hexaferrites (BSZFAO) [21, 56, 57]. Thirdly, magnetization reversal by electric field without  $H$  bias has been demonstrated in the Y-type hexaferrites ( $\pm 2 \mu_B/\text{f.u.}$  under  $\pm 2$  MV/m); the two materials properties of the magnetic softness and giant direct ME coupling were keys to leading such giant converse ME effects [48].

For those several advantages, the Y-type hexaferrites are currently drawing



lots of research attention [36]; they offer great potential for realizing the electric field  $E$  control of magnetization  $M$  reversal at room temperature due to their large direct ME coupling that results in a sharp increase (decrease) of  $P$  at a small positive (negative)  $H$  bias [21, 58]. On the other hand,  $T_{con}$  in most of the Y-type hexaferrites are still located below room temperature, hindering realization of the ME effects near room temperature. It has been uncovered that the  $T_{con}$  can be increased when zinc ions are replaced by cobalt ions in the ceramic samples [56]. However, it has been difficult to quantify intrinsic ME effects in the ceramic samples because of the trapped charges in the grain boundary. Fig. S1 illustrates that the ME properties between the ceramic and single crystal samples do not coincide in the same nominal composition [52, 55] suggesting that systematic study in a single crystal form is required to understand the intrinsic ME coupling in the Co<sub>2</sub>Y-type and related hexaferrites. Along this line, Kocsis *et al.*,

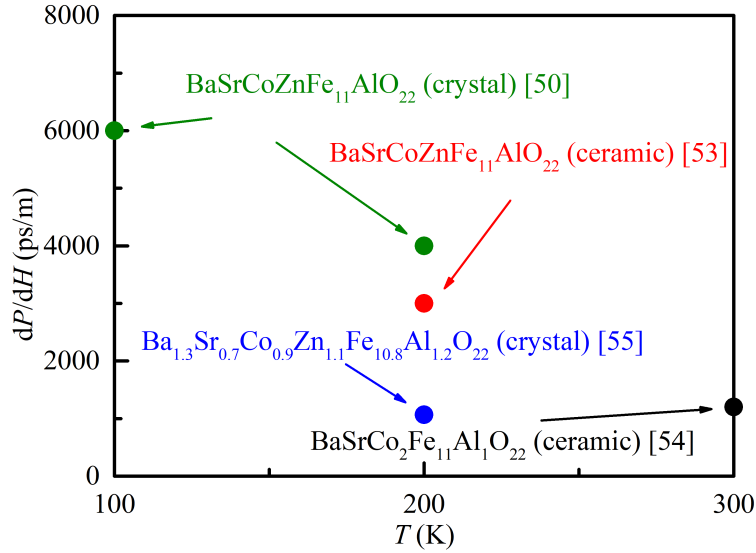


Figure 3.1: Summary of  $dP/dH$  in various Y-type hexaferrites single crystal and poly crystal [52, 55–57].

have recently shown that a  $\text{Ba}_{0.8}\text{Sr}_{1.2}\text{Co}_2\text{Fe}_{11.1}\text{Al}_{0.9}\text{O}_{22}$  single crystal having high resistivity from the oxygen annealing can induce M reversal by  $E$  field control at room temperature [36]. On the other hand, systematic efforts are still lacking to understand how the maximum ME coupling can be obtained with the variation of material properties such as doping and related magnetic phase competition.

In this study, we explore the physical properties of  $\text{Ba}_{2-x}\text{Sr}_x\text{Co}_2(\text{Fe}_{1-y}\text{Al}_y)_{12}\text{O}_{22}$  (BSCFAO) single crystals in order to find the optimal ME coupling strength near room temperature. We have varied the doping ratios  $x$  and  $y$  of those single crystals and have investigated their magnetic, electric, and magnetoelectric properties. We find that the specimen of  $x=1.8$  and  $y=0.04$  exhibits the largest ME susceptibility values at temperatures between 10 and 300 K (  $\sim 25000$  ps/m at 10 K and  $\sim 1000$  ps/m at 300 K). The intrinsic  $P$  induced by  $H$  was successfully measured up to 320 K. Based on systematic studies of magnetic and electrical properties, we point out that the volume fraction and stability of the TC phase is a key to achieving strongest ME coupling in the  $\text{Co}_2\text{Y}$ -type hexaferrites series at both room temperature as well as low temperatures.

## 3.2 Experimental results

### 3.2.1 Crystallographic structure of $\text{Co}_2\text{Y}$ -type hexaferrites

The Z- or Y- type hexaferrites are composed of combination of three crystallographic blocks, i.e., rhombohedral ( $R$ ), spinel ( $S$ ), and tetragonal ( $T$ ) blocks [59, 60]. In particular, one hexagonal unit cell of the Y-type hexaferrite contains only  $S$  and  $T$  blocks as drawn in Fig. 3.2. The  $T$  block is placed at the bottom of

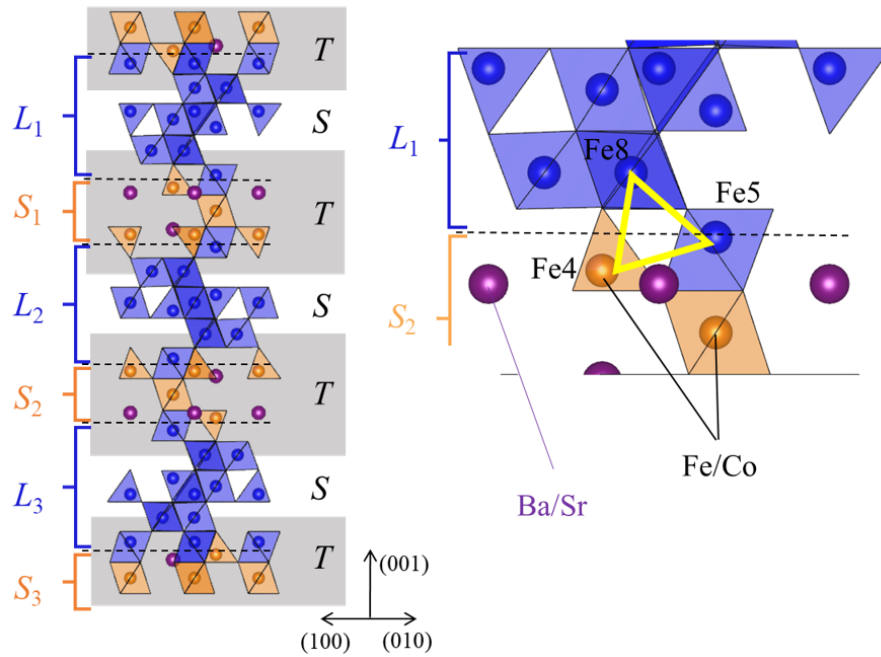


Figure 3.2: The crystal structure of  $\text{Co}_2\text{Y}$ -type hexaferrites (left) and a zoomed-up structure around the interface of the magnetic blocks (right). Both Fe and Co ions are located in the center of the oxygen octahedra or tetrahedra. Orange and blue colors represent the Fe or Co ions located in the magnetic  $L$  and  $S$  blocks, respectively while purple spheres represent the Ba or Sr sites. The yellow triangle indicates the geometrical spin frustration related to helical spin ordering in the  $\text{Co}_2\text{Y}$ -type hexaferrites.

unit cell and the  $S$  block is stacked on top of the  $T$  block. Then,  $T'$  block (' symbol means  $120^\circ$  rotation along  $c$  axis) and another  $S'$  block are also subsequently stacked. After  $S''$  and  $T''$  blocks are piled up again, the unit cell of the Y-type hexaferrites is completed. The spin structure of the Y-type hexaferrite can be also divided into the two major spin moment blocks of Large ( $L$ ) and Small ( $S$ ) as shown in (Fig. 3.2). The chemical substitution in the Fe/Co octahedra and tetrahedra can indeed result in variation of the magnetic anisotropy within the  $L$  and  $S$  blocks, allowing the control of the ME coupling [21].

Fig. 3.3 (a) shows an X-ray diffraction pattern of a ground powder obtained from a typical Y-type hexaferrite single crystal and a fitting curve based on the structural model shown in Fig. 1 (a) by the Rietveld refinement method. These X-ray data analyses have ensured that all the single crystals investigated have exhibited Bragg peaks consistent with the Y-type hexaferrite structure with the  $R\bar{3}m$  space group [59]. As summarized in Fig. 3.3 (b), the lattice constants ( $a$  and  $c$ ) of  $\text{Ba}_{2-x}\text{Sr}_x\text{Co}_2(\text{Fe}_{1-y}\text{Al}_y)_{12}\text{O}_{22}$  obtained from the refinement decrease almost linearly in proportional to Sr ( $x$ ) and Al ( $y$ ) doing ratios. In both Y- and Z-type hexaferrites, it has been known that Sr substitution for Ba results in the smallest  $c$  and  $a$  values, which in turn was useful for making a transverse conical spin ordering most stable. Our results here indicate that not only Sr but also Al substitution allows us to reduce the  $c$  and  $a$  values further. Therefore, simultaneous substitution of both Sr and Al constitutes an effective route to stabilize a transverse conical phase.

Electron probe micro-analysis (EPMA) results are shown in Table 3.1.

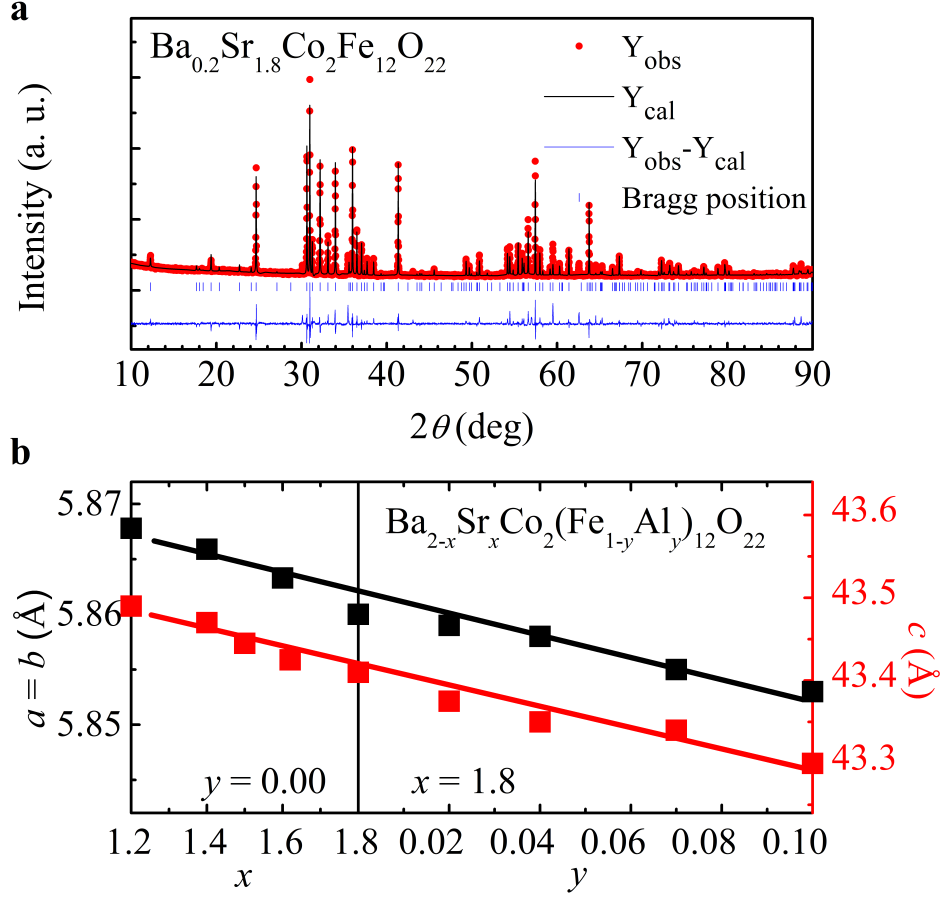


Figure 3.3: (a) An X-ray diffraction pattern of the ground  $\text{Ba}_{0.2}\text{Sr}_{1.8}\text{Co}_2\text{Fe}_{12}\text{O}_{22}$  single crystal powder and its Rietveld refinement result, which verifies the  $R\bar{3}m$  structure. (b) The evolution of  $a$ - and  $c$ -axes lattice constants with Sr ( $x$ ) and Al ( $y$ ) substitution ratios as determined from the X-ray diffraction data and the Rietveld refinement result.

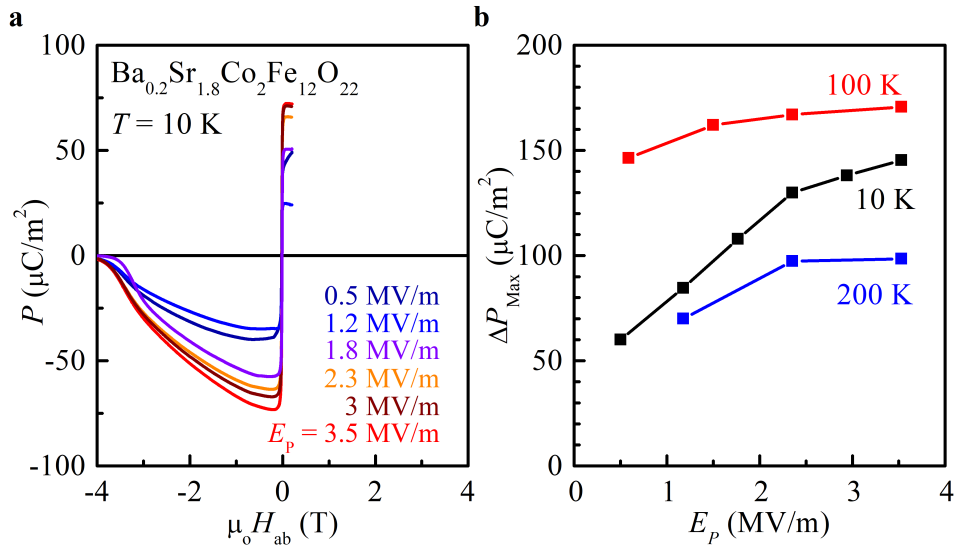
### 3.2.2 Enhancement of magnetoelectric coupling by the Sr and Al substitution

The sample before performing the ME current measurements, a maximum allowed electric field bias  $E_P$  without electrical breakdown (e.g., 3.0 MV/m at 10 K and 2.5 MV/m at 100 K) was applied along the [120] direction in the paraelectric collinear state ( $\mu_0 H = 5$  T) to pole the electric polarization (See the Fig. 3.4 for detailed poling electric fields). Then, the electric field is turned off

Nominal compound	EPMA results
$\text{Ba}_{0.6}\text{Sr}_{1.4}\text{Co}_2\text{Fe}_{12}\text{O}_{22}$	$\text{Ba}_{0.74}\text{Sr}_{1.26}\text{Co}_2\text{Fe}_{12}\text{O}_{22}$
$\text{Ba}_{0.5}\text{Sr}_{1.5}\text{Co}_2\text{Fe}_{12}\text{O}_{22}$	$\text{Ba}_{0.56}\text{Sr}_{1.44}\text{Co}_2\text{Fe}_{12}\text{O}_{22}$
$\text{Ba}_{0.3}\text{Sr}_{1.7}\text{Co}_2\text{Fe}_{12}\text{O}_{22}$	$\text{Ba}_{0.38}\text{Sr}_{1.62}\text{Co}_2\text{Fe}_{12}\text{O}_{22}$
$\text{Ba}_{0.2}\text{Sr}_{1.8}\text{Co}_2\text{Fe}_{12}\text{O}_{22}$	$\text{Ba}_{0.24}\text{Sr}_{1.76}\text{Co}_2\text{Fe}_{12}\text{O}_{22}$
$\text{Ba}_{0.2}\text{Sr}_{1.8}\text{Co}_2(\text{Fe}_{0.96}\text{Al}_{0.04})_{12}\text{O}_{22}$	$\text{Ba}_{0.25}\text{Sr}_{1.75}\text{Co}_2(\text{Fe}_{0.96}\text{Al}_{0.04})_{12}\text{O}_{22}$
$\text{Ba}_{0.2}\text{Sr}_{1.8}\text{Co}_2(\text{Fe}_{0.94}\text{Al}_{0.06})_{12}\text{O}_{22}$	$\text{Ba}_{0.23}\text{Sr}_{1.77}\text{Co}_2(\text{Fe}_{0.93}\text{Al}_{0.07})_{12}\text{O}_{22}$
$\text{Ba}_{0.2}\text{Sr}_{1.8}\text{Co}_2(\text{Fe}_{0.92}\text{Al}_{0.08})_{12}\text{O}_{22}$	$\text{Ba}_{0.24}\text{Sr}_{1.76}\text{Co}_2(\text{Fe}_{0.9}\text{Al}_{0.10})_{12}\text{O}_{22}$

Table 3.1: Nominal chemical formula and EPMA results.

after  $H$  is reduced to become a ferroelectric state ( $\mu_0 H = 0.2$  T). Electric-field poling  $E_P$  dependence of polarization at 10 K is shown in Fig. 3.4 (a). Similar curves were obtained at 10, 100, and 200 K. Both at 10 and 100 K, electric polarization is saturated at high electric field poling around 3 MV/m above. The polarization at various temperature range is summarized in Fig. 3.4 (b). When the transverse cone phase becomes dominant, the ferroelectric polarization becomes maximized in this hexaferrite. In order to extract the intrinsic electric


 Figure 3.4: (a) Electric-field poling  $E_P$  dependence of polarization at 10 K. (b) Summary of the polarization at 10 K, 100 K, and 200 K.

polarization induced by the transverse cone phase, application of  $E_P$  around 3 MV/m above is presumably required at low temperatures. On the other hand, at high temperatures around 200 K, the diminishing TC phase result in the reduction of induced electric polarization value as well as smaller variation with respect to  $E_P$  variation (10 % variation of  $\Delta P_{max}$  for  $\sim 2.2 \text{ MV/m} \leq E_P$ ). Therefore, in order to reduce a risk of having electrical breakdown effects in a specimen coming from the increased leakage at high temperatures, we have varied  $E_P$  to obtain  $P(H)$  curves at each temperature; 3 MV/m at 10 K, 2.5 MV/m at 100 K, 2.0 MV/m at 200 K, and 0.5 MV/m at 300 K.

Fig. 3.5 summarizes the variations of electric polarization  $P$  and ME susceptibility  $dP/dH$  in the single crystals of  $\text{Ba}_{2-x}\text{Sr}_x\text{Co}_2(\text{Fe}_{1-y}\text{Al}_y)_{12}\text{O}_{22}$ , which have been obtained from the integration of the ME current data at various temperatures between 10 and 300 K. Fig. 3.5 (a) first exhibits the  $P \parallel [120]$  variation with respect to  $H \parallel [100]$  measured with either increasing or decreasing  $H$  after the ME poling at  $H = 0.1 \text{ T}$ . At a low temperature 10 K, the  $P$  vs  $H$  curve typically exhibits a sharp increase (decrease) of  $P$  at a small positive (negative)  $H$  bias, resulting in a very asymmetric line shape that changes the sign of  $P$  with respect to  $H$  direction reversal. This is a characteristic  $P$  vs  $H$  curve that has also been realized in an archetypal magnetoelectric Y-type hexaferrite, formula at 10 K [47, 48].

To understand how such phase competition and thermal/magnetic stability of the TC phase can affect the electrical properties, we have compared the ME effects quantitatively in the series of  $\text{Ba}_{2-x}\text{Sr}_x\text{Co}_2(\text{Fe}_{1-y}\text{Al}_y)_{12}\text{O}_{22}$ . First of all, it is clearly found in Fig. 3.5 (a) that as  $x$  is increased, a sudden increase of  $P$  at 10 K at a small  $H$  bias becomes systematically increasing, finally exhibiting almost a maximum at  $x=1.6-1.8$ . Moreover,  $x=1.8$  compound still exhibits most

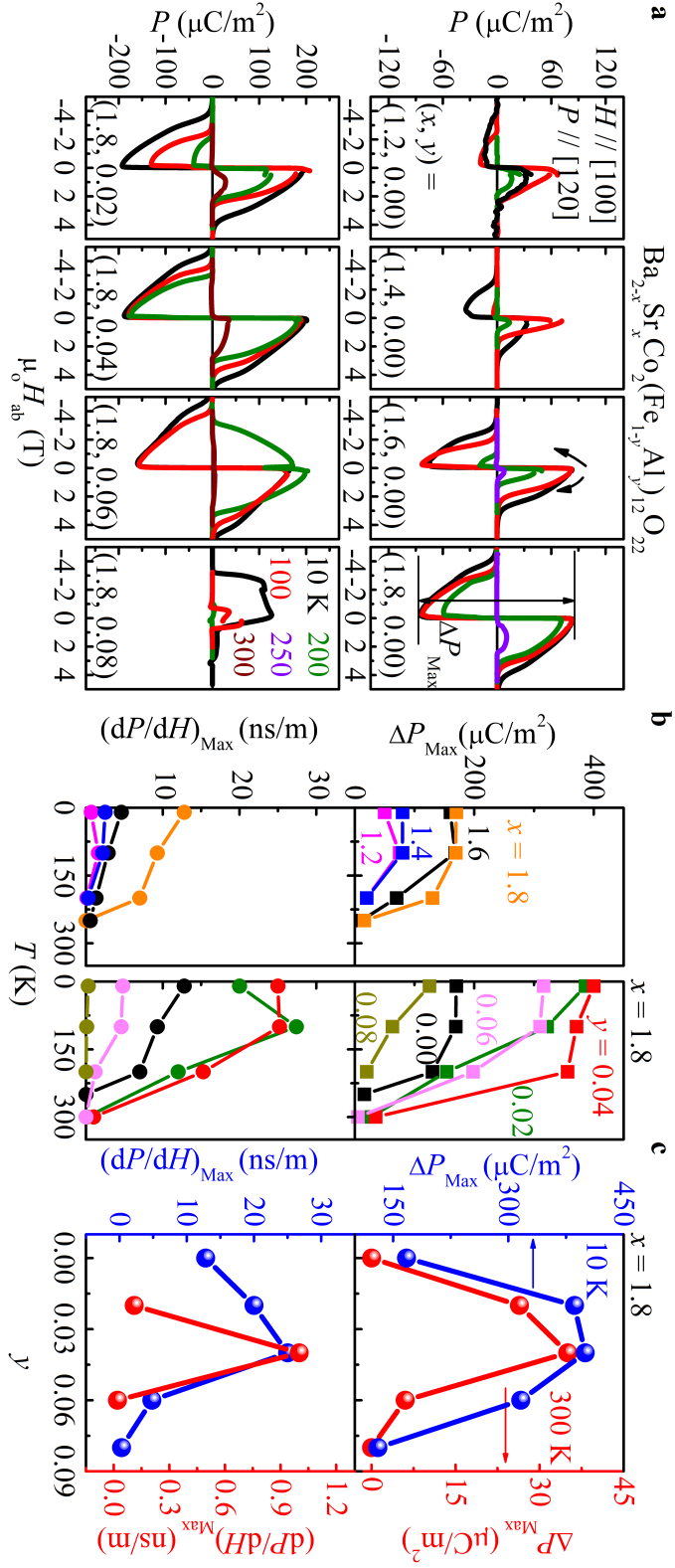


Figure 3.5: (a) Magnetic-field dependent electric polarization of  $\text{Ba}_{2-x}\text{Sr}_x\text{Co}_2(\text{Fe}_{1-y}\text{Al}_y)_{12}\text{O}_{22}$  single crystals.  $\Delta P_{\text{max}}$  indicates the difference between extreme values,  $P_{\text{max}} - P_{\text{min}}$ . Electric polarization is calculated from the integration of the ME current. (b) Temperature-dependence of  $\Delta P_{\text{max}}$  and maximum  $dP/dH$  values. (c) Summary of  $\Delta P_{\text{max}}$  and maximum  $dP/dH$  as a function of  $y$  at 10 K and 300 K, demonstrating that the specimen with  $x = 1.8$  and  $y = 0.04$  has the largest magnetic field induced polarization at both temperatures.



### 3.2. Experimental results

---

asymmetric  $P$  vs  $H$  line shape even at 200 K. To quantify the ME coupling strength, we have thus defined  $\Delta P_{max}$  and  $(dP/dH)_{max}$ ;  $\Delta P_{max}$  represents the difference between the extrema of  $H$ -induced  $P$ ,  $P_{max}-P_{min}$ , and  $(dP/dH)_{max}$  represents the maximum of  $dP/dH$  near zero but at a finite field.

Based on the two quantities, we find that sample with  $x=1.8$  in the series of  $\text{Ba}_{2-x}\text{Sr}_x\text{Co}_2(\text{Fe}_{1-y}\text{Al}_y)_{12}\text{O}_{22}$  exhibits the strongest ME coupling at overall temperatures up to 250 K (Fig. 3.5). Although  $\Delta P_{max}$  is quite similar in both  $x=1.6$  and 1.8 below 200 K,  $\Delta P_{max}$  at 250 K becomes maximum at  $x=1.8$ . Moreover,  $(dP/dH)_{max}$  observable up to 250 K also becomes maximum at  $x=1.8$ . The enhancement of  $\Delta P_{max}$  and  $(dP/dH)_{max}$  at  $x=1.8$  compound is closely coined to the most asymmetric  $P$  vs  $H$  lineshape maintained up to high temperature of 200 K, indicating the field-induced stabilization of the TC phase is a key to the enhancement. With such a Sr ratio of  $x=1.8$ , variation of the three O-Fe-O bonding angles at the interface between the structural T and S blocks (Fig. 3.2, right panel) and resultant spin frustration among the three superexchange interactions are likely optimized for firstly leading to the longitudinal conical spin state (the ALC phase) at zero field. At the same time, the compound with Sr  $x=1.8$  compound should also have an optimized field-induced metastability of the TC phase after the FC process over other compounds with different  $x$ , which can then explain the maximized  $\Delta P_{max}$  and  $(dP/dH)_{max}$  [24, 59]. Although a larger Sr concentration  $x$  may further optimize the spin frustration to increase the stability of the ALC phase at zero field and the field-induced metastability of the TC phase, we could not obtain high quality single crystals with  $x > 1.8$  because of the presence of large amount of  $\text{Fe}_2\text{O}_3$  and M-type hexaferrite impurities. Therefore, we have chosen  $x=1.8$  to investigate the effects of Al doping to see whether the ME properties can be further optimized.

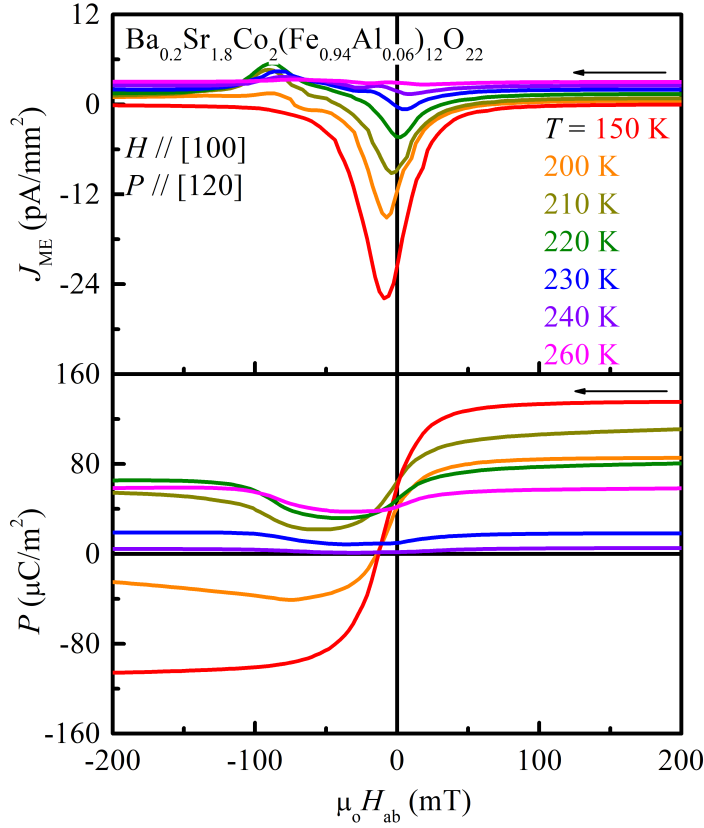


Figure 3.6: (up) ME current and (down) electric polarization of  $x=1.8$  and  $y=0.06$  compound at low magnetic field region above 150 K.

As aluminum Al is substituted to form  $\text{Ba}_{0.2}\text{Sr}_{1.8}\text{Co}_2(\text{Fe}_{1-y}\text{Al}_y)_{12}\text{O}_{22}$ , it is surprisingly found that  $P$  induced by a small  $H$  bias suddenly increases to result in even more sharp increase of  $\Delta P_{max}$  and  $(dP/dH)_{max}$  at overall temperatures. In particular, Al concentration  $y=0.02-0.06$  exhibits most enhanced  $\Delta P_{max}$  and  $(dP/dH)_{max}$  as compared with those of the Al-undoped specimen,  $\text{Ba}_{0.2}\text{Sr}_{1.8}\text{Co}_2\text{Fe}_{12}\text{O}_{22}$ . On the other hand, as Al is increased further up to e.g.  $y=0.06-0.08$ , there is a general tendency that  $P$  vs  $H$  curve is not reversed even at 200 K, exhibiting symmetric lineshape. For example, the  $P$  vs  $H$  curve becomes almost symmetric at  $y=0.06$  compound at 200 K (Fig. 3.6). The results indicate that Al substitution does not only monotonically enhance the ME coupling via

the increase of the meta-stability of TC phase after the FC process. Instead, at higher Al doping ranges of  $y=0.06-0.08$  and at high temperatures above  $\sim 200$  K,  $P$  reversal with the  $H$  direction change is suppressed slowly, presumably coined to a decrease of the field-induced TC phase in its volume fraction. As a result, the optimal volume fraction and thermal stability of the field-induced TC phase seem to be realized in a specimen of  $y=0.04$ . We indeed find that both  $\Delta P_{max}$  and  $(dP/dH)_{max}$  become maximum values at  $y = 0.04$  at overall temperatures as summarized in Fig. 3.5 (c).  $\Delta P_{max}$  is optimized as  $430 \mu\text{C}/\text{m}^2$  at 10 K and  $37 \mu\text{C}/\text{m}^2$  at 300 K while  $(dP/dH)_{max}$  is  $25000 \text{ ps}/\text{m}$  at 10 K and  $1000 \text{ ps}/\text{m}$  at 300 K.

#### 3.2.3 The metastability of the transverse conical state

Such asymmetric lineshape in  $P$  vs  $H$  curve is closely associated with the field-history dependent stabilization of the TC phase, thus called ‘metastable’ here. Several neutron diffraction studies [45,50,51,61] on  $\text{Ba}_{0.5}\text{Sr}_{1.5}\text{Zn}_2(\text{Fe}_{0.92}\text{Al}_{0.08})_{12}\text{O}_{22}$ ,  $\text{Ba}_{0.3}\text{Sr}_{1.7}\text{Co}_2\text{Fe}_{12}\text{O}_{22}$  and similar Y-type hexaferrites have indeed shown that the TC phase becomes stabilized at a field increasing measurement up to 3 T after suppressing the ALC phase existing at the zero field. Surprisingly the TC phase remains robust even after turning-off the field without returning to the ALC phase. This implies that upon the field being decreased, the TC phase once stabilized at a high field above  $\sim 1$  T is subject to only in-plane rotation at a lower field region as the magnetic easy axis of the TC phase prefers to staying in the  $ab$ -plane.

However, as temperature is increased, the asymmetric line shape of the  $P$  vs  $H$  curve becomes increasingly symmetric. At 300 K, most of  $P$  vs  $H$  curves

exhibit a positive  $P$  at a positive  $H$  bias. Upon the ME poling being performed at  $H = -0.1$  T,  $P$  exhibits a positive value even at negative  $H$  bias, resulting in almost symmetric  $P$  vs  $H$  curve (not shown). (Note that almost zero  $P$  at a negative  $H$  bias in Fig. 3.5 (a) is due to the lack of a proper poling at the negative  $H$  region in the  $H$  sweep process.) This observation at high temperatures around 300 K implies that the rotation axis of the TC phase is increasingly subject to the rotation via the  $c$ -axis in the field decreasing run, resulting in more and more the stabilization of the ALC phase at low fields near the zero field (see Fig. 3.7 for spin patterns). Therefore, it is concluded that the metastable TC phase realized

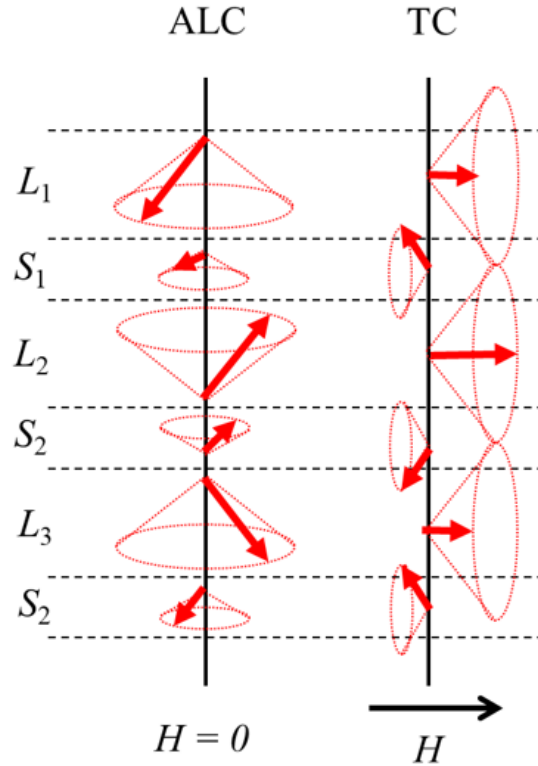


Figure 3.7: A pictorial representation of spin configuration of the  $\text{Co}_2\text{Y}$ -type hexaferrites without (left) and with (right) application of an in-plane magnetic field ( $H_{ab}$ ). ALC refers to an alternative conical spin ordering pattern and TC represents a transverse conical spin ordering pattern.

after turning-off the field mostly remains stable at low temperatures, while the ALC phase becomes increasingly stabilized at high temperatures in competition with the TC phase.

The volume fraction or stability of the TC phase can be indeed proportional to the net magnetic moment remaining after field cooling as the TC phase essentially exhibits a large moment while the ALC phase with antiferromagnetic spin configuration exhibits quite a small magnetic moment. In order to investigate whether such metastable nature of the TC phase over the ALC phase can be

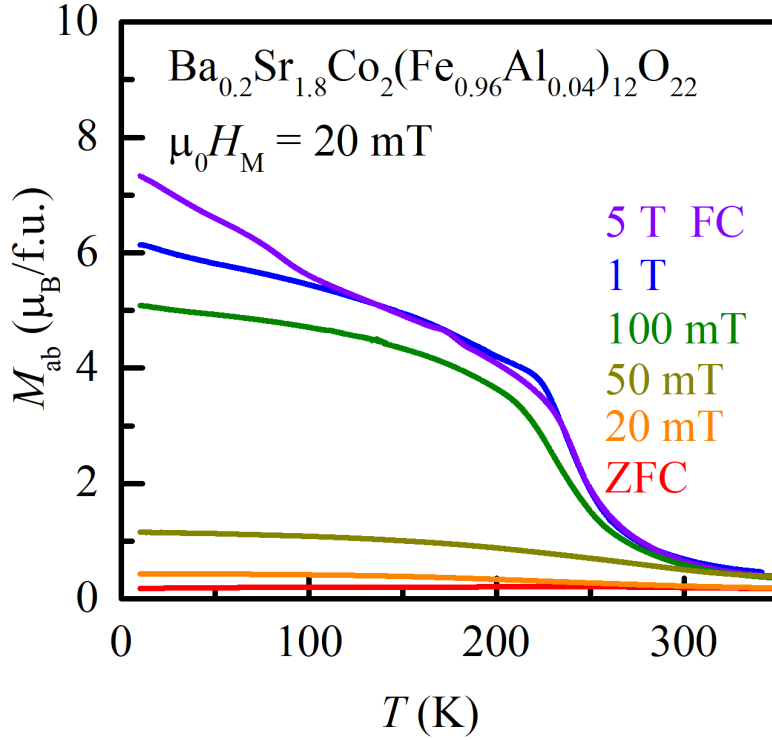


Figure 3.8: In-plane magnetization  $M_{ab}$  data of  $\text{Ba}_{0.2}\text{Sr}_{1.8}\text{Co}_2(\text{Fe}_{0.96}\text{Al}_{0.04})_{12}\text{O}_{22}$  from 10 K to 350 K measured at 20 mT after field cooling with various magnetic field applications conditions, demonstrating the metastable nature of competing phases in the  $\text{Co}_2\text{Y}$ -type hexaferrites.  $M_{ab}$  measured during the warming process under the bias magnetic field  $\mu_0 H_M = 20 \text{ mT}$  after cooling with finite (FC) and zero (ZFC) magnetic field.

persistent in all the BSCFAO series studied here, we have thus investigated temperature dependent in-plane magnetic moment  $M_{ab}$  at a small bias field of 20 mT (warming) after applying various field cooling processes. A typical measurement for  $\text{Ba}_{0.2}\text{Sr}_{1.8}\text{Co}_2(\text{Fe}_{0.96}\text{Al}_{0.04})_{12}\text{O}_{22}$  is summarized in Fig. 3.8. The field cooling (FC) approximately above 100 mT indeed results in quite high  $M_{ab}$  values while the  $M_{ab}$  after a zero field cooling (ZFC), implying that the TC phase becomes metastable mostly after field cooling process above 100 mT while the ZFC makes the ALC phase stable dominantly near the zero field regions. Moreover, for the FC curves above 100 mT up to 5 T,  $M_{ab}$  measured at a very small bias field of 20 mT remain nearly similar high values, suggesting that the field cooling above 100 mT and up to  $\sim 5$  T is nearly enough to make the TC phase metastable dominantly. We found that all the  $\text{Ba}_{0.2}\text{Sr}_{1.8}\text{Co}_2(\text{Fe}_{1-y}\text{Al}_y)_{12}\text{O}_{22}$  series studied here have such metastable nature (See, Fig. 3.9). It is noted in Fig. 3.9 that the  $M_{ab}$  curves after FC at 5 T and ZFC becomes most conspicuously different in the  $y=0.04$  compound among  $\text{Ba}_{0.2}\text{Sr}_{1.8}\text{Co}_2(\text{Fe}_{0.96}\text{Al}_{0.04})_{12}\text{O}_{22}$ ; the difference between the  $M_{ab}$  values at 10 K is the largest and the temperature where the FC 5 T curve starts to increase and is located at the highest temperature. Therefore, it is concluded that the volume fraction and temperature stability of the TC phase remaining after FC becomes highest in the  $y=0.04$  compound.

The metastable nature of the TC phase in competition with the ALC phase found in a broad doping ranges of  $\text{Ba}_{0.2}\text{Sr}_{1.8}\text{Co}_2(\text{Fe}_{1-y}\text{Al}_y)_{12}\text{O}_{22}$  can be summarized as temperature- dependent free energy behavior shown in Fig. 3.10. Upon being cooled down at zero field ((1) ZFC), the system mostly remains in the ALC phase, of which stability sensitively depends on the spin frustration as well as magnetic anisotropy. As soon as the field is applied up to 5 T at low temperatures, the system is chosen to stay at the TC phase that forms a minimum in the

### 3.2. Experimental results

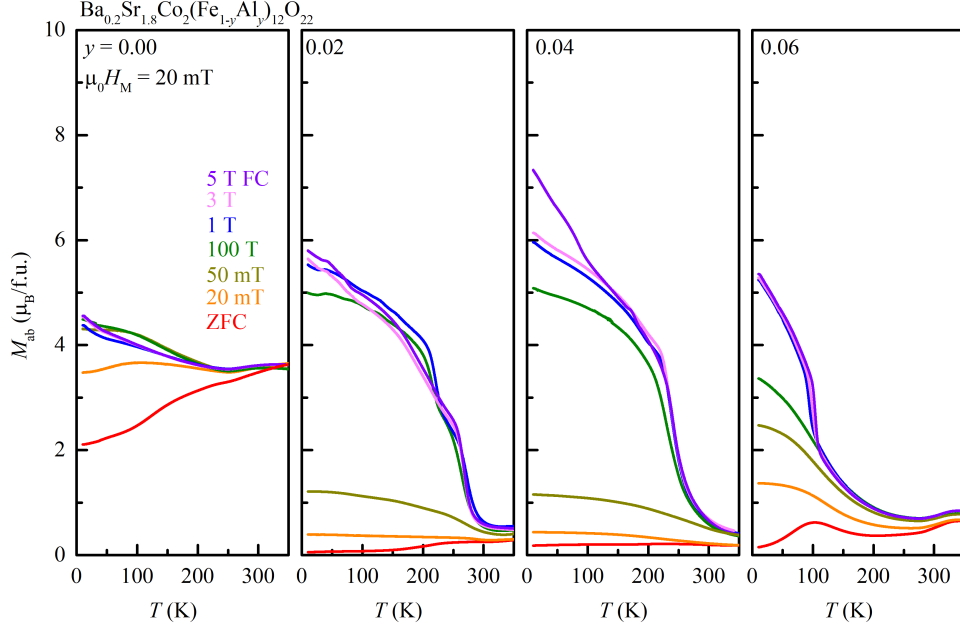


Figure 3.9: The  $M_{ab}$  for various doping ratio. The red curve and black curves are  $M_{ab}$  of  $\text{Ba}_{0.2}\text{Sr}_{1.8}\text{Co}_2(\text{Fe}_{1-y}\text{Al}_y)_{12}\text{O}_{22}$  measured under  $\mu_0 H_M = 20$  mT during the warming process after various magnetic field applications conditions.

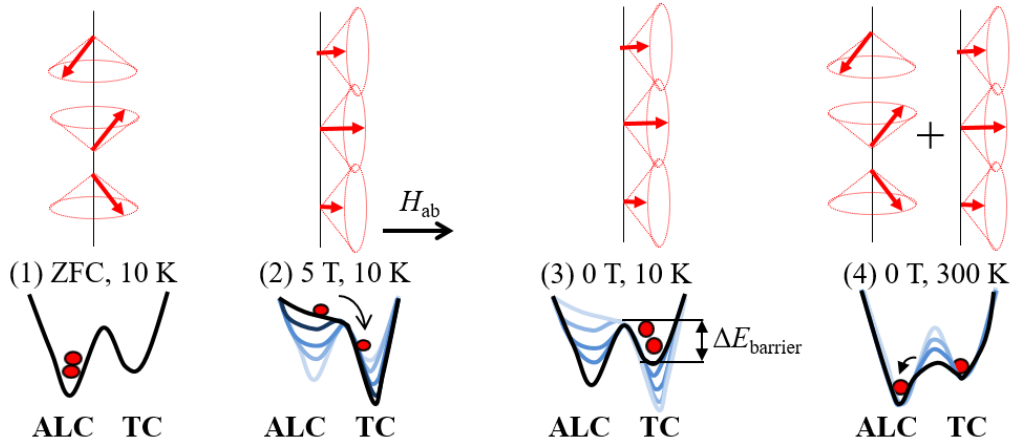


Figure 3.10: Pictorial descriptions for a dominant spin configurations and.  $L$  and  $S$  mean the magnetic  $L$  and  $S$  blocks as shown in Fig. 3.7. The spin state of  $S$  block is omitted for clarity.

free energy under magnetic field ((2) 5 T, 10 K). Upon the field being turned off, the system still remains at the TC phase at 10 K as the barrier height  $\Delta E_{\text{barrier}}$  between the TC and ALC phase is high enough to block the phase changes at low temperatures((3) 0 T, 10 K). When temperature is raised again, the system can populate both the ACL and the TC phase by thermal excitation, in which volume fraction of each phase depends on  $\Delta E_{\text{barrier}}$  between the two phases ((4) 300 K). According to this picture, the  $y=0.04$  compound is expected to a most sharp and deep potential shape in the TC phase relative to that of the ALC phase so that the volume fraction and thermal stability of the TC phase becomes highest.

The neutron scattering experiment of  $\text{Ba}_{0.2}\text{Sr}_{1.8}\text{Co}_2(\text{Fe}_{0.96}\text{Al}_{0.04})_{12}\text{O}_{22}$  also supports that  $\Delta E_{\text{barrier}}$  is enhanced by Al substitution. In the case of the Al-undoped specimen  $\text{Ba}_{0.2}\text{Sr}_{1.8}\text{Co}_2\text{Fe}_{12}\text{O}_{22}$ , incommensurate  $k = (0,0,\delta)$  peak (ALC) starts to evolve and is mixed with the commensurate  $k=(0, 0, 3/2)$  peak (TC) in the zero-field above 120 K [51]. However, Fig. 3.11 indicates that the incommensurate  $k = (0,0,\delta)$  peak (ALC) of Al-doped specimen  $\text{Ba}_{0.2}\text{Sr}_{1.8}\text{Co}_2(\text{Fe}_{0.96}\text{Al}_{0.04})_{12}\text{O}_{22}$  emerges above 220 K, much higher than that of Al-undoped sample.

Fig. 3.12 exhibits another evidence of the metastability of the TC phase. ME susceptibility  $dP/dH$ , so-called  $\alpha_{MES}$ , is measured with AC method [42]. If the AC method is used, the  $\alpha_{MES}$  can be measured continuously without sweeping the magnetic field or temperature. The magnetic structure is mostly stabilized to the TC phase after the poling procedure. However, the TC phase exists in the local minima of the free energy (metastable phase) while the ALC is a ground state which placed in the global minima of the free energy (most-stable phase) at zero magnetic field. Depending on the energy barrier between the TC and ALC phase ( $\Delta E_{\text{barrier}}$ ), the TC phase moves to ALC by the tunneling effect. Interestingly, the up-panel of Fig. 3.12 indicates that  $\alpha_{MES}$  decays as time goes on near 0 T (9



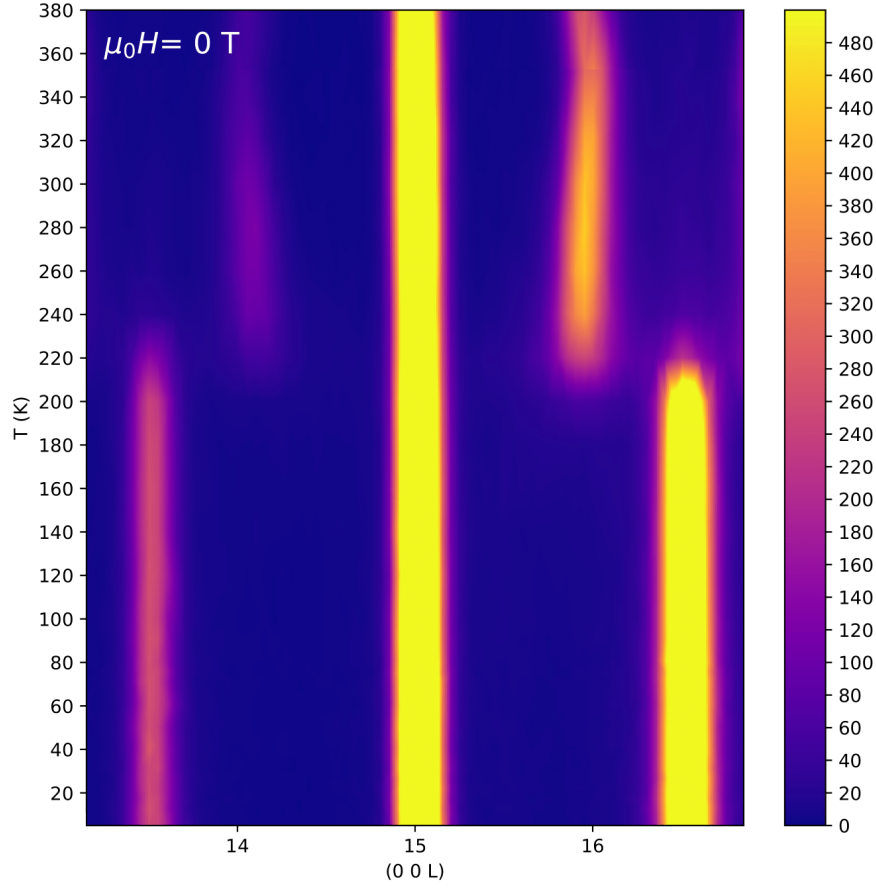


Figure 3.11: The change of the Bragg peak intensities under warming the sample in zero field after applying 3.0 T along  $ab$ -plane at 10 K.

mT), whereas  $\alpha_{MES}$  at 1.5 T, corresponding to the (2) configuration in Fig. 3.10 is constant. This result strongly supports that the existence of metastability in the  $\text{Ba}_{0.2}\text{Sr}_{1.8}\text{Co}_2(\text{Fe}_{0.96}\text{Al}_{0.04})_{12}\text{O}_{22}$ .

### 3.2.4 Magnetic properties of $\text{Co}_2\text{Y}$ -type hexaferrites

It is known in  $\text{Ba}_{0.5}\text{Sr}_{1.5}\text{Zn}_2(\text{Fe}_{1-y}\text{Al}_y)_12\text{O}_{22}$  [21, 22] that nonmagnetic  $\text{Al}^{3+}$

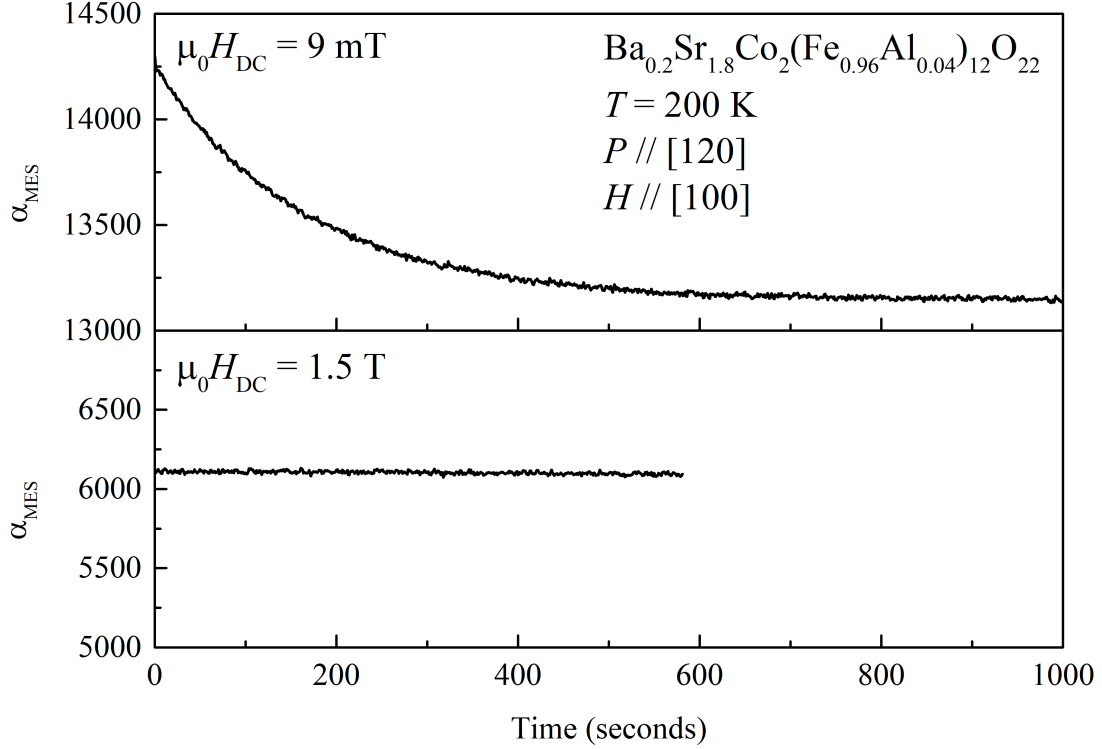


Figure 3.12: AC ME susceptibility  $\alpha_{\text{MES}}$  as a function of time under static 9 mT (up) and 1.5 T (down) after the poling procedure.

ions prefer to occupying the octahedral sites to result in reduction of the in-plane orbital angular momentum,  $L_{ab}$ , of the  $\text{Fe}^{3+}$  ions, particularly in the off-centered octahedral site. Such reduction in  $L_{ab}$  is a source of a decrease in the in-plane magnetic anisotropy with Al substitution, hence resulting in the change of the spin structure from the proper screw type with in-plane magnetic moment only to the longitudinal conical spin structure with the local  $c$ -axis spin component. In the case of  $\text{Ba}_{0.2}\text{Sr}_{1.8}\text{Co}_2\text{Fe}_{12}\text{O}_{22}$ , magnetic circular dichroism (MCD) measurements at the Fe  $L_{2,3}$  edge have revealed that the  $\text{Co}^{2+}$  ions also prefer to going into the octahedral site and yields out-plane angular momentum  $L_c$ , making additional magnetic moment component tend to become parallel to the  $c$ -axis. As a result,

the  $\text{Co}^{2+}$  ion not only stabilizes the ALC phase having a local  $c$ -axis moment but also increases the superexchange interaction strengths (possibly via the Co-O-Fe path) to increase the spin ordering temperatures of the ALC phase above room temperatures as compared with those of the corresponding  $\text{Zn}_2\text{Y}$  type specimen, e.g.  $\text{Ba}_{0.5}\text{Sr}_{1.5}\text{Zn}_2\text{Fe}_{12}\text{O}_{22}$  [21]. As a final result,  $\text{Ba}_{0.2}\text{Sr}_{1.8}\text{Co}_2(\text{Fe}_{1-y}\text{Al}_y)_{12}\text{O}_{22}$  is expected to have not only weakened  $L_{ab}$  due to  $\text{Al}^{3+}$  substitution but also the increased  $L_c$  due to the  $\text{Co}^{2+}$  substitution. According to this picture,  $\text{Al}^{3+}$  substitution to make  $\text{Ba}_{0.2}\text{Sr}_{1.8}\text{Co}_2(\text{Fe}_{1-y}\text{Al}_y)_{12}\text{O}_{22}$  seems to allow us to achieve fine control of the interplay between the in-plane and the out-of-plane magnetic anisotropy. Moreover, the Al substitution into one of three octahedral Fe sites represented in Fig. 3.2 can also affect the degree of spin frustration via the spin dilution effect as well as the bond angle change at the interface. Such a delicate control of magnetic anisotropy as well as the degree of spin frustration could be crucial to stabilize the ALC phase (at  $H_{ab} = 0$ ) and TC phase (at  $H_{ab} \neq 0$ ) up to high temperatures to optimize the ME coupling near room temperature.

To find a clue on the interplay between  $ab$ -plane and  $c$ -axis magnetic anisotropy, we have systematically investigated the temperature dependence of the in-plane ( $M_{ab}$ ) and out-of-plane magnetization ( $M_c$ ) at high temperature range ( $300 \text{ K} < T < 800 \text{ K}$ ) after the ZFC process (Fig. 3.13). In the Al-free specimen  $\text{Ba}_{0.2}\text{Sr}_{1.8}\text{Co}_2\text{Fe}_{12}\text{O}_{22}$ , both  $M_{ab}$  and  $M_c$  exhibits a step-like increase at  $T^*=750 \text{ K}$ , which is also observed at almost same temperatures in most of the specimen with Al substitution. As this transition is nearly independent of Al substitution and no appreciable impurity phase is observed in our single crystals, the transition is likely related to the local spin ordering coming from one of Fe-O-Fe superexchange paths; upon  $\text{Co}^{2+}$  being located dominantly in the octahedral site,  $\text{Fe}^{3+}$  in the tetrahedral sites can form the superexchange path between neighboring

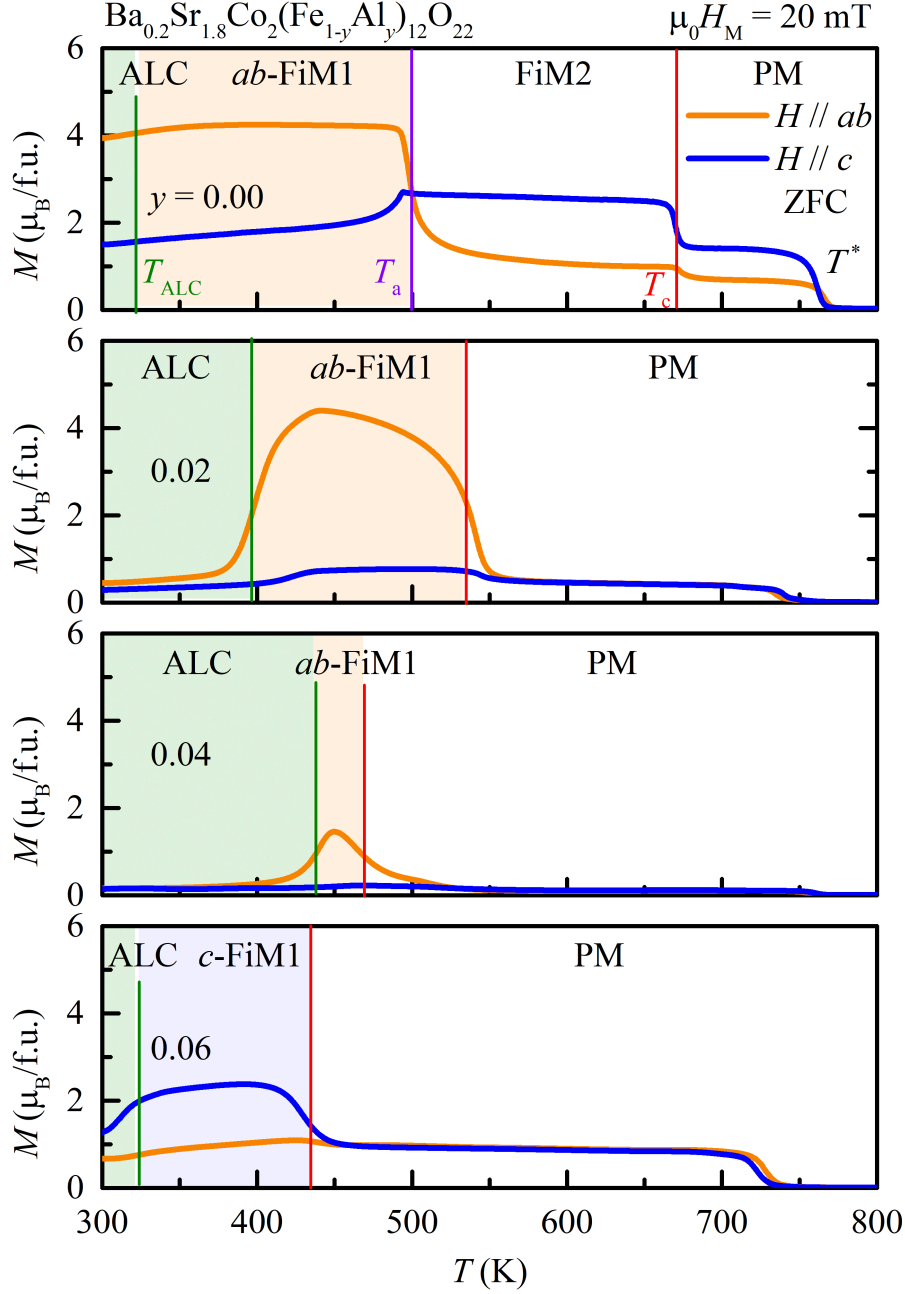


Figure 3.13: Magnetization curve along  $ab$ - (orange) and  $c$ - (blue) direction measured in the application of  $\mu_0 H_M = 20$  mT during the warming process after ZFC.

### 3.2. Experimental results

---

$\text{Fe}^{2+}$  or  $\text{Fe}^{3+}$  in the octahedral sites via the oxygen so that a local ferrimagnetic spin ordering may occur as similarly observed in other iron oxides e.g. in the magnetite at 850 K [23].

As a result, Magnetic phases are divided into 5 phases; ALC, *ab*-FiM1 (ferrimagnet along *ab*-plane), *c*-FiM1 (ferrimagnet along *c*-axis), FiM2 (canted ferrimagnet tilted between *ab*-plane and *c*-axis), and PM (paramagnet). ALC, *ab*-FiM1, and *c*-FiM1 phases are highlighted by green, orange, and blue shadows respectively in Fig. 3.13. The  $T_{\text{ALC}}$  (green solid line) denotes the transition temperature from ALC to the FiM1 phases.  $T_a$  indicates the temperature of magnetic anisotropy transition from the *ab*-plane to the tilted direction.  $T_c$  is the Curie temperature, at which the ferrimagnet changes to the paramagnet.

A relevant long-range ferrimagnetic spin ordering between the effective magnetic *L* and *S* blocks in  $\text{Ba}_{0.2}\text{Sr}_{1.8}\text{Co}_2\text{Fe}_{12}\text{O}_{22}$  is attributed to the step-like feature observed at  $T_c = 670$  K (Fig. 3.13). Note that for  $\text{Ba}_2\text{Co}_2\text{Fe}_{12}\text{O}_{22}$ , a similar transition has been identified at  $T_c = 613$  K [60]. We find that  $T_c$  in  $\text{Ba}_{0.2}\text{Sr}_{1.8}\text{Co}_2\text{Fe}_{12}\text{O}_{22}$  is systematically reduced with the increase of Al substitution ratio (*y*) as indicated by the red solid lines in Fig. 3.14;  $T_c = 670, 541, 463,$  and  $438$  K for  $y = 0.00, 0.02, 0.04,$  and  $0.06$ , respectively. This is consistent with expectation that the spin dilution effect with Al substitution makes the overall transition temperatures decrease. The red solid symbols in the phase diagram summarized in Fig. 3.14 well summarize this trend.

Another notable feature below  $T_c$  is that the magnitudes of  $M_{ab}$  and  $M_c$  measured at a bias field of  $\mu_0 H_M = 20$  mT are varied with the Al doping ratio *y* or temperature; in the  $y = 0.00$  specimen,  $M_c = 2.5 \mu_B/\text{f.u.}$  and  $M_{ab} = 1.0 \mu_B/\text{f.u.}$  just below  $T_c$  and then  $M_c = 1.8 \mu_B/\text{f.u.}$   $M_{ab} = 4.0 \mu_B/\text{f.u.}$  below  $T = 495$  K, showing that the ferrimagnetic moment was initially pointing dominantly along

the  $c$ -axis with considerable  $ab$ -plane component. Then, a magnetic anisotropy transition, defined as  $T_a$ , occurs at 495 K to let the  $ab$ -plane become an easy plane. We thus assign the phase below  $T_a = 498$  K as a ferrimagnetic phase with dominant alignment along the  $a$ -axis, i.e.,  $ab$ -FiM1 and the phase above  $T_a$  as a tilted ferrimagnetic phase FiM2. In the  $y = 0.02$  and  $0.04$  specimens, a similar  $ab$ -FiM1 phase with dominant  $M_{ab}$  moment is realized immediately below  $T_c$ . Finally, in the  $y=0.06$  specimen, a ferrimagnetic phase with dominant  $M_c$  component, thus defined as  $c$ -FiM1, is realized at  $T_c = 438$  K.

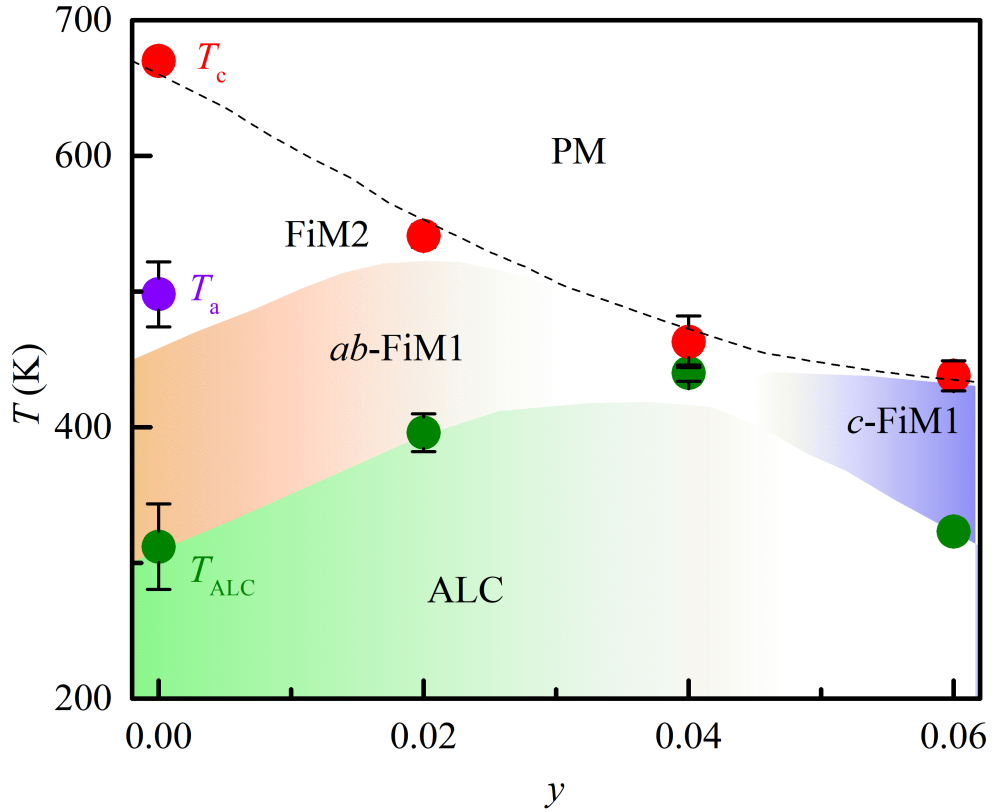


Figure 3.14: Magnetic phase diagram constructed from the magnetization curve. Red arrows represent the spin structures in the phases. Long and short arrows denotes the spin in  $L$  and  $S$  blocks, respectively. ALC,  $ab$ -FiM1, and  $c$ -FiM1 phases are painted in green, red, and blue colors to coincide with the Fig. 3.13. The black dashed line denotes the paramagnetic phase for guides to the eye.

### 3.2.5 Ferroelectricity and its phase diagram

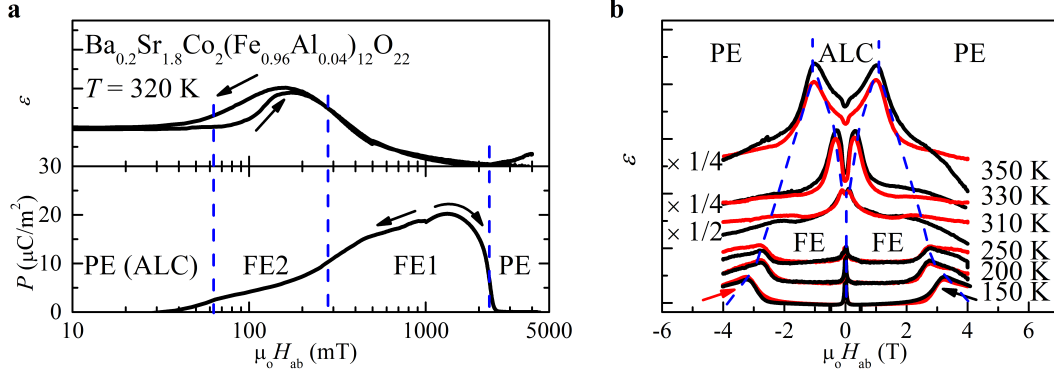


Figure 3.15: (a) Variation of dielectric constant and electric polarization as a function of magnetic fields at 320 K in the  $\text{Ba}_{0.2}\text{Sr}_{1.8}\text{Co}_2(\text{Fe}_{0.96}\text{Al}_{0.04})_{12}\text{O}_{22}$  crystal. (b) Magnetic-field dependent dielectric constant variation at wide temperatures in the same crystal. The red (black) curve was measured while magnetic field is increasing (decreasing). Blue dotted lines are for guides to the eye.

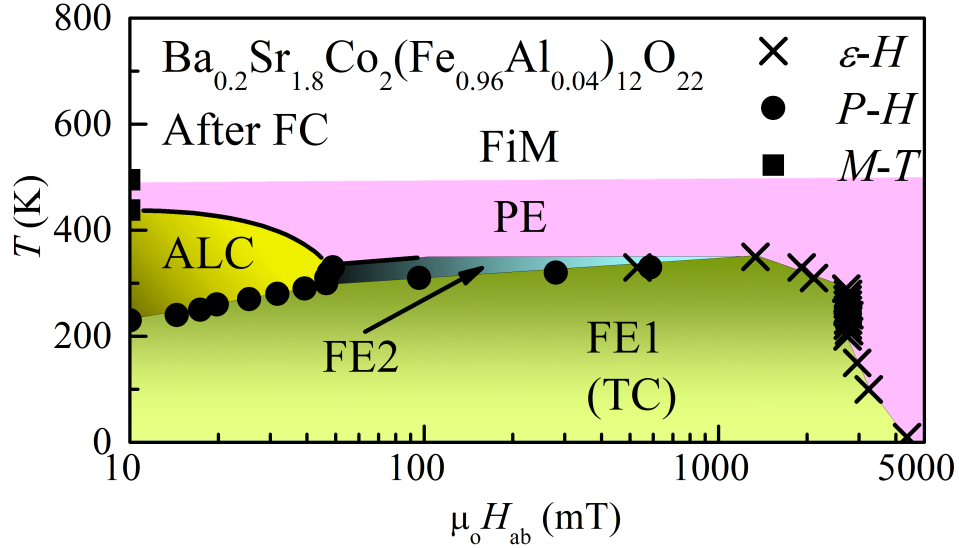


Figure 3.16: Phase diagram of  $\text{Ba}_{0.2}\text{Sr}_{1.8}\text{Co}_2(\text{Fe}_{0.96}\text{Al}_{0.04})_{12}\text{O}_{22}$  single crystal constructed from the dielectric constant, magnetic field-induced polarization, and magnetization measurement.

To further understand the effects of  $\text{Al}^{3+}$  substitution, we have determined phase boundaries of a  $\text{Ba}_{0.2}\text{Sr}_{1.8}\text{Co}_2(\text{Fe}_{1-y}\text{Al}_y)_{12}\text{O}_{22}$  crystal from the dielectric constant and electric polarization data. Fig. 3.15 presents experimental data used to determine each phase at 320 K. The left panel of Fig. 3.15 (a) shows the dielectric constant and  $P$  with variation of  $H$ . As described in other literatures [51, 59], the paraelectric (PE) state at high fields coincides with a collinear spin state. The other paraelectric (PE) phase at low field regions should then result from the ALC state. The ferroelectric (FE) states induced by the TC phase can appear between the two different PE states. We notice that increase of  $P$  with  $H$  occurs in two different steps, which is assigned here as FE1 and ME current shows clear anomaly with an emergence of FE2 state near room temperature, as depicted in Fig. 3.16. The FE1 state is characterized with the large  $P$  state induced by  $H$  and is likely to be associated with  $P$  induced by the TC phase under the magnetic field via the spin current mechanism i.e. inverse DM effect. The other FE2 state seems only stable under finite fields and between the collinear Ferrimagnetic (Ferri) state and the FE1 (TC) state. This state allowed with enough thermal fluctuation at finite field and temperature windows might be related to the canted TC phase or canted ALC phase (Fig. 3.17). The right panel of Fig. 3.15 (b) displays variation of dielectric constant  $\epsilon$  peak in an application of  $H$ . The peak related to the FE transition from a collinear spin state to a TC state is being suppressed as temperature is increased. In addition,  $\epsilon$  at a low field region starts to split above 310 K where the PE state is stabilized.

### 3.2.6 Observation of converse ME effect

The control of magnetization under electric field, so-called converse ME effect,



### 3.2. Experimental results

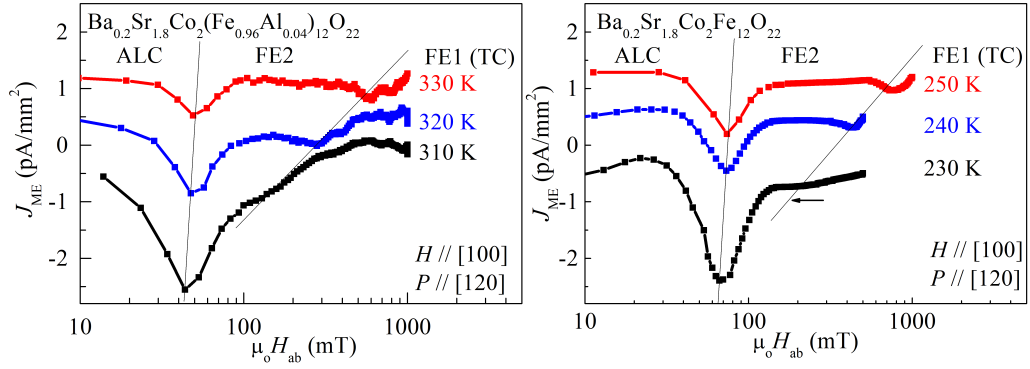


Figure 3.17: ME current at low magnetic field region in (left)  $y = 0.04$  and (right)  $y = 0.00$  compounds.

was also investigated in  $\text{Ba}_{0.2}\text{Sr}_{1.8}\text{Co}_2(\text{Fe}_{0.96}\text{Al}_{0.04})_{12}\text{O}_{22}$  single crystal. Before starting the measurement, the poling process was performed by following the

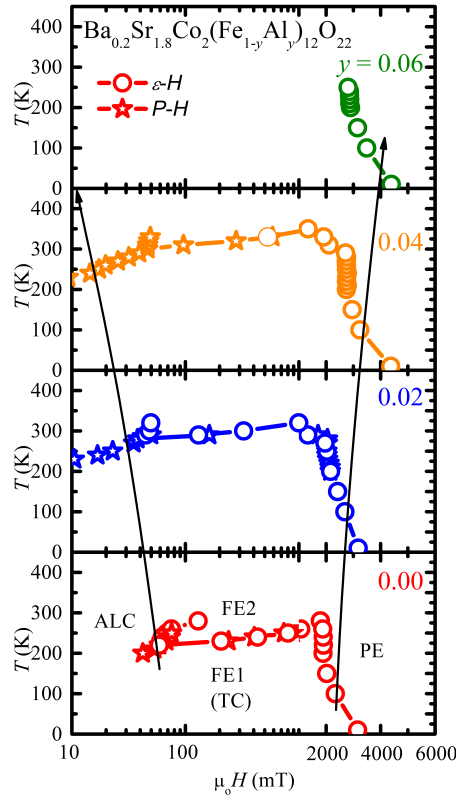


Figure 3.18: Phase diagram of  $\text{Ba}_{0.2}\text{Sr}_{1.8}\text{Co}_2(\text{Fe}_{1-y}\text{Al}_y)_{12}\text{O}_{22}$  single crystal.

previous section. The chiral magnetic domain structures, corresponding to TC and ALC was confirmed in  $\text{CoZn-Y}$  type hexaferrite  $\text{Ba}_{1.3}\text{Sr}_{0.7}\text{CoZnFe}_{11}\text{Al}_1\text{O}_{22}$  [62, 63] and the magnetic domain can be controlled by the electric field due to cross-coupling of ferroelectricity and magnetism [36, 64]. To confirm the converse ME effect in our single crystal, magnetization has been measured with a lab-made VSM probe to apply the electric field to  $\text{Ba}_{0.2}\text{Sr}_{1.8}\text{Co}_2(\text{Fe}_{1-y}\text{Al}_y)_{12}\text{O}_{22}$  samples.

Fig. 3.19 is an example of the converse ME effect at zero magnetic field and 10 K in  $\text{Ba}_{0.2}\text{Sr}_{1.8}\text{Co}_2(\text{Fe}_{0.96}\text{Al}_{0.04})_{12}\text{O}_{22}$ . It shows that magnetization follows the behavior of the electric field. Magnetization increases (decreases) as the electric field increases (decreases), indicating that the variation of magnetization  $\Delta M$  has a linear response to the electric field, while the absolute value  $M$  does not reverse the sign at 10 K. The non-reversal of  $M$  vs  $E$  curve is distinct from the  $\text{Zn}_2\text{Y}$ -type hexaferrite [48]. It is due to the relatively high coercive field  $H_c$  of  $\text{Co}_2\text{Y}$ -type hexaferrites (Note that  $H_c$  of  $\text{Co}_2\text{Y}$ -type hexaferrites is  $\sim 10$  mT whereas  $H_c$  of  $\text{Zn}_2\text{Y}$ -type hexaferrites is  $\sim 1$  mT.). It is likely that the enhancement of magnetic anisotropy along the  $c$ -direction influences the coercivity by pinning the magnetic domain along the direction.

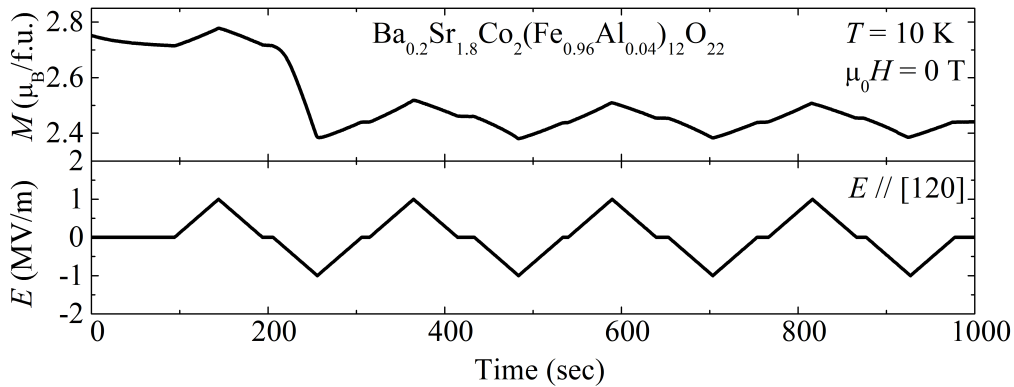


Figure 3.19: Electric field dependence of magnetization at 0 T and 10 K in  $\text{Ba}_{0.2}\text{Sr}_{1.8}\text{Co}_2(\text{Fe}_{0.96}\text{Al}_{0.04})_{12}\text{O}_{22}$ .

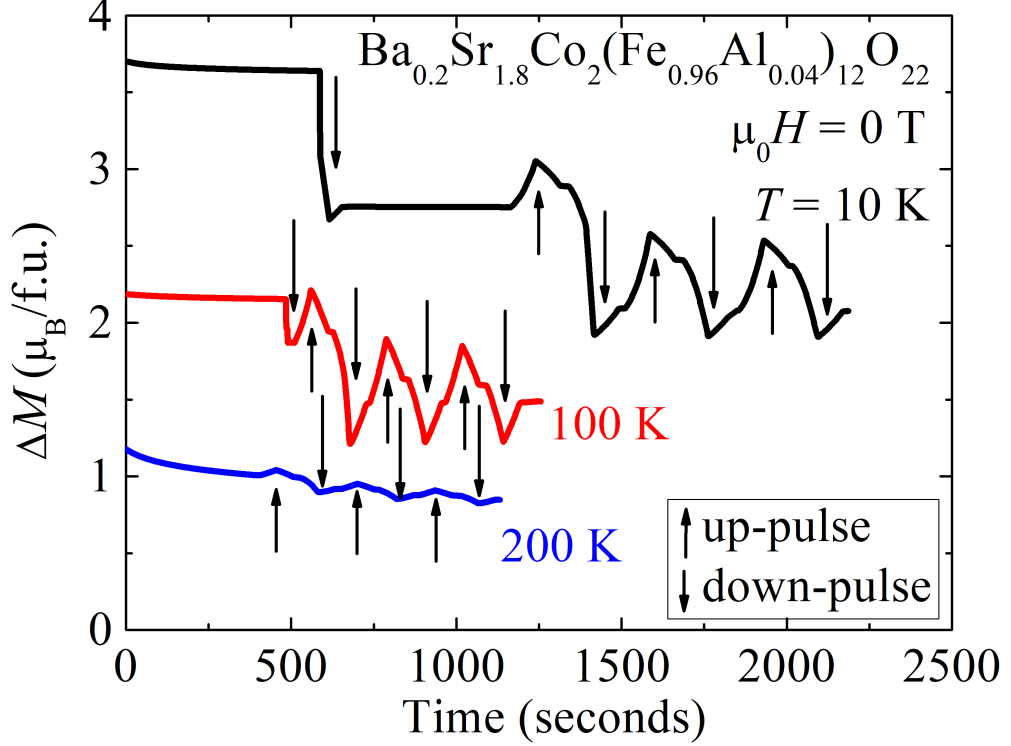


Figure 3.20: Electric field dependence of magnetization at 0 T in various temperatures in  $\text{Ba}_{0.2}\text{Sr}_{1.8}\text{Co}_2(\text{Fe}_{0.96}\text{Al}_{0.04})_{12}\text{O}_{22}$ .

Fig. 3.20 displays the same measurement at various temperature ranges. At 100 K and 200 K, magnetization also shows a linear response to the electric field and the overall  $\Delta M$  variations are suppressed as warming the sample. Furthermore, remnant magnetization at 0 T is  $\sim 1 \mu_B$  at 200 K, even though the modulation of magnetization by the electric field is small ( $\Delta M = \sim 0.05 \mu_B$ ). As a result, the reversal of magnetization is not realized in our experiments. V. Kocsis, *et al.*, [36, 64] claims that magnetization is reversed by the electric field at 0 T, even at 250 K in  $\text{Ba}_{0.8}\text{Sr}_{1.2}\text{Co}_2\text{Fe}_{11.1}\text{Al}_{0.9}\text{O}_{22}$ . They applied the high electric field above 5 MV/m, which is almost four times higher than the electric field we applied. The application of 5 MV/m to our  $\text{Ba}_{0.2}\text{Sr}_{1.8}\text{Co}_2(\text{Fe}_{1-y}\text{Al}_y)_{12}\text{O}_{22}$  single

crystal electrically breaks down the sample due to the high current. It indicates that not only the optimization of ME coupling but also the increase of resistivity by oxygen annealing is crucial for the magnetization reversal. The discrepancy between  $dP/dH$  and  $\mu_0(dM/dE)$  is exhibited in Fig. 3.21 and it has been discussed in previous studies [56,65]. It might be also originated from the insufficient biased-electric field and it seems that cobalt substitution has a relevant role to enhance the coercivity as discussed before.

Eventually, magnetization can be reversed by the aid of finite magnetic field. Fig. 3.22 depicts the result. The reversal of magnetization by the electric field is realized with small magnetic field of -6 mT in  $\text{Ba}_{0.2}\text{Sr}_{1.8}\text{Co}_2(\text{Fe}_{0.96}\text{Al}_{0.04})_{12}\text{O}_{22}$ . The remnant magnetization  $M_r$  - 0.07  $\mu_B/\text{f.u.}$  at -6 mT is successfully modulated

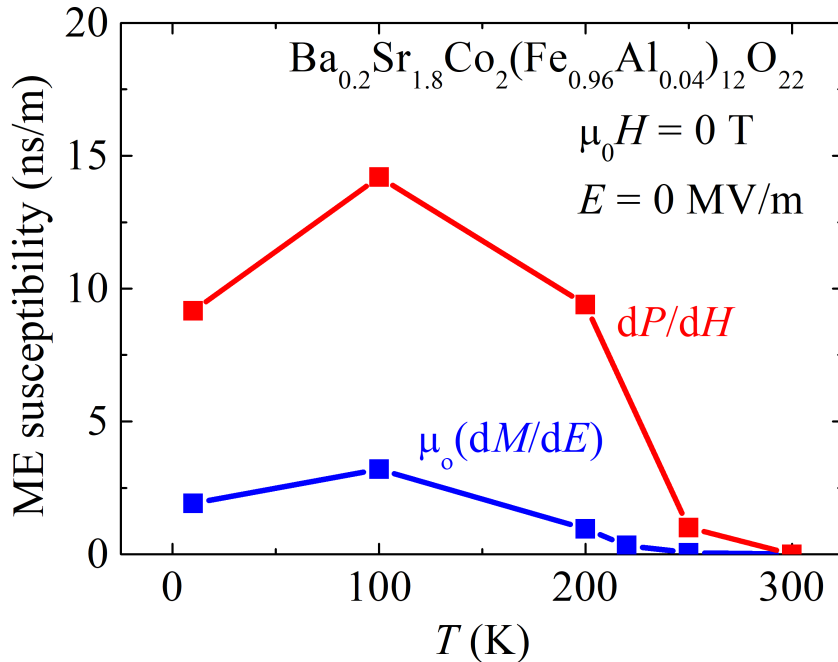


Figure 3.21: Electric field dependence of magnetization at 0 T in various temperatures in  $\text{Ba}_{0.2}\text{Sr}_{1.8}\text{Co}_2(\text{Fe}_{0.96}\text{Al}_{0.04})_{12}\text{O}_{22}$ .

$\pm 0.3$  by application of the electric field  $\pm 3$  MV/m.

Fig. 3.23 summarize the  $\Delta M$  vs  $E$  curves in  $\text{Ba}_{0.2}\text{Sr}_{1.8}\text{Co}_2(\text{Fe}_{1-y}\text{Al}_y)_{12}\text{O}_{22}$ . We found that  $y = 0.04$  compound has the highest converse ME coupling from 10 K to 300 K. The linear behavior of magnetization changes to a quadratic curve at room temperature because the linear coefficient of ME susceptibility is decreasing near room temperature [47]. The overall coercive electric field in  $M$  vs  $E$  curve is around 1 MV/m at 10 K, which is higher than that of  $\text{Zn}_2\text{Y}$ -type hexaferrite (0.1 MV/m) and consistent with the coercive magnetic field in  $M$  vs  $H$ , as mentioned in the previous part.

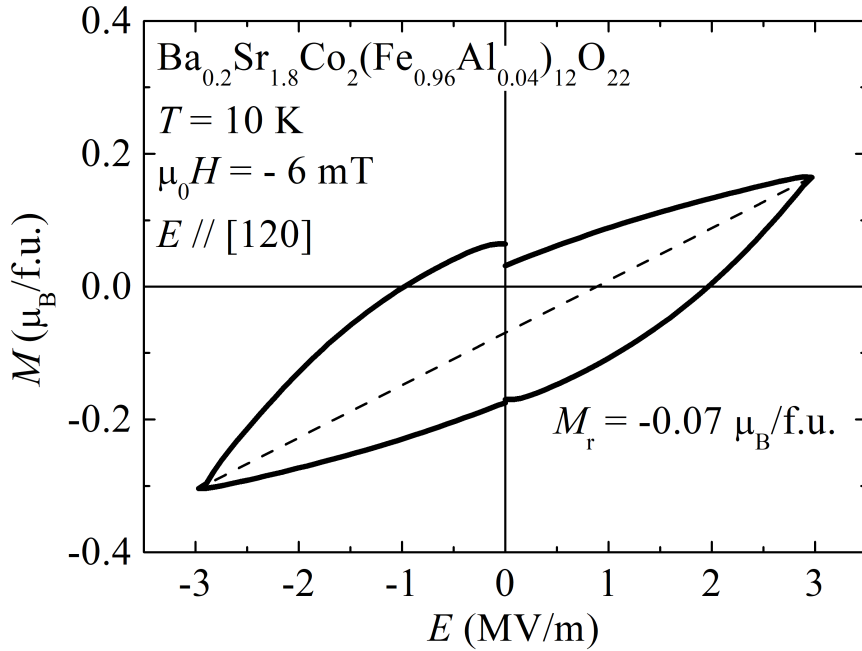


Figure 3.22: The reversal of magnetization by the electric field with finite magnetic field -6 mT in  $\text{Ba}_{0.2}\text{Sr}_{1.8}\text{Co}_2(\text{Fe}_{0.96}\text{Al}_{0.04})_{12}\text{O}_{22}$ .

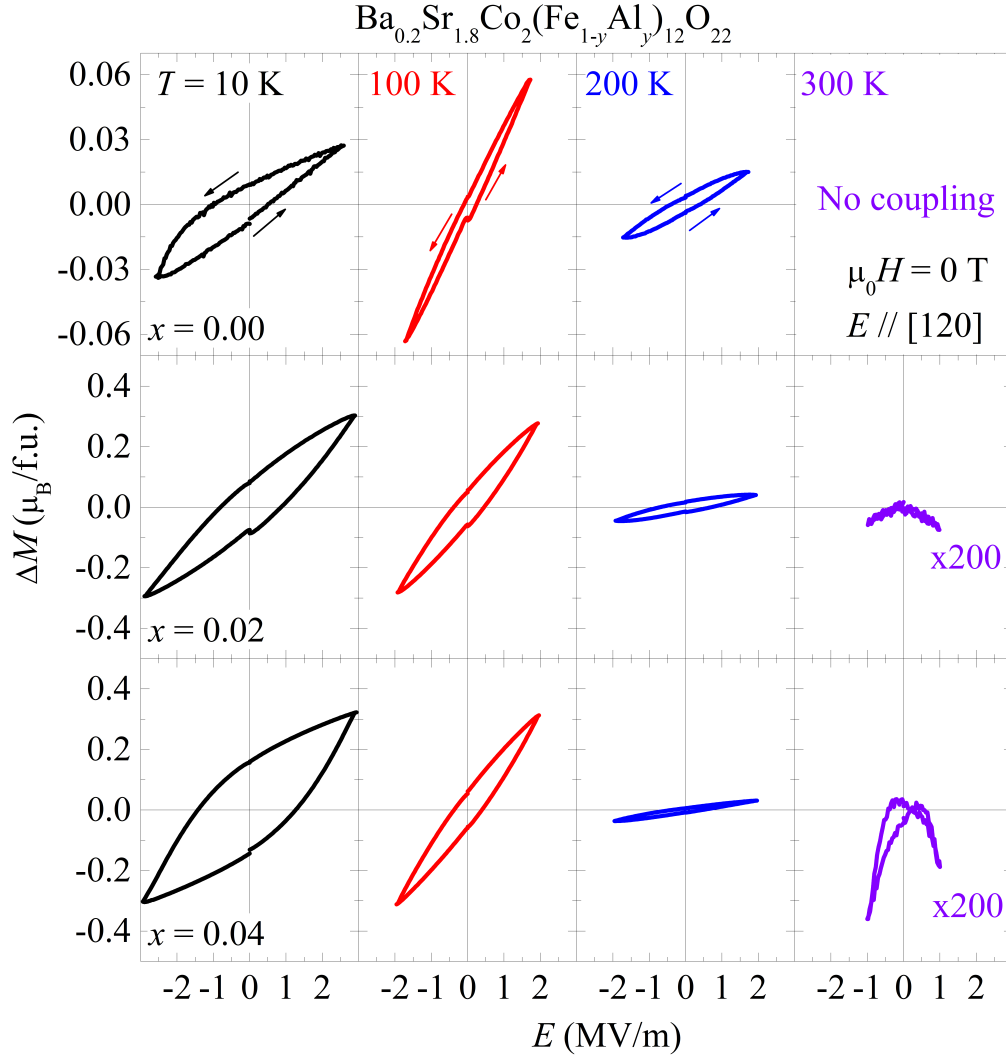


Figure 3.23: The profiles of  $\Delta M$  vs  $E$  in  $\text{Ba}_{0.2}\text{Sr}_{1.8}\text{Co}_2(\text{Fe}_{1-y}\text{Al}_y)_{12}\text{O}_{22}$ .

### 3.3 Discussion

The well-known ALC phase is indeed formed below the temperature regions

where these *ab*-FiM1 or *c*-FiM1 phases are stabilized. When the ALC phase is formed, both  $M_{ab}$  and  $M_c$  decrease to make the moment values become smaller at the ALC phase. The transition temperature for the ALC phase is consistent with the previous neutron diffraction study for the  $y = 0.0$  specimen<sup>16</sup> and the existence of the ALC phase was also confirmed for  $y=0.04$  at 350 K (Fig. 3.11). When the transition temperatures of the ALC phase,  $T_{ALC}$ , is extracted from the extrema of the temperature derivative of the magnetization curves, we find that  $T_{ALC}$ , as indicated by green solid lines in Fig. ??, becomes the highest at  $\sim 440$  K at the Al doping ratio  $y = 0.04$ . As summarized in phase diagram of Fig. 3.14 (green solid circles), the evolution of  $T_{ALC}$  thus forms a dome-shape with an optimal  $T_{ALC} = \sim 440$  K at  $y = 0.04$ . This finding clearly proves that  $T_{ALC}$  becomes highest around the doping ratio of the  $y = 0.04$  specimen.

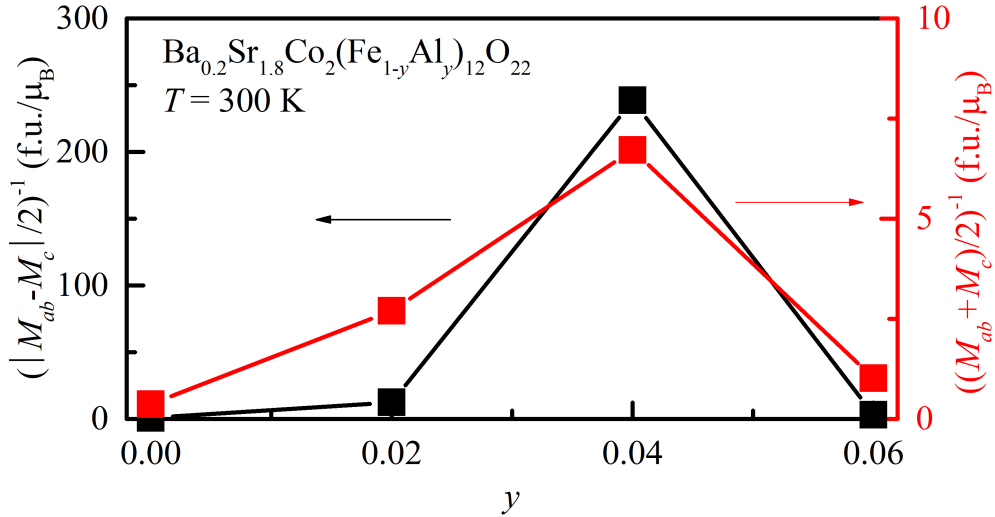


Figure 3.24: The reciprocal of  $|M_{ab} - M_c|/2$  (left tick label) and  $(M_{ab} + M_c)/2$  (right tick label) as a function of Al substitution  $y$  at 300 K. The reciprocal is taken to each values to emphasize the lowest values in the  $y = 0.04$  specimen.

Not only the transition temperature but also the volume fraction of the ALC phase in competition with the  $ab$ -FiM1 or  $c$ -FiM1 phases seems to be most optimized at  $y = 0.04$ . At 300 K where the ALC phase is formed in all the specimens with  $y$  variation, we notice that  $M_{ab}$  and  $M_c$  curves show two interesting features; the overall magnitudes of  $M_{ab}$  and  $M_c$  as well as the difference between  $M_{ab}$  and  $M_c$  also becomes minimum at  $y = 0.04$ . The inverse of  $(M_{ab} + M_c)/2$  and  $|M_{ab} - M_c|/2$ , plotted in Fig. 3.24 demonstrate this trend. Because the ALC phase with a noncollinear antiferromagnetic spin arrangement, is characterized by the isotropic and low magnetic moments, the behavior uncovered in Fig. 3.24 directly shows that the ferrimagnetic phases of  $ab$ -FiM1 and  $c$ -FiM1 formed at higher temperature competes with the ALC phase and as a result, the volume fraction of the ALC phase becomes highest in the  $y = 0.04$  specimen.

Our experimental findings here directly shows that at a proximate zero magnetic field ( $\mu_0 H_M = 20$  mT), the ALC phase becomes the most stabilized at the  $y = 0.04$ . Combining with the magnetization evolution at temperatures below 300 K presented in Fig. 3.8 and 3.9, the observation in the phase diagram of Fig. 3.13 demonstrates that the most stable doping of  $y = 0.04$  for the ALC phase, formed at ZFC, indeed coincides with the most stable TC phase, formed after FC. Therefore, our work here clearly demonstrates that the stability of ALC phase is a prerequisite for making the metastable TC phase after high field applications become most stable to result in a highest volume fraction and a widest temperature window up to high temperature regions. In other words, the highest  $\Delta E_{\text{barrier}}$  between the TC and the ALC phases in Fig. 3.9 is achieved when ALC phase becomes highest.

The importance of the metastability of the TC phase for having the optimized ME coupling at overall temperatures including room temperature is found and



has been also discussed in very recent publications [45, 64]. However, our work here uncovers that  $y = 0.04$  compound exhibits the most stable TC phase with the highest ME coupling in the series of  $\text{Ba}_{0.2}\text{Sr}_{1.8}\text{Co}_2(\text{Fe}_{1-y}\text{Al}_y)_{12}\text{O}_{22}$  specimen. Moreover, the results here establish that the stability of the ALC phase is a key to reaching the optimized TC phase and thus optimized ME coupling. Furthermore, we uncover that the fine control of magnetic anisotropy via selective chemical substitution, e.g.  $\text{Al}^{3+}$  in this case, is an essential procedure to make the ALC phase most stable. The fine control of the magnetic anisotropy seems to also allow the optimized control of spin frustration at the interface as well to result in the most high transition temperatures of the ALC phase.

### 3.4 Conclusion

We have synthesized the Ba<sub>2-x</sub>Sr<sub>x</sub>Co<sub>2</sub>(Fe<sub>1-y</sub>Al<sub>y</sub>)<sub>12</sub>O<sub>22</sub> ( $1.0 \leq x \leq 1.9$  and  $0.00 \leq y \leq 0.08$ ) single crystals in order to maximize the ME coupling by controlling the spin frustration and the magnetic anisotropy. Systematic measurement of ME current reveals that Ba<sub>0.2</sub>Sr<sub>1.8</sub>Co<sub>2</sub>(Fe<sub>0.96</sub>Al<sub>0.04</sub>)<sub>12</sub>O<sub>22</sub> exhibits the biggest magnetic field-induced polarization and dP/dH value among the series of Co<sub>2</sub>Y-type hexaferrites. The magnetization measurement after the various ZFC and FC conditions indicates that metastable TC and ALC phases are coexisting in the all Ba<sub>0.2</sub>Sr<sub>1.8</sub>Co<sub>2</sub>(Fe<sub>1-y</sub>Al<sub>y</sub>)<sub>12</sub>O<sub>22</sub> series, conjectured that the TC phase is separated from the ALC phase by the free energy barrier at low temperature. The magnitude of M<sub>ab</sub> after FC and neutron scattering results support that the free energy barrier develops by Al substitution and the TC phase is the most stabilized in Ba<sub>0.2</sub>Sr<sub>1.8</sub>Co<sub>2</sub>(Fe<sub>0.96</sub>Al<sub>0.04</sub>)<sub>12</sub>O<sub>22</sub> showing the optimized ME coupling. Furthermore, the comparison between M<sub>ab</sub> and M<sub>c</sub> across the ferromagnetic transition demonstrates that Co and Al substitutions modulate the magnetic anisotropy and the transition temperature of ALC phase enhances while *ab*-FiM1 and *c*-FiM1 are competing. Our observation indicates that the robust ALC phase represented by the isotropic and small magnetization is a key ingredient to the giant ME effect and is realized in the  $y = 0.04$  samples. It proposes a general route to achieve the giant ME coupling in the family of Co<sub>2</sub>Y-type hexaferrites at room temperature and additional studies on the out-plane anisotropy of the Al-doped Co<sub>2</sub>Y-type hexaferrites will help to fully understand the delicate magnetic phases.

# Chapter 4

## 2D van der Waals materials $\text{CuCrP}_2\text{X}_6$ (X=S and Se)

### 4.1 Introduction

Multiferroic and magnetoelectric (ME) materials have been intensively investigated due to their exotic physical phenomenon derived from the nontrivial spin order as well as the potential spintronic devices [1, 2, 5, 75]. However, it had been believed that the realization of multiferroic materials is challenging according to empirical  $d^0$ -ness rule relevant to two distinct origins of magnetism and electricity in single material [76]. Since then, new mechanisms of multiferroicity have been proposed to overcome the restriction and several materials have been discovered for more than a decade [2, 30, 77]. For example, material  $\text{BiFeO}_3$  is the most widely investigated material among single materials [14] and  $\text{Cr}_2\text{O}_3$  has been spotlighted as a ME material at room temperature [46]. Artificial multiferroic materials in which perovskite and spinel are combined such as  $\text{BiFeO}_3$ - $\text{CoFe}_2\text{O}_4$  nanostructure, have been also actively studied [1, 78].

It is rare to find multiferric materials in low dimensional system even though multiferroic and ME researches in low dimensional system can open up a new

route for nanoscale electronic devices. Before investigations for multiferroics, there had been theoretical and experimental effort to find the single ferroic materials such as ferromagnetic (FM) and ferroelectric (FE) compounds in two-dimensional (2D) system. FE along out-plane direction in monolayer has been observed in van der Waals (vdW) compounds, such as  $\text{CrGeTe}_3$  and  $\text{CrI}_3$ , with magneto optical Kerr effect measurement [79,80]. Also, the stable in-plane electric polarization ( $P$ ) been measured in 1-unit cell  $\text{SnTe}$  film [81]. Given the successful observation of FM and FE order in 2D system, lots of vdW materials have been theoretically predicted as a 2D multiferroic [82–84] and recently Y. Lai *et al.*, [85] experimentally have claimed that  $\text{CuCrP}_2\text{S}_6$  compound has multiferroic property at room temperature. They explain that the  $P$  along out-plane is attributed to the noncentrosymmetric position of  $\text{Cu}^{1+}$  ions and FM order is originated from the dominant magnetic interaction between  $\text{Cr}^{3+}$  ions within the layer.

Meanwhile, multiferroic and ME materials commonly involve spatial- and time-broken symmetry [86] and are categorized into two types (type-I and type-II) based on the mechanism. In the case of type-I multiferroics, ferroelectricity has distinct origin from magnetism so that the temperatures of ferroelectric and magnetic phase transition don't match each other. In general, the magnitude of  $P$  in type-I multiferroic is large because it is a proper FE in which structural instability is the main source of  $P$ . However, the ME coupling coefficient,  $\alpha = dP/dH$ , is quite small due to two different origins of magnetic and electric order.  $\text{BiFeO}_3$  is a good example of type-I multiferroics. The displacement of  $\text{Bi}^{3+}$  ions from the centrosymmetric site breaks a space inversion symmetry at 1100 K and results in large  $P \sim 100 \mu\text{C}/\text{cm}^2$  at room temperature, while antiferromagnetic (AFM) ordering originated from partially filled  $d$ -orbital of  $\text{Fe}^{3+}$  ions occurs at 643 K with small  $\alpha = 55 \text{ ps/m}$  [14,87].

In contrast, type-II multiferroic results from the single origin. The exotic spin order such as  $\uparrow\uparrow\downarrow\downarrow$  and cycloidal spin configuration can be realized from the competition between complex magnetic interaction and spin frustration. The special spin texture can give rise to spin-induced polarization by breaking the inversion symmetry and the emergence of  $P$  has been established as three well-known mechanisms: exchange striction [26, 27], spin current model [30, 47, 48], and  $p$ - $d$  hybridization [35, 77, 88]. Therefore, ferroelectricity accompanies magnetism and they are strongly coupled. For example,  $\text{TbMn}_2\text{O}_5$  exhibits  $P$  attributed to exchange striction between the  $\text{Mn}^{4+}$ - $\text{Mn}^{3+}$  spin chain at 37 K and  $\alpha$  is estimated to be 600 ps/m [89]. Among hexaferrites materials, Y-type hexaferrites  $\text{Ba}_{0.5}\text{Sr}_{1.5}\text{Zn}_2(\text{Fe}_{0.92}\text{Al}_{0.08})_{12}\text{O}_{22}$  with spin transverse conical structure which breaks the inversion symmetry by spin current model shows the huge ME coupling with  $\alpha = 20000$  ps/m which is the highest value in the world [48]. Another type of hexaferrites, Z-type hexaferrites  $\text{Ba}_{0.48}\text{Sr}_{2.52}\text{Co}_2\text{Fe}_{24}\text{O}_{41}$  also has the strong ME coupling even at room temperature [24] and the mechanism of huge ME coupling has been revealed to be the spin-direction dependent hybridization between  $d$ -orbital of  $\text{Fe}^{3+}$  ion in the off-centered octahedral site and  $p$ -orbital of oxygen ligand, so-called  $p$ - $d$  hybridization [58].

In the application point of view, developing the type-II multiferroic is necessary as much as type-I multiferroic because type-II multiferroic generally has strong ME coupling. However, to our knowledge, type-II multiferroic or ME coupling have not been found yet in 2D vdW compound. In this work, we present the discovery of type-II multiferroic and its magnetoelectric coupling in  $\text{CuCrP}_2\text{S}_6$  single crystal. In order to find a new type-II multiferroic material in 2D vdW material, we have focused on magnetic  $\text{Cr}^{3+}$  ion because  $\text{Cu}^{1+}$  ion has no spin magnetic moment with  $d^{10}$  electronic configuration. We have observed magnetic

field-induced-polarization accompanying to AFM order at 32 K. With comprehensive measurement of magnetic and dielectric properties, we have successfully drawn enriched phase diagram. We will also discuss about the physical origin of  $P$  based on  $p$ - $d$  hybridization mechanism derived from off-centered  $\text{Cr}^{3+}$  cation by comparing to the counterpart compound  $\text{CuCrP}_2\text{Se}_6$ .

## 4.2 Experimental results

### 4.2.1 The growth of single crystals

$\text{CuCrP}_2\text{S}_6$  Single crystal was successfully grown by chemical vapor transport (CVT) method with sulfur as a self-transport agent. The stoichiometric Cu, Cr, P, and S powder of high purity was mixed as a starting material and sealed in an evacuated quartz tube. The tube was position in well-calibrated tube furnace with a temperature gradient from 650 °C to 600 °C for 2 weeks [40]. In the case of  $\text{CuCrP}_2\text{Se}_6$ , the condition of sample growth is almost similar, except that we have used  $\text{SeCl}_4$  as a transport agent. The single crystals of thin plate shape with the size  $2 \times 2 \times 0.5 \text{ mm}^3$  have grown on the cold zone (Fig. 2(a)). The structural

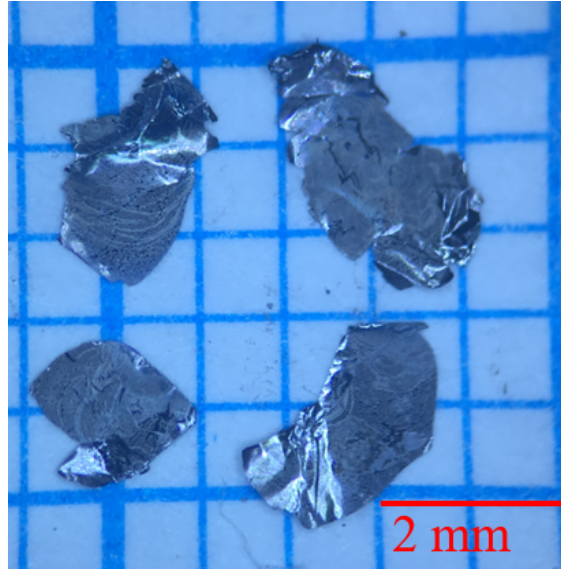


Figure 4.1: The image of the grown  $\text{CuCrP}_2\text{S}_6$  single crystal.

analysis is performed by high-resolution X-ray diffractometer and XRD data has a good agreement on Ref. [90].

### 4.2.2 Crystallographic structure of $\text{CuCrP}_2\text{X}_6$

The structure of  $\text{CuCrP}_2\text{S}_6$  is layered structure. Within the layers,  $\text{Cu}^{1+}$ ,  $\text{Cr}^{3+}$  ions, and P-P pairs constitute the honeycomb lattice in an ordered way as depicted to Fig. 4.3 (b). The honeycomb layers are separated by a vdW gap. Out of three ions,  $\text{Cr}^{3+}$  is the only source of long range magnetic ordering because  $\text{Cu}^{1+}$  does not have spin moment due to  $d^{10}$  electronic configuration [40]. Below 150 K,  $\text{CuCrP}_2\text{S}_6$  undergoes structural transition to  $Pc$  space group at 150 K. Fig. 4.3 (a)

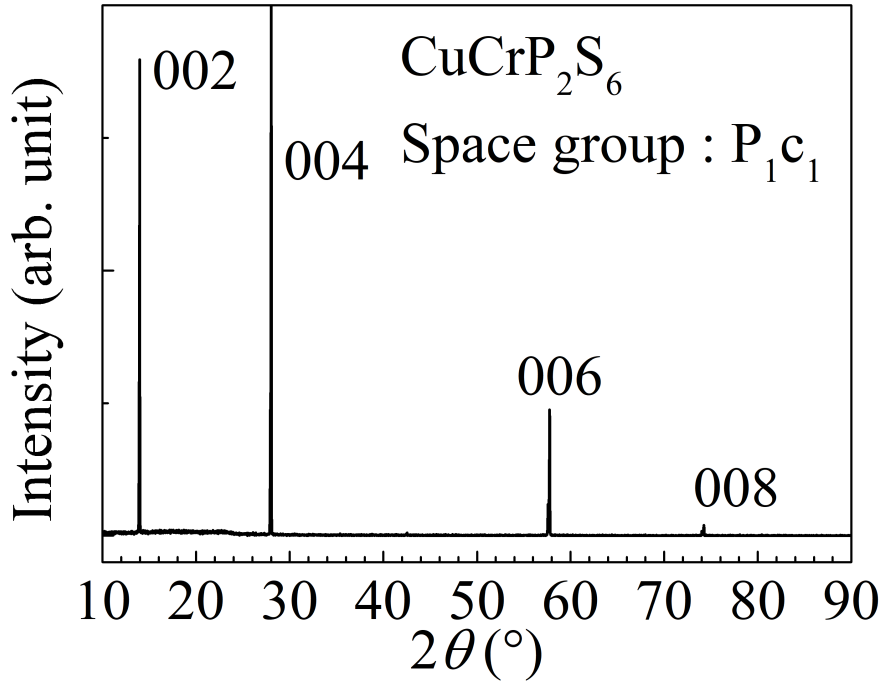


Figure 4.2: XRD peak of  $\text{CuCrP}_2\text{S}_6$  indexed by the space group suggested in Ref. [90].



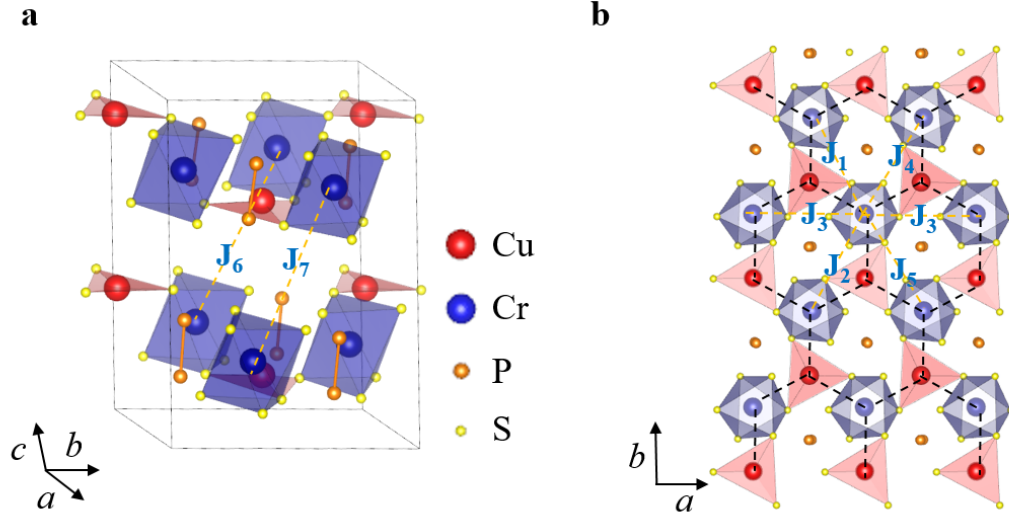


Figure 4.3: (a) The crystal structure of  $\text{CuCrP}_2\text{S}_6$  including the six  $\text{CrS}_6$  octahedron (blue) and the six  $\text{CuS}_3$  triangle (red) below 150 K.  $\text{P}^{4+}$  ions (orange) forms pairs. Orange dashed line indicates the NNN interaction  $J$  (b) The illustration projected onto  $ab$ -plane. It shows the  $\text{CuS}_6$  and  $\text{CrS}_6$  have honeycomb network (dashed line).

displays that Cu atoms alternatively move to up-down position in the octahedral site at 150 K so that Cu atoms mostly form triangular network and it changes to be structurally ordered with antipolar Cu sublattice [90–92, 94]. Moreover, the ordered Cu-Cr honeycomb lattice is distorted leading to the deviation of the Cr position from the center of  $\text{CrS}_6$  octahedron.

In contrast to  $\text{CuCrP}_2\text{S}_6$ ,  $\text{CuCrP}_2\text{Se}_6$ , the counterpart of  $\text{CuCrP}_2\text{S}_6$ , has a disordered Cu atom from the center of octahedral site and the honeycomb lattice is not distorted [93], thus giving rise to almost centered position of Cr atom in the  $\text{CrSe}_6$  octahedron. The structural difference between two compounds is essential to discuss about the origin of ME coupling at the last section. The structures of  $\text{CuCrP}_2\text{X}_6$  are compared in Fig. 4.4. it displays the structures including only Cu and Cr atoms and it is easily found that the lattice structure of  $\text{CuCrP}_2\text{S}_6$  is buckled.

### 4.2.3 Magnetic properties in $\text{CuCrP}_2\text{S}_6$

On further cooling process,  $\text{CuCrP}_2\text{S}_6$  compound shows AFM transition at 32 K. Fig. 2 (a) displays the magnetization  $M$  data as a function of temperature  $T$  along  $a$ -,  $b$ -, and  $c^*$ -direction ( $c^*$ -direction is parallel to  $a \times b$ ). The  $M$ - $T$  data demonstrates the weak magnetic anisotropy with easy axis along  $a$ -direction. Previous results claim that  $\text{CuCrP}_2\text{S}_6$  possibly possess FM order within the layer (in-plane) and AFM order between the layer (out-plane) with easy plane anisotropy [40,91]. Our result which has been obtained by distinguishing between  $a$ - and  $b$ -direction thoroughly indicates that magnetic anisotropy is not easy plane but easy axis. For magnetic field ( $H$ ) along every direction, it shows anomaly at  $T_N = 32$  K, implying the AFM ordering.

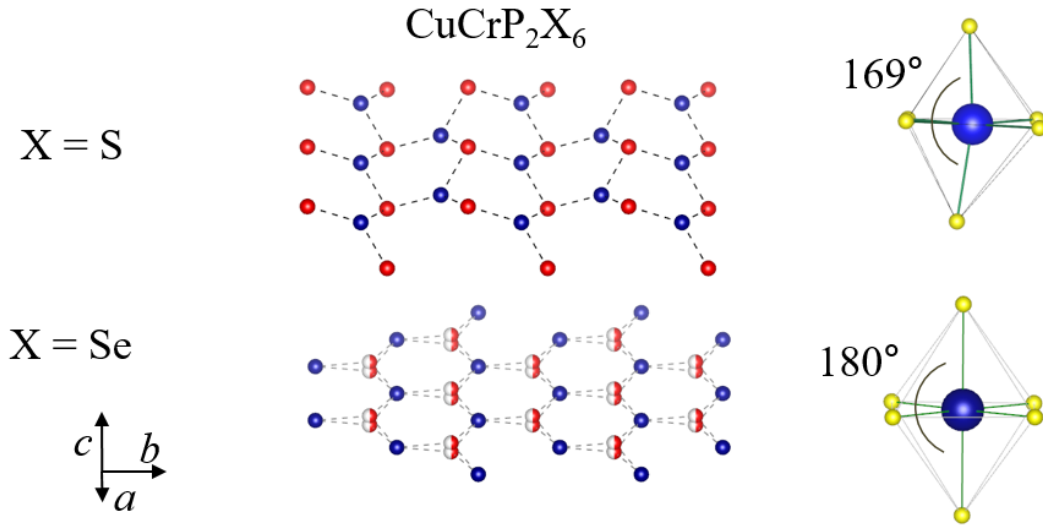


Figure 4.4: The comparison between  $\text{CuCrP}_2\text{S}_6$  and  $\text{CuCrP}_2\text{Se}_6$  structure including only Cu and Cr atoms. The white and red mixed ball indicates the disordered distribution of Cu atom at two different positions. In contrast with  $\text{CuCrP}_2\text{Se}_6$  compound,  $\text{CuCrP}_2\text{S}_6$  has a buckled structure (left). Also  $\text{CrS}_6$  octahedron of  $\text{CuCrP}_2\text{S}_6$  is much distorted than that of  $\text{CuCrP}_2\text{Se}_6$  (right) [93].

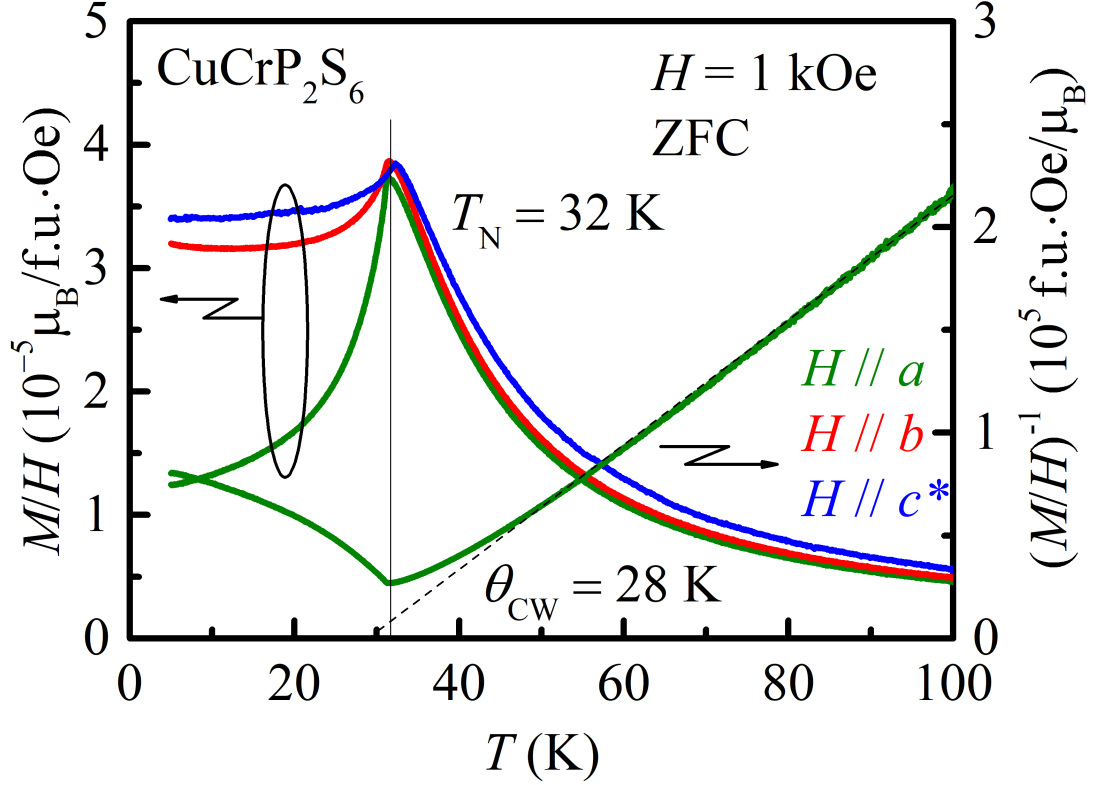


Figure 4.5: The temperature dependent magnetization  $M$  along  $a$ -,  $b$ -, and  $c$ -directions after zero field cooling process (ZFC). The Néel temperature  $T_N$  is 32 K and Curie-Weiss temperature  $\theta_{CW}$  is 28 K.

	$J_1$	$J_2$	$J_3$	$J_4$	$J_5$
Cu-Cu distance (Å)	5.832	5.868	5.935	6.008	6.044
Intralayer coupling (meV)	3.66	2.8	1.9	2.66	1.62
	$J_6$	$J_7$			
Cu-Cu distance, Å	6.674	6.718			
Interlayer coupling (meV)	-0.2	0.096			

Table 4.1: Exchange constant  $J$  of  $\text{CuCrP}_2\text{S}_6$  estimated from the DFT calculation.  $J_1$ - $J_5$  indicates the intralayer exchange constant and  $J_6$ - $J_7$  is interlayer exchange constant as depicted to Fig. 4.6.

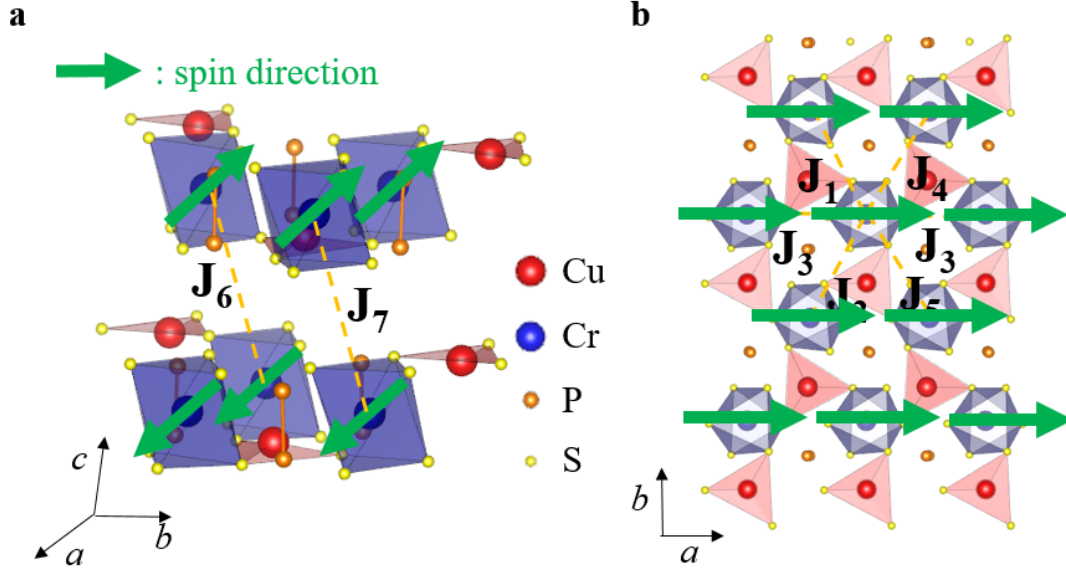


Figure 4.6: (a) Spin structure of  $\text{CuCrP}_2\text{S}_6$  overlapped in the crystal structure displayed in Fig. 4.3. Green arrows indicates the spin direction. (b) The projection onto  $ab$ -plane.

Moreover,  $M$  along  $a$ -direction starts from  $\sim 1 \mu_B/\text{f.u.}$  almost close to zero at lowest temperature, supporting the cancellation of magnetic moment by AFM along  $a$ -direction. The  $1 \mu_B/\text{f.u.}$  discrepancy probably comes from the 1 kOe external field. This result also can be compared to the prediction of density functional theory (DFT) calculation. Table 4.1 summarizes the next nearest neighbor (NNN) exchange interaction ( $J_n$ ) marked in Fig. 4.3. DFT calculation estimates the intralayer coupling to FM and interlayer coupling to AFM, consistent with previous studies [40, 90, 91] and our experimental data. Fig. 4.5 exhibits long range AFM ordering on bulk samples while Curie-Weiss temperature  $\theta_{CW}$  is +28 K, demonstrating that FM interaction is surviving. Thus by putting all information together it is seen that spins mostly aligned along  $a$ -direction forms FM ordering within the  $ab$ -plane and AFM ordering along  $c$ -direction (Fig. 4.6).

Fig. 4.7 depict the  $M$  under  $H$  sweeping along  $a$ -,  $b$ -, and  $c$ -direction at 10 K

with different magnetic field scale. The left and right image plot high magnetic field from -9 T to 9 T and low magnetic field -0.9 T to 0.9 T respectively. The  $M$ - $H$  along  $a$ -direction curve has a slight curvature change at 0.3 T, whereas  $b$ - and  $c^*$ -directional curves show a linear behavior. The curvature change representing the spin-flop (SF) transition only happens along  $a$ -direction [87]. The  $M$  is saturated at 6.1 T (8.3 T) when  $\mu_0 H$  is applied to  $ab$ -plane ( $c^*$ ) and the transition was coined to magnetic field-induced ferromagnetic (FIF) transition. The saturated  $M_s$  is  $2.4 \mu_B/\text{f.u.}$  ( $3.0 \mu_B/\text{f.u.}$ ) for  $H//ab$  ( $H//c^*$ ) configuration, little smaller than isolated  $\text{Cr}^{3+}$  moment  $3.87 \mu_B$ .

#### 4.2.4 Magnetoelectric properties in $\text{CuCrP}_2\text{S}_6$

Fig. 4.8 present the ME current under electric field  $E$ -bias, magnetic field-induced polarization along  $c^*$ -direction  $\Delta P_{c^*}$ , and dielectric constant  $\epsilon$  as a function of  $H$  along  $ab$ -plane at 5 K. We have observed ME current peak in the

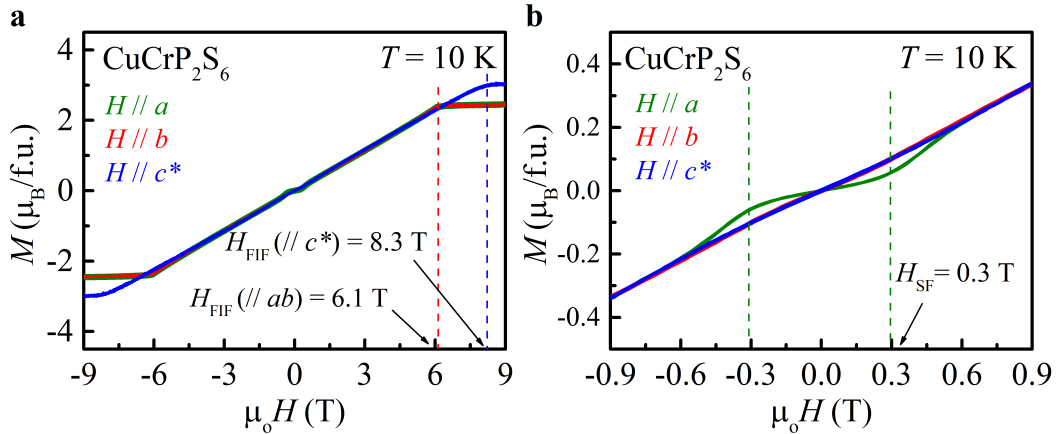


Figure 4.7: (a) Magnetization  $M$  along  $a$ -,  $b$ -, and  $c^*$ - directions as a function of magnetic field with  $-9 \text{ T} \leq \mu_0 H \leq 9 \text{ T}$  (left) and  $-0.9 \text{ T} \leq \mu_0 H \leq 0.9 \text{ T}$  (right) ranges. FIF and SF indicate the magnetic field induced ferromagnetic transition and spin-flop transition, respectively.

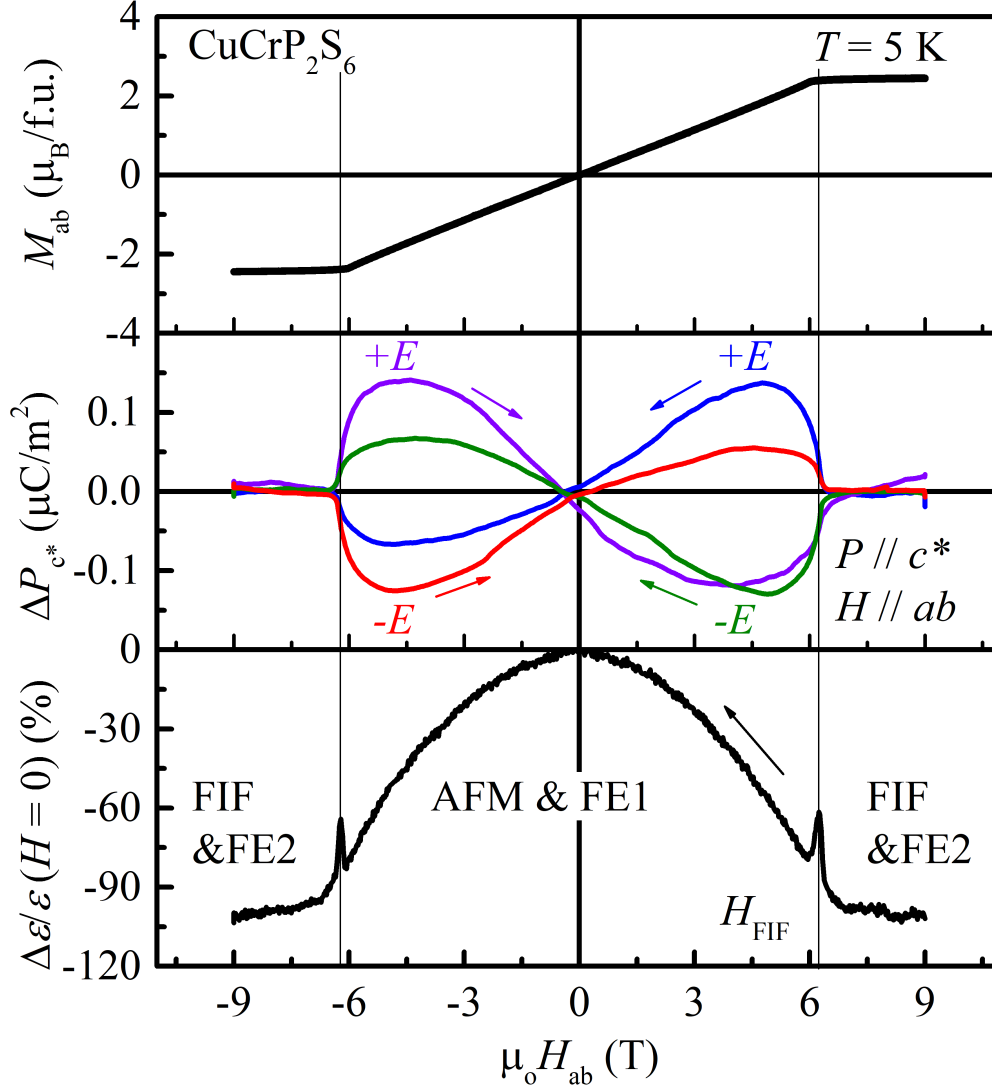


Figure 4.8: (a) Magnetization  $M$  along  $a$ -,  $b$ -, and  $c$ - directions as a function of magnetic field with  $-9 \text{ T} \leq \mu_0 H \leq 9 \text{ T}$  (left) and  $-0.9 \text{ T} \leq \mu_0 H \leq 0.9 \text{ T}$  (right) ranges. FIF and SF indicate the magnetic field induced ferromagnetic transition and spin-flop transition, respectively.

vicinity of  $H_{FIF}$  and broad signal between  $-H_{FIF}$  and  $H_{FIF}$ . The ME current is reversed when the sign of  $E$ -bias is changed. The  $P$  is obviously switched by  $E$ -

bias strongly supporting the emergence of ferroelectricity, termed a FE1 phase.  $\epsilon$ - $H$  curve exhibits a peak feature at  $\mu_0 H_{FIF} = 6.1$  T, accompanying to FE1 transition of ME current. It also indicates that there is the FE transition at 6.1 T for  $H//ab$  configuration. Furthermore, we did not observe  $P$  for  $P//H$  configuration (Fig. 4.9).

We have performed ME current at various temperature from 5 K to 40 K. Fig. 4.10 displays the results at selected temperature. The magnitude of ME current is gradually decreasing and the magnetic field where FIF transition occurs,  $H_{FIF}$ , is reduced. Fig. 4.10(b) summarize the results. The both of  $\Delta P_{c^*}$  and  $H_{FIF}$  are suppressed with AFM order, implying that the AFM order is strongly coupled to

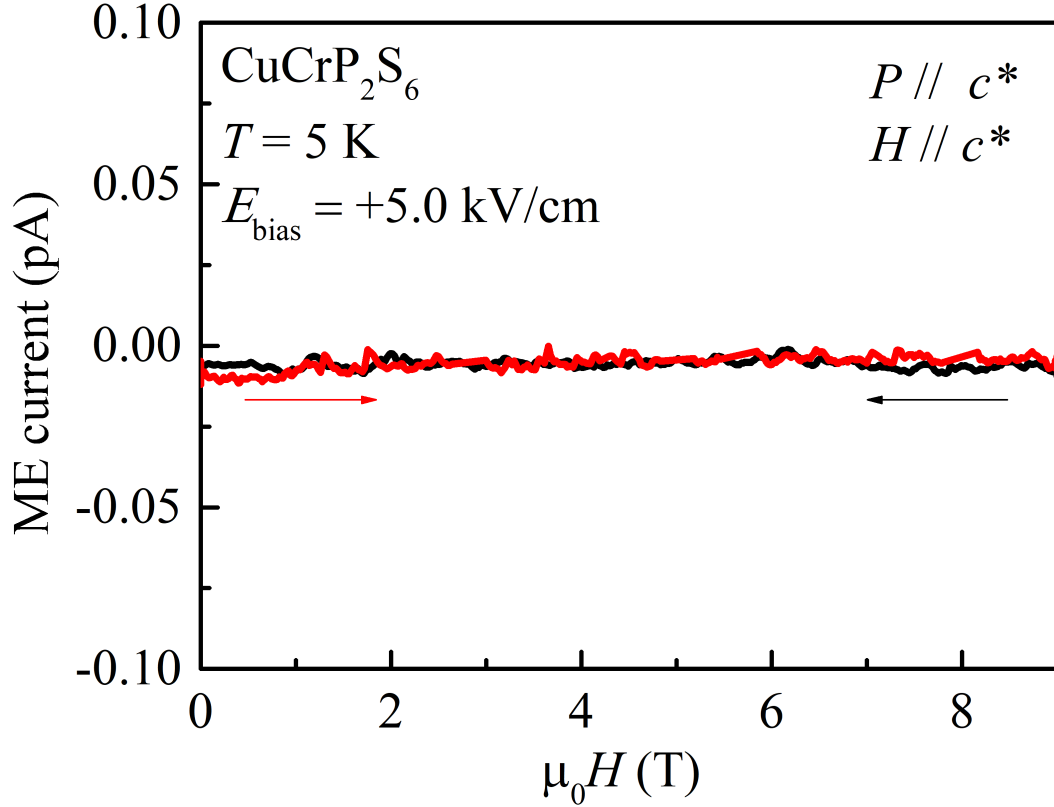


Figure 4.9: ME current measured under  $E$ -bias at 5 K for  $P//c^*$  and  $H//ab$  configuration.

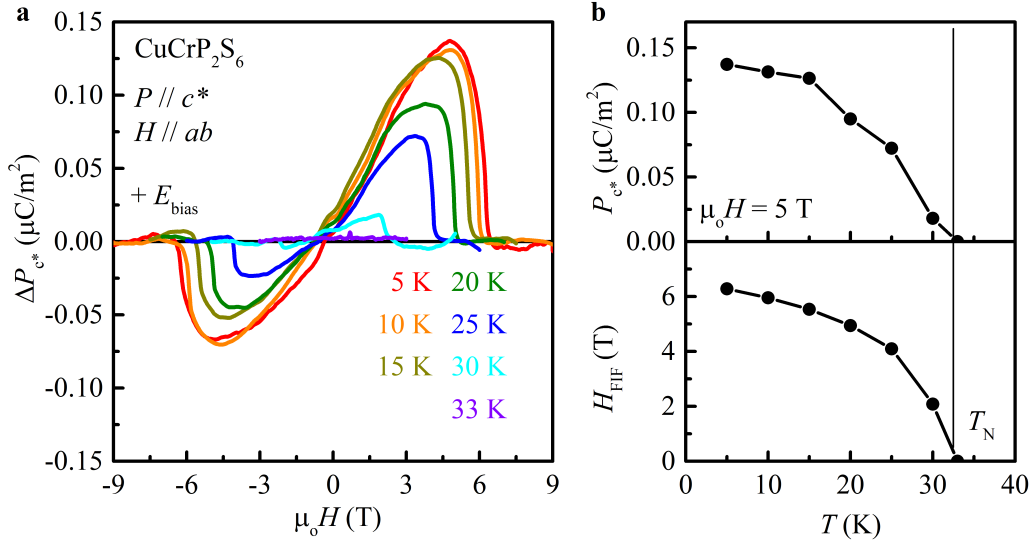


Figure 4.10: (a) Electric polarization as a function of magnetic field at various temperatures. (b) the selected  $\Delta P_{c^*}$  at 5 T and  $H_{\text{FIF}}$  at each temperatures.

FE order.

Based on the comprehensive measurements, we have defined the phase boundary and plotted phase diagram for  $H//ab$ , as presented in Fig. 4.11. As a result, there are three phases. First, paramagnetic (PM) and antiferroelectric (AFE) phase resulting from the antipolar sublattice of  $\text{Cu}^{1+}$  is placed above  $T_N = 32$  K. The phase is well-known phase from the previous studies consistent with our result. Second phase is AFM and FE1 phase in which out-plane ferroelectricity are particularly originated from the spin. The  $P$  along  $c^*$ -direction is disappeared at high magnetic field as spins are aligned to the magnetic field direction and the resulting third phase is FIF and FE2. We expect that ferroelectricity derived from  $\text{Cu}^{1+}$  ion still survives in the region and further investigation is needed for FE2 phase to identify the exact magnetic and electric structure. However, we call the phase FE2 in order to differentiate it from the FE1 phase.



## 4.3 Discussion

### 4.3.1 The mechanism of ME coupling in $\text{CuCrP}_2\text{S}_6$

As mentioned in the previous part related to crystal structure, the distortion of honeycomb network is much relieved in  $\text{CuCrP}_2\text{S}_6$  than  $\text{CuCrP}_2\text{Se}_6$ . In particular, the  $\text{CrS}_6$  octahedrons consisting of  $\text{CuCrP}_2\text{S}_6$  are also twisted so that Cr atoms are pushed from the center of octahedral  $\text{CrS}_6$ , whereas  $\text{CuCrP}_2\text{Se}_6$  has centered Cr position into octahedral  $\text{CrSe}_6$ . To confirm what the structural difference affects to ME coupling in this system, we have grown  $\text{CuCrP}_2\text{S}_6$  single crystal, as a counterpart compound of  $\text{CuCrP}_2\text{Se}_6$ , and conducted the coherent measurements.

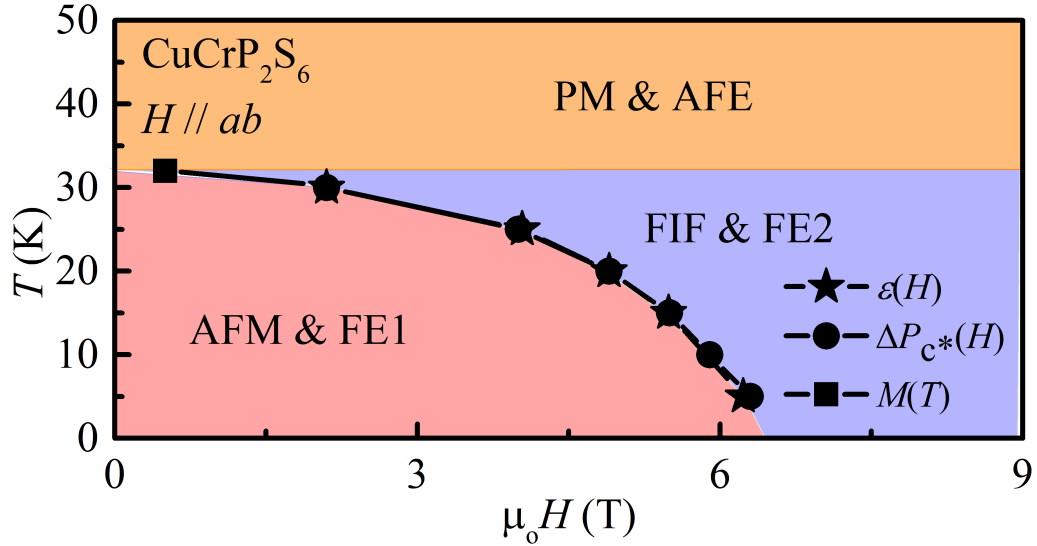


Figure 4.11: Magnetic and electric phase diagram of  $\text{CuCrP}_2\text{S}_6$  for  $H // ab$ . The boundary points are obtained from the dielectric constant  $\epsilon$ , electric polarization  $\Delta P_{c^*}$ , and magnetization  $M$ .

Magnetic properties are shown in Fig. 4.12. Magnetic properties of  $\text{CuCrP}_2\text{Se}_6$  seem to be similar with that of  $\text{CuCrP}_2\text{S}_6$ . Fig. 4.12 verifies that  $\text{CuCrP}_2\text{Se}_6$  undergoes AFM transition at 42 K and FIF transition at 5.5 T at 5 K, similar behavior with  $\text{CuCrP}_2\text{S}_6$ . In spite of the similar magnetic behavior, the magnetic field-induced polarization vanishes in  $\text{CuCrP}_2\text{Se}_6$  (Fig. 4.13), revealing that off-centered  $\text{Cr}^{3+}$  cation plays the crucial role in the ME coupling.

In the introduction 1.2, the microscopic origin of ME coupling in quantum-level is divided into three types: exchange striction [5, 25, 26], spin current model [30, 47, 48], and  $p$ - $d$  hybridization [34, 35, 77, 88]. In the exchange striction mechanism,  $P$  generated from the symmetric exchange interaction between the neighboring magnetic ions, expressed by Eq. 1.1. Also, the Eq. 1.1 indicates that the macroscopic  $P$  is cancelled out when spins form FM ordering aligned to the one direction due to the identical value of  $\langle S_i \cdot S_j \rangle$ . In  $\text{CuCrP}_2\text{S}_6$ , the spins of  $\text{Cr}^{3+}$  ions show FM ordering within the  $ab$ -plane and AFM ordering along  $c$ -direction with the small ratio of FM intralayer coupling to AFM interlayer exchange cou-

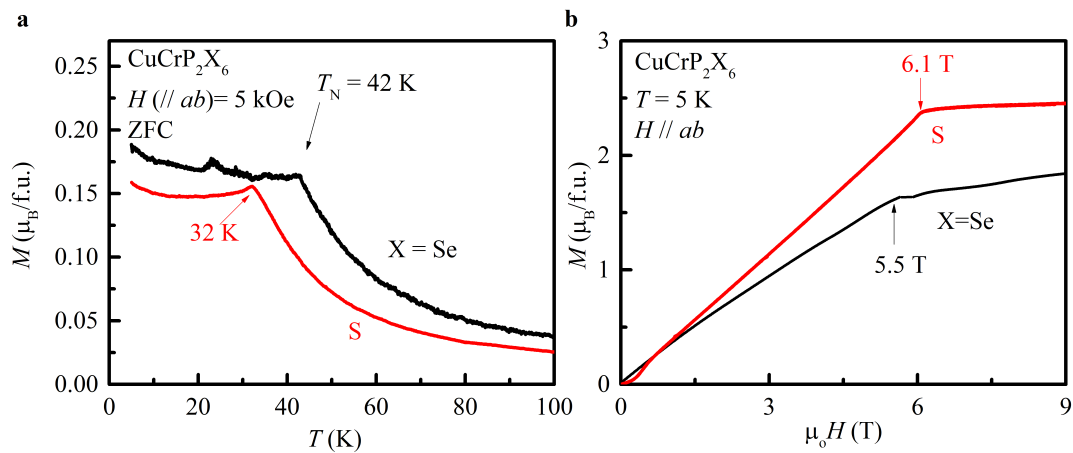


Figure 4.12: (a) Temperature dependent magnetization curve under  $H = 5 \text{ kOe}$  along  $ab$ -plane (b) magnetic field dependent magnetization curve under along  $ab$ -plane at 5 K.

pling,  $0.03 \leq J_{inter}/J_{intra} \leq 0.12$  (Table 4.1). Therefore, the bulk  $\text{CuCrP}_2\text{S}_6$  can be regarded to have a quasi-2D nature and FM spin pairs laying on the layer do not produce the  $P$  with the exchange striction mechanism.

The spin current model or inverse Dzyaloshinskii-Moriya mechanism [30] arising from the antisymmetric spin exchange interaction is formulated by Eq. 1.2. The spin current model is only applicable to canted spin magnet such as cycloidal and transverse conical spin structure. However,  $\text{CuCrP}_2\text{S}_6$  has a small frustration parameter  $f = \theta_{CW}/T_N$  of  $\sim 0.875$ , compared with other materials showing cycloidal ordering ( $\text{Ni}_3\text{V}_2\text{O}_8 \sim 4$  [31],  $\text{MnWO}_4 \sim 6$  [95]). The weak spin frustration support that the spin structure of  $\text{CuCrP}_2\text{S}_6$  is collinear AFM spin structure and previous studies on neutron scattering have no evidence of canted spin structure [40, 91, 94] leading to rule out the spin current mechanism.

The only promising mechanism of ME coupling is  $p$ - $d$  hybridization. In the  $p$ - $d$  hybridization mechanism, local  $P$  is generated from electronic bonding between

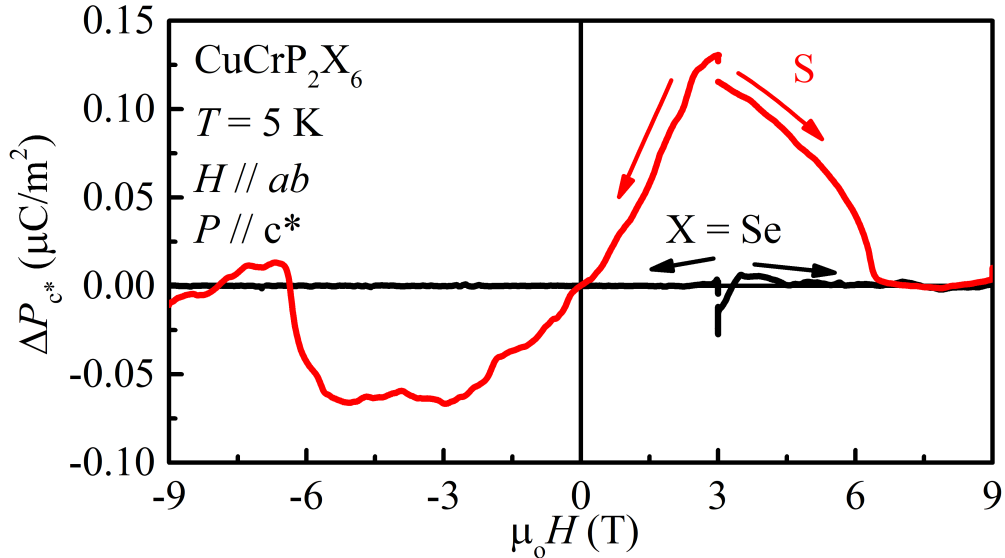


Figure 4.13: Electric polarization of  $\text{CuCrP}_2\text{S}_6$  (red line) and  $\text{CuCrP}_2\text{Se}_6$  (black line) along  $c$ -direction at 5 K for  $H // ab$ .

$p$ -orbital of a ligand ion and  $d$ -orbital of a transition metal magnetic ion. The electronic hybridization depends on spin direction of magnetic ion by spin-orbit coupling and the electric polarization is formulated by Eq. 1.3

The transition metal magnetic ion deviated from the center of octahedron composed of six ligand ions produces the local  $P$  by means of the  $p$ - $d$  hybridization mechanism as well [58]. The  $P$  in the centered magnetic ion is disappeared because the symmetric six hybridizations are cancelled each other. However, the off-centered position breaks the balance of hybridization inside octahedral network and gives rise to local  $P$ . Our result in Fig. 4.13 demonstrates that  $P$  of  $\text{CuCrP}_2\text{S}_6$  containing the off-centered  $\text{Cr}^{3+}$  position is interestingly suppressed in  $\text{CuCrP}_2\text{Se}_6$  without off-centered  $\text{Cr}^{3+}$  position as described in Fig. 4.4. Field-rotation measurement provides another evidence of  $p$ - $d$  hybridization. The mechanism and Eq. 1.3 permit the  $P$  to rotate twice as much to  $H$ -rotation [58]. Fig. 4.14 shows that  $P$  is sinusoidally modulated by the azimuthal angle  $\theta$  of  $H$  with respect to  $a$ -axis and it has  $\pi$  - periodicity. We claim that  $p$ - $d$  hybridization between the off-centered  $\text{Cr}^{3+}$  and  $\text{S}^{2-}$  ligand is probably the origin of ME coupling with two clues: The extinction of  $P$  in  $\text{CuCrP}_2\text{Se}_6$  and sinusoidal behavior of  $P$  under in-plane rotation of  $H$  with period of  $\pi$ . Even though further studies are required to resolve the mechanism of ME coupling, this interpretation will set the stage for understanding the ME coupling in vdW materials.

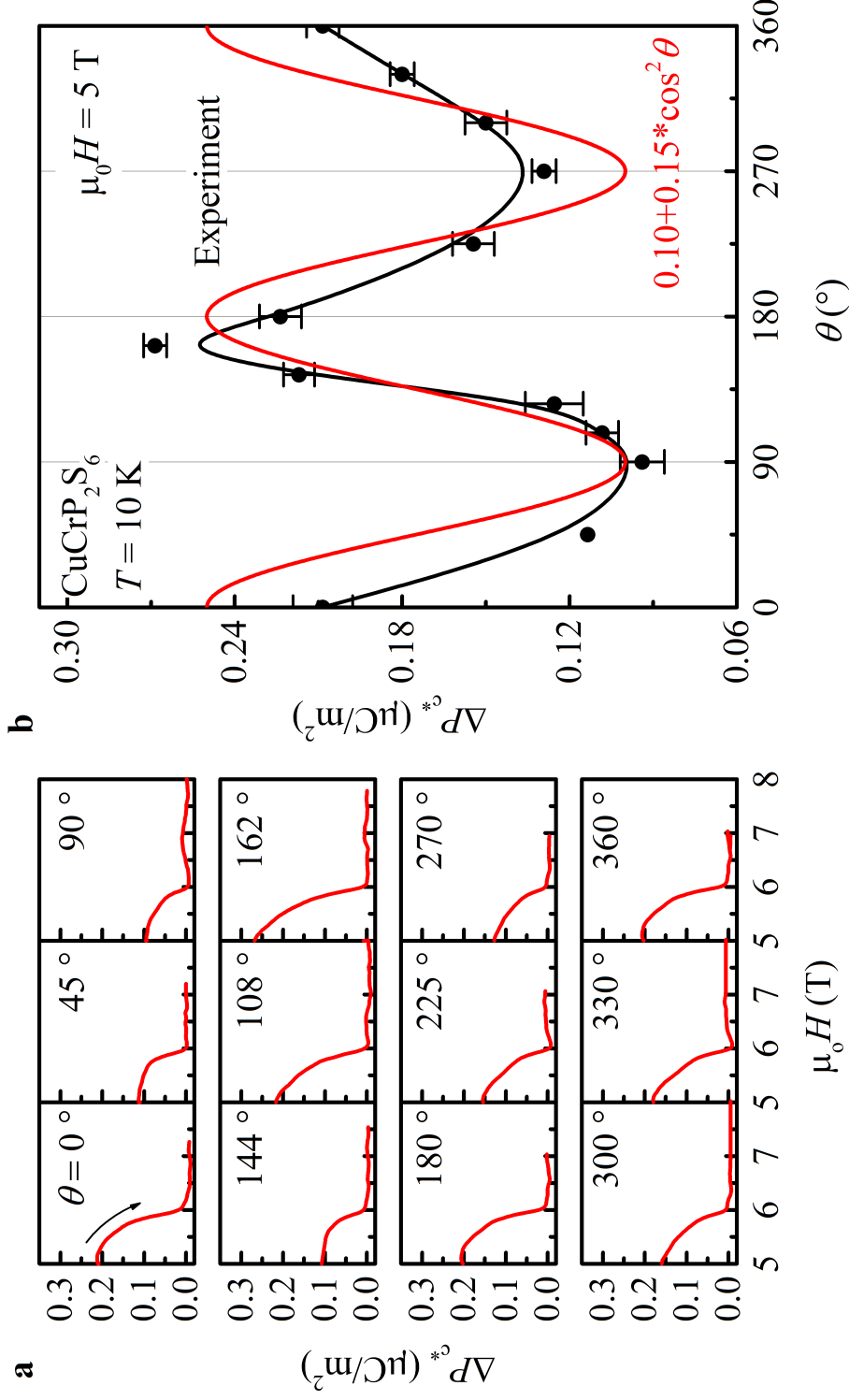


Figure 4.14: (a) Magnetic field dependence of electric polarization at each azimuthal angle  $\theta$   $^\circ \leq \theta \leq 90^\circ$  (first row),  $90^\circ \leq \theta \leq 180^\circ$  (second row),  $180^\circ \leq \theta \leq 270^\circ$  (third row), and  $270^\circ \leq \theta \leq 360^\circ$  (fourth row). (b) The experimental electric polarization  $\Delta P_{c*}$  at 10 K (upper) and calculated electric polarization from  $p$ - $d$  hybridization mechanism (lower) as a function of azimuthal angle  $\theta$ .

### 4.3.2 Symmetry analysis in CuCrP<sub>2</sub>S<sub>6</sub>

Symmetry analysis has been done by Dr. N. T.- Oganessian at Southern Federal University. CuCrP<sub>2</sub>S<sub>6</sub> has a monoclinic  $Pc$  space group with  $a = 5.935$  Å,  $b = 10.282$  Å,  $c = 13.368$  Å, and  $\beta = 106.78^\circ$  [90]. The  $Pc$  space group has two symmetry elements,  $E = (x, y, z)$  and  $\sigma_y = (x, -y, z + \frac{1}{2})$ .  $i^{th}$  Cr atom at  $j^{th}$  layer, Cr <sub>$ij$</sub> , with S <sub>$ij$</sub>  spins are placed at below position (Table 4.2).

Cr <sub><math>ij</math></sub>	Position	S <sub><math>ij</math></sub>
Cr <sub>11</sub>	(0, 0.332, 0.250)	S <sub>11</sub>
Cr <sub>12</sub>	(0, 0.668, 0.750)	S <sub>12</sub>
Cr <sub>21</sub>	(0.527, 0.830, 0.246)	S <sub>21</sub>
Cr <sub>21</sub>	(0.527, 0.170, 0.746)	S <sub>22</sub>

Table 4.2: The distinct atomic positions of Cr atom in one unit cell [90].

Thus, FM and AFM order parameters ( $\vec{F}$  and  $\vec{A}$  respectively) are introduced in this system.

$$\begin{aligned}
 \vec{F}_1 &= \vec{S}_{11} + \vec{S}_{12}; & \vec{F}_2 &= \vec{S}_{21} + \vec{S}_{22} \\
 \vec{A}_1 &= \vec{S}_{11} - \vec{S}_{12}; & \vec{A}_2 &= \vec{S}_{21} - \vec{S}_{22}
 \end{aligned}
 \tag{4.1}$$

Their transformational properties are summarized in Table 4.3. Macroscopically, ME interaction terms which are invariant under  $\sigma_y$  and time reversal ( $T$ ) are only allowed and it gives  $\vec{F} \rightarrow -\vec{F}$  and  $\vec{A} \rightarrow -\vec{A}$ . Therefore,  $P_y F_i^2$  or  $P_y A_j^2$

Irreducible representation	$E(x, y, z)$	$\sigma_y(x, -y, z + \frac{1}{2})$	Order parameter
$\Gamma_1$	1	1	$F_{1y}, F_{2y}, A_{1x}, A_{1z}, A_{2x}, A_{2z}; P_x, P_z$
$\Gamma_2$	1	-1	$F_{1x}, F_{2z}, F_{2x}, F_{2z}, A_{2y}, A_{2y}; P_y$

Table 4.3: Transformational properties of  $Pc$  space group.

are not allowed since they change sign upon  $\sigma_y$ . Also we are interested in the terms such as  $P_i F_j A_k$  among ME interactions formulated by combination of order parameters (Table 4.3) because ME effect exists below  $T_N$  when  $\vec{A} \neq 0$  and  $\vec{F} \neq 0$ . However, we should find any interactions with  $P_z$ ,  $F_x$ ,  $F_y$ ,  $A_x$  and  $A_y$  and invariant ME interactions are as below:

$$P_z F_x A_y, P_z F_y A_x \quad (4.2)$$

Here  $\vec{F}$  can be replace by  $\vec{M}$ . They are not exactly equal, but for the symmetry analysis, it does not matter. As a result, possible terms for electric polarization along  $c$ -direction are as below:

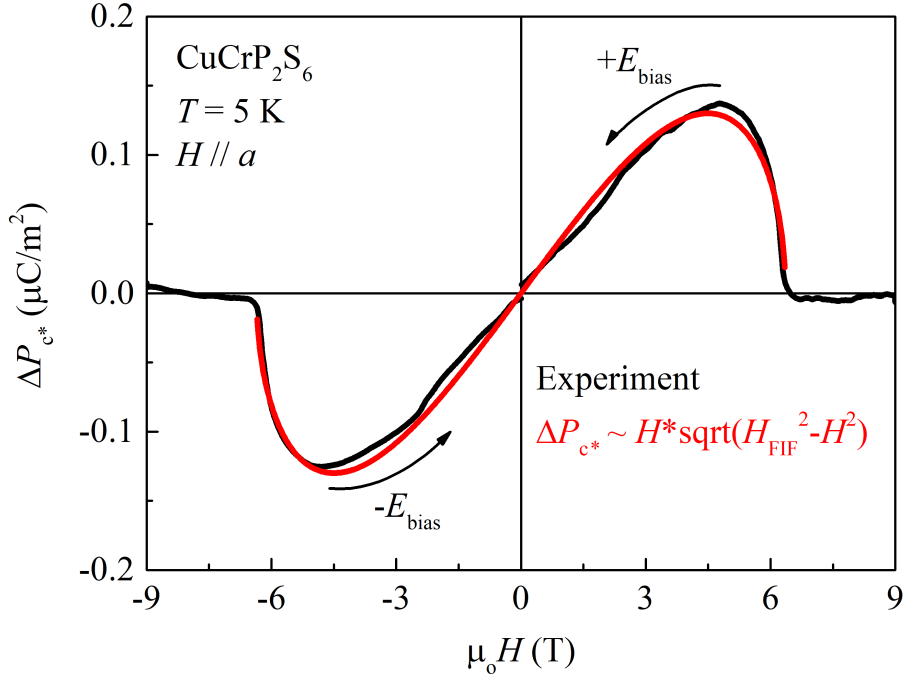


Figure 4.15: Electric polarization by the experiment (black line) and the calculation (red line) in CuCrP<sub>2</sub>S<sub>6</sub>.

$$\begin{aligned} P_z &\sim M_x A_y \\ P_z &\sim M_y A_x \end{aligned} \tag{4.3}$$

Thus, we have

$$P_z = aM_x\sqrt{1 - M_x^2} + bM_y\sqrt{1 - M_y^2} \tag{4.4}$$

where  $a$  and  $b$  are ME coefficient when magnetic field is applied along  $x$  and  $y$  directions. Result is shown in Fig. 4.15 and magnetic field dependent electric polarization curve is quantitatively explained.



## 4.4 Conclusion

In conclusion, we have discovered a new type-II multiferroic material and investigated the ME coupling in vdW compound  $\text{CuCrP}_2\text{S}_6$ . The magnetic measurement and DFT calculation demonstrate that the bulk sample exhibits AFM ordering at 32 K with the weak anisotropy along  $a$ -direction. Concomitant with AFM ordering,  $\text{CuCrP}_2\text{S}_6$  establishes unveiled ferroelectricity strongly coupled to AFM ordering at 32 K. The  $P$  can be controlled by magnetic field and eventually suppressed at high magnetic field as  $M$  is saturated, so-called FIF transition. By comparing with  $\text{CuCrP}_2\text{Se}_6$  having a relaxed structure with almost centered  $\text{CrSe}_6$  octahedron, we claim that the appearance of ME coupling in  $\text{CuCrP}_2\text{S}_6$  compound results from the unbalanced local  $P$  which is induced from the off-centered  $\text{Cr}^{3+}$  cation via  $p$ - $d$  hybridization mechanism. Our observation should shift the paradigm of discovering multiferroicity in 2D vdW materials by utilizing magnetic ion as an ingredient for the ferroelectricity. We also envision that this work will pave the way for realizing the true 2D ME coupling in future.

# Chapter 5

## Summary and conclusion

The magnetoelectric (ME) coupling is highly demanded in many areas of science and technology for fundamental and application purposes, e.g., spintronic devices and next generation memories and sensors. One of central goals for the intense research on multiferroics/magnetoelectrics is an enhancement of the ME coupling at room temperature. In particular, Co<sub>2</sub>Y-type hexaferrites show the biggest polarization reversed by the external magnetic field so that they are known as promising materials to realize the huge ME coupling. There are several routes to optimize the ME coupling in the Co<sub>2</sub>Y-type hexaferrites; for example, a reduction of the leakage current and a delicate control of magnetic structure by doping, etc. In this thesis, we discuss a general route to achieve the giant ME coupling in the family of the Co<sub>2</sub>Y-type hexaferrites by the Aluminum and Strontium substitution. It has been rare that the specific role of Al<sup>3+</sup> is described, even though the magnetic and ME properties are widely studied in these compounds.

As a result, we have optimized the ME coupling in Ba<sub>0.2</sub>Sr<sub>1.8</sub>Co<sub>2</sub>(Fe<sub>0.96</sub>Al<sub>0.04</sub>)<sub>12</sub>O<sub>22</sub> single crystal. We have grown the Ba<sub>2-x</sub>Sr<sub>x</sub>Co<sub>2</sub>(Fe<sub>1-y</sub>Al<sub>y</sub>)<sub>12</sub>O<sub>22</sub> ( $1.0 \leq x \leq 1.8$  and  $0.00 \leq y \leq 0.08$ ) single crystals to control the spin frustration and the magnetic anisotropy. The biggest magnetic field-induced polarization and ME

---

susceptibility is observed in  $\text{Ba}_{0.2}\text{Sr}_{1.8}\text{Co}_2(\text{Fe}_{0.96}\text{Al}_{0.04})_{12}\text{O}_{22}$  out among the series of  $\text{Co}_2\text{Y}$ -type hexaferrites we have synthesized. All  $\text{Ba}_{0.2}\text{Sr}_{1.8}\text{Co}_2(\text{Fe}_{1-y}\text{Al}_y)_{12}\text{O}_{22}$  specimens exhibit the magnetic metastable nature of TC and ALC phases and the variation of the free energy barrier between the magnetic phases, resulting in the well-separated TC phases in  $y = 0.04$  compound. Furthermore, we found that ALC phase is most stabilized up to high temperature by competing the in-plane and out-of-plane magnetic anisotropy. We conclude that the fine tuning of the magnetic anisotropy originated from the Al substitution into the octahedral site is crucial to induce the robust ALC spin phase.

In addition, we report our discovery of magnetic field-induced electric polarization in a two-dimensional (2D) van der Waals material  $\text{CuCrP}_2\text{S}_6$  forming a monoclinic lattice, in which Cu, Cr and P-P pairs are forming a honeycomb networks. We have observed that electric polarization under magnetic fields occurs below 32 K and is modulated by magnetic field while it is suppressed with the spin-flop transition located around 6.1 T. Based on magnetization and electric polarization measurements, electric and magnetic phase diagram has been constructed. We also claim that the magnetic field-induced electric polarization is closely associated with the  $p$ - $d$  hybridization mechanism originated from the off-centered  $\text{Cr}^{3+}$  cations within the octahedral sites. Furthermore, with the symmetry analysis between the antiferromagnetic layers, we could explain the shape of the electric polarization curve qualitatively. The  $p$ - $d$  hybridization mechanism is further corroborated by the observation of vanishing polarization in the  $\text{CuCrP}_2\text{Se}_6$  compound in which  $\text{Cr}^{3+}$  is positioned at the octahedral center, further supporting that the off-centered cation plays an important role in the magnetoelectric coupling. Our results thus point to one general route to induce magnetoelectric coupling in 2D layered materials, *i.e.*, via the off-centered cation.

## Chapter 6

## References

# Bibliography

- [1] R. Ramesh and N. A. Spaldin, [Nat. Mater. \*\*6\*\*, 21–29\(2007\).](#)
- [2] S. -W. Cheong, and M. Mostovoy, [Nat. Mater. \*\*6\*\*, 13 \(2007\).](#)
- [3] D. I. Khomskii, [J. Magn. Magn. Mater. \*\*306\*\*, 1-8 \(2006\).](#)
- [4] Ronald E. Cohen, [Nature \*\*358\*\*, 136–138 \(1992\).](#)
- [5] Y. Tokura, S. Seki, and N. Nagaosa, [Rep. Prog. Phys. \*\*77\*\*, 076501 \(2014\).](#)
- [6] T. Kimura, *et al.*, [J. Phys.: Condens. Matter \*\*20\*\*, 434204 \(2008\).](#)
- [7] T. Kimura, *et al.*, [Nature \*\*426\*\*, 55–58 \(2003\).](#)
- [8] N. Hur, *et al.*, [Nature \*\*429\*\*, 392–395\(2004\)](#)
- [9] C. Lu, *et al.*, [Natl. Sci. Rev. \*\*6\*\*, 653-668 \(2019\).](#)
- [10] D. I. Khomskii, [Physics \*\*2\*\*, 20 \(2009\).](#)
- [11] N. A. Spaldin, S. -W. Cheong, and R. Ramesh, [Physics Today \*\*63\*\*, 10, 38 \(2010\).](#)
- [12] J. Wang, *et al.*, [Science \*\*299\*\*, 1719-1722 \(2003\).](#)
- [13] M. Tokunaga, *et al.*, [Nat. Commun. \*\*6\*\*, 5878 \(2015\).](#)
- [14] M. Tokunaga, *et al.*, [J. Phys. Soc. Jpn. \*\*79\*\*, 064713 \(2010\).](#)

- [15] B. B. V. Aken, *et al.*, [Nat. Mater.](#) **3**, 164 (2004).
- [16] M. Fiebig, *et al.*, [Nature](#) **419**, 818 (2002).
- [17] M. Matsubara, *et al.*, [Science](#) **348**, 1112 (2015).
- [18] T. Arima, *et al.*, [Phys. Rev. Lett.](#) **96**, 097202 (2006).
- [19] Y. S. Oh, *et al.*, [Phys. Rev. B](#) **83**, 060405(R) (2011).
- [20] T. Kimura, G. Lawes, and A. P. Ramirez, *Phys. Rev. Lett.* [Phys. Rev. Lett.](#) **94**, 137201 (2005).
- [21] S. H. Chun, *et al.*, [Phys. Rev. Lett.](#) **104**, 037204 (2010).
- [22] W. -S. Noh, *et al.*, [Phys. Rev. Lett.](#) **114**, 117603 (2015).
- [23] D. Levy, R. Giustetto, and A. Hoser, [Phys. Chem. Miner.](#) **39**, 169 (2012).
- [24] Y. Kitagawa, *et al.*, [Nat. Mater.](#) **9**, 797 (2010).
- [25] J. Wang, *Multiferroic Materials: Properties, Techniques, and Applications*, CRD Press (2016).
- [26] I. A. Sergienko, C. Sen, and E. Dagotto, [Phys. Rev. Lett.](#) **97**, 227204 (2006).
- [27] S. Picozzi, *et al.*, [Phys. Rev. Lett.](#) **99**, 227201 (2007).
- [28] H. Kimura *et al.*, [Phys. Rev. B](#) **87**, 104414 (2013).
- [29] Y. J. Choi, *et al.*, [Phys. Rev. Lett.](#) **100**, 047601 (2008).
- [30] H. Katsura, N. Nagaosa, and A. Balatsky [Phys. Rev. Lett.](#) **95**, 057205 (2005).
- [31] G. Lawes, *et al.*, [Phys. Rev. Lett.](#) **95**, 087205 (2005).

- [32] K. Yoo, *et al.*, [npj Quantum Mater.](#) **3**, 45 (2018).
- [33] T.-h. Arima, [J. Phys. Soc. Jpn.](#) **76**, 073702 (2007).
- [34] H. Murakawa, *et al.*, [Phys. Rev. Lett.](#) **105**, 137202 (2010).
- [35] J. W. Kim, *et al.*, [Nat. Commun.](#) **5**, 4419 (2014).
- [36] V. Kocsis, *et al.*, [Nat. Commun.](#) **10**, 1247 (2019).
- [37] N. Momozawa, M. Mita, and H. Takei, [J. Cryst. Growth](#) **83**, 40 (1987).
- [38] H. S. Shin and S. -J. Kwon, [J. Korean Ceram. Soc.](#) **30**, 499 (1993).
- [39] Y. S. Chai, *et al.*, [New J. Phys.](#) **11**, 073030 (2009).
- [40] P. Colombet, *et al.*, [J. Solid State Chem.](#) **41**, 174 (1982).
- [41] C. De, S. Ghara, and A. Sundaresan, [Solid State Commun.](#) **205**, 61 (2015).
- [42] S. H. Chun, [Ph. D. thesis](#) (2013).
- [43] I. Kagomiya, *et al.*, [Ferroelectrics](#) **286**, 167 (2003).
- [44] D. V. Efremov, J. V. D. Brink, and D. I. Khomskii, [Nat. Mater.](#) **3**, 853 (2004).
- [45] T. Nakajima, *et al.*, [Phys. Rev. B](#) **94**, 195154 (2016).
- [46] A. Iyama and T. Kimura, [Phys. Rev. B](#) **87**, 180408(R) (2013).
- [47] S. H. Chun, *et al.*, [Phys. Rev. Lett.](#) **108**, 177201 (2012).
- [48] Y. S. Chai, *et al.*, [Nat. Commun.](#) **5**, 4208 (2014).

- [49] N. Momozawa, Y. Yamaguchi, and M. Mita, *J. Phys. Soc. Jpn.* **55**, 1350 (1986).
- [50] H. B. Lee, *et al.*, *Phys. Rev. B* **83**, 144425 (2011).
- [51] H. B. Lee, *et al.*, *Phys. Rev. B* **86**, 094435 (2012).
- [52] S. Shen, Y. Chai, and Y. Sun, *Sci. Rep.* **5**, 8254 (2015).
- [53] K. Taniguchi, *et al.*, *Appl. Phys. Express* **1**, 031301 (2008).
- [54] H. Sagayama, *et al.*, *Phys. Rev. B* **80**, 180419(R) (2009).
- [55] F. Wang, *et al.*, *Appl. Phys. Lett.* **100**, 122901 (2012).
- [56] S. Hirose, *et al.*, *Appl. Phys. Lett.* **104**, 022907 (2014).
- [57] S. Shen, *et al.*, *Appl. Phys. Lett.* **104**, 032905 (2014).
- [58] Y. S. Chai, *et al.*, *Phys. Rev. B* **98**, 104416 (2018).
- [59] N. Momozawa and Y. Yamaguchi, *J. Phys. Soc. Jpn.* **62**, 1292 (1993).
- [60] R. C. Pullar, *Prog. Mater. Sci.* **57**, 1191 (2012).
- [61] K. Zhai, *et al.*, *Nat. Commun.* **8**, 519 (2017).
- [62] H. Ueda, *et al.*, *Appl. Phys. Lett.* **109**, 182902 (2016).
- [63] H. Ueda, *et al.*, *Physica B* **536**, 118 (2018).
- [64] V. Kocsis, *et al.*, *Phys. Rev. B* **101**, 075136 (2020).
- [65] B. Choi, *et al.*, *J. Phys.: Condens. Matter* **30**, 065802 (2018).
- [66] S. -P. Shen, *et al.*, *Phys. Rev. B* **95**, 094405 (2017).



- [67] K. Okumura, *et al.*, [Appl. Phys. Lett.](#) **98**, 212504 (2011).
- [68] H. Chang, *et al.*, [Physica B: Condes. Matter](#) **551**, 122 (2017).
- [69] Y. S. Oh, *et al.*, [Nat. Mater.](#) **14**, 407 (2015).
- [70] N. A. Benedek, *et al.*, [Phys. Rev. Lett.](#) **106**, 107204 (2011).
- [71] A. T. Mulder, *et al.*, [Adv. Funct. Mater.](#) **23**, 4810 (2013).
- [72] H.J. Kim, *et al.*, [Bull. Kor. Chem. Soc.](#) **22**, 298 (2001).
- [73] R. Nozaki, *et al.*, [J. Phys. Chem. B](#) **105**, 7950 (2001).
- [74] S.K. Singh, *et al.*, [Mater. Chem. Phys.](#) **160**, 187 (2015).
- [75] T. Zhao, *et al.*, [Nat. Mater.](#) **5**, 823 (2006).
- [76] N. A. Hill, [J. Phys. Chem. B](#) **2000**, 6694 (2000).
- [77] C. Jia, *et al.*, [Phys. Rev. B](#) **74**, 224444 (2006).
- [78] N. A. Spaldin and R. Ramesh, [Nat. Mater.](#) **18**, 203 (2019).
- [79] C. Gong, *et al.*, [Nature](#) **546**, 265 (2017).
- [80] B. Huang, *et al.*, [Nature](#) **546**, 270 (2017).
- [81] K. Chang, *et al.*, [Science](#) **353**, 274 (2016).
- [82] J. Qi, *et al.*, [Appl. Phys. Lett.](#) **113**, 043102 (2018).
- [83] J. R. Reimers, S. A. Tawfik, and M. J. Ford, [Chem. Sci.](#) **9**, 7620 (2018).
- [84] L. Seixas, *et al.*, [Phys. Rev. Lett.](#) **116**, 206803 (2016).
- [85] Y. Lai, *et al.*, [Nanoscale](#) **11**, 5163 (2019).

- [86] S. -W. Cheong, *et al.*, [npj Quantum Mater.](#) **3**, 19 (2018).
- [87] D. Lebeugle, *et al.*, [Appl. Phys. Lett.](#) **91**, 022907 (2007).
- [88] K. Yamauchi, P. Barone, and S. Picozzi, [Phys. Rev. B](#) **84**, 165137 (2011).
- [89] Y. S. Oh, *et al.*, [Phys. Rev. B](#) **83**, 060405(R) (2011).
- [90] V. Maisonneuve, V. B. Cajipe, and C. Payen, [Chem. Mater.](#) **5**, 758 (1993).
- [91] V. Maisonneuve, C. Payen, and V. B. Cajipe, [J. Solid State Chem.](#) **116**, 208 (1995).
- [92] V. Maisonneuve, *et al.*, [Ferroelectrics](#) **186**, 257 (1997).
- [93] X. Bourdon, *et al.*, [J. Alloys Compd.](#) **283**, 122 (1999).
- [94] K. Moriya, *et al.*, [Solid State Commun.](#) **136**, 173 (2005).
- [95] K. Taniguchi, *et al.*, [Phys. Rev. Lett.](#) **97**, 097203 (2006).
- [96] L. D. Casto, *et al.*, [APL Materials](#) **3**, 041515 (2015).
- [97] S. Kang, S. Kang, and J. Yu, [J. Electron. Mater.](#) **48**, 1441 (2019).
- [98] V. Carteaux, *et al.*, [J. Magn. Magn. Mater.](#) **94**, 127 (1991).
- [99] M. B. Dines, [Mat. Res. Bull.](#) **10**, 287 (1975).
- [100] R. Brec, *et al.*, [Inorg. Chem.](#) **18**, 7 (1979).
- [101] Z. Lin, *et al.*, [Phys. Rev. Mater.](#) **2**, 051004(R) (2018).
- [102] M. H. Heather, *et al.*, [Phys. Rev. B](#) **99**, 174110 (2019).

# Chapter 7

## Appendix

In this chapter, we present the experimental results which have not been discussed in the main contents.

### 7.1 The additional experiments on the series of the $\text{Co}_2\text{Y}$ -type hexaferrites

#### 7.1.1 Direct ME coupling in the $\text{Ba}_{2-x}\text{Sr}_x\text{Co}_2(\text{Fe}_{1-y}\text{Al}_y)_{12}\text{O}_{22}$ ( $y = 0.04$ and $0.08$ ) series

Fixing not only the Sr ratio to 1.8 ( $\text{Ba}_{0.2}\text{Sr}_{1.8}\text{Co}_2(\text{Fe}_{1-y}\text{Al}_y)_{12}\text{O}_{22}$ ) but also the Al ratio to 0.04 or 0.08 are checked to find the compound which has the largest ME coupling. Thus  $\text{Ba}_{2-x}\text{Sr}_x\text{Co}_2(\text{Fe}_{0.92}\text{Al}_{0.08})_{12}\text{O}_{22}$  and  $\text{Ba}_{2-x}\text{Sr}_x\text{Co}_2(\text{Fe}_{0.96}\text{Al}_{0.04})_{12}\text{O}_{22}$  single crystals are grown by the same method described in the main contents and annealed under oxygen atmosphere.

As a result,  $x=1.7$ -1.8 sample has the biggest ME coupling among  $y = 0.04$  compounds as we expected. In the case of  $y=0.08$  compounds,  $x = 1.3$  specimen show the highest  $dP/dH$  value whereas  $x=1.6$  specimen has the biggest  $\Delta P_{max}$

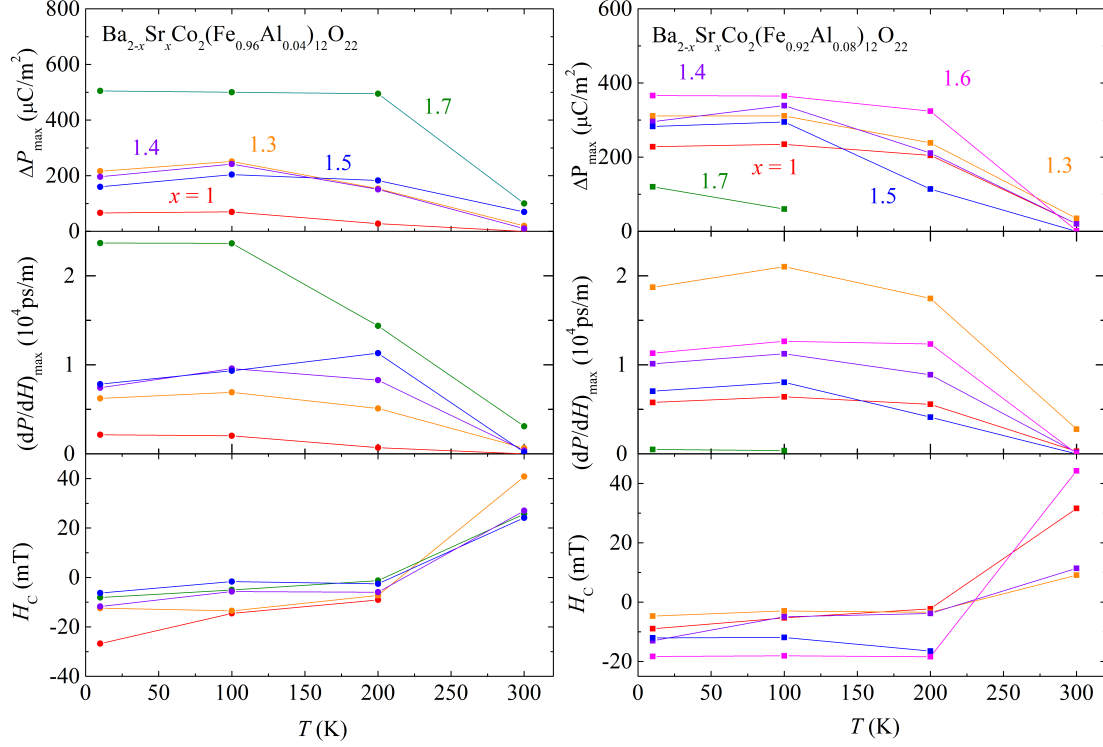


Figure 7.1: Magnetic-field dependent electric polarization of (left)  $\text{Ba}_{2-x}\text{Sr}_x\text{Co}_2(\text{Fe}_{0.96}\text{Al}_{0.04})_{12}\text{O}_{22}$  and (right)  $\text{Ba}_{2-x}\text{Sr}_x\text{Co}_2(\text{Fe}_{0.92}\text{Al}_{0.08})_{12}\text{O}_{22}$  single crystals.  $\Delta P_{\max}$  indicates the difference between extreme values,  $P_{\max} - P_{\min}$  and  $H_c$  indicates the critical magnetic field where  $dP/dH$  is maximum.

because  $x = 1.3$  specimen is softer than  $x = 1.6$  specimen (Note that  $H_c$  is small in  $x = 1.3$  sample). To optimize the ME coupling, enhancement of anisotropy along  $c$ -direction should be achieved with the robust ALC phase, which means that the spin frustration and anisotropy should be properly controlled. Sr- and Al-substitution simultaneously control the frustration and it is likely that a certain optimal  $c/a$  ratio exists for the giant ME coupling. Thus it seems that less amount of Sr-substitution is needed in  $y=0.08$  specimen than  $y=0.04$  specimen because  $c/a$  is already suppressed by large  $y=0.08$ .

### 7.1.2 Magnetostriction of the Co<sub>2</sub>Y-type hexaferrites

Magnetostriction indicates a property that magnetic material changes the dimension by application of the magnetic field. It is a beneficial tool to investigate the motion of the magnetic domain under the magnetic field because the application of the magnetic field is tricky for the XRD or neutron scattering. Here we present the magnetostriction data measured with lab-made dilatometer and strain gauge (KYOWA) utilized in PPMS<sup>TM</sup>.

The dilatometer is a capacitive type with which the change of lattice parameters are estimated by the capacitance values. Capacitance is measured by using the sensitive capacitance bridge, AH2550, with a resolution of 0.01 pF. The dilatometer is only usable for the  $L \parallel H$  configuration. Therefore, the strain gauge is used to measure the  $\Delta L$  perpendicular to the direction of the magnetic field. In this method, the Wheatstone bridge is used. If the sample expands or contracts by an external field, the resistance of strain gauge changes and the balance of Wheatstone bridge collapses. We calculated the  $\Delta L$  by measuring the voltage across the Wheatstone bridge.

Fig. 7.2 shows the in-plane and out-of-plane magnetostriction by the in-plane magnetic field in Ba<sub>0.2</sub>Sr<sub>1.8</sub>Co<sub>2</sub>(Fe<sub>0.96</sub>Al<sub>0.04</sub>)<sub>12</sub>O<sub>22</sub>. The in-plane magnetostriction is increasing rapidly at a low field region and starts to decrease at 0.4 T as the in-plane magnetic field is increasing while the out-of-plane magnetostriction keeps decreasing. In the high field region, the in-plane magnetostriction is almost saturated. The magnetostriction shows hysteresis behavior which is due to the rotating of TC domain as discussed in the magnetic domain imaging study [62]. We could not find any variation by warming the sample which indicates that TC and ALC domains are well-established from the low temperature to room

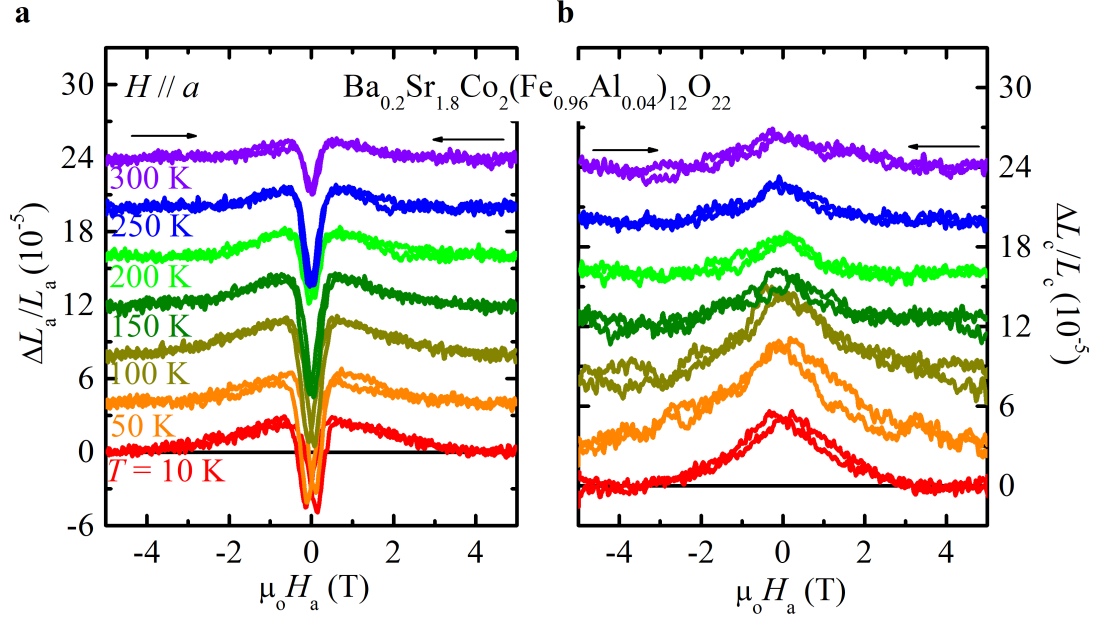


Figure 7.2: (a) In-plane and (b) out-of-plane magnetostriction under magnetic field parallel to in-plane direction in  $\text{Ba}_{0.2}\text{Sr}_{1.8}\text{Co}_2(\text{Fe}_{0.96}\text{Al}_{0.04})_{12}\text{O}_{22}$ .

temperature.

The magnetostriction, magnetization, and electric polarization under the in-plane magnetic field are compared at 10 K in Fig. 7.3. Phase (1) represents the rotation of the TC phase. During the rotation of TC, magnetization is mostly pointing to the tilted direction to the magnetic field so that  $L_a$  is contracting. Under the higher magnetic field above 150 mT, multiple magnetic domains are unified by the external magnetic field and  $L_a$  rapidly increases while polarization is constant (phase 2), supporting that the aligned two distinct TCs with opposite chirality repulse each other. Above 0.4 T,  $L_a$  and  $L_c$  decrease simultaneously by suppressing the domain wall between the two different TCs accompanying to the disappearance of electric polarization because the spin structure changes to be collinear.

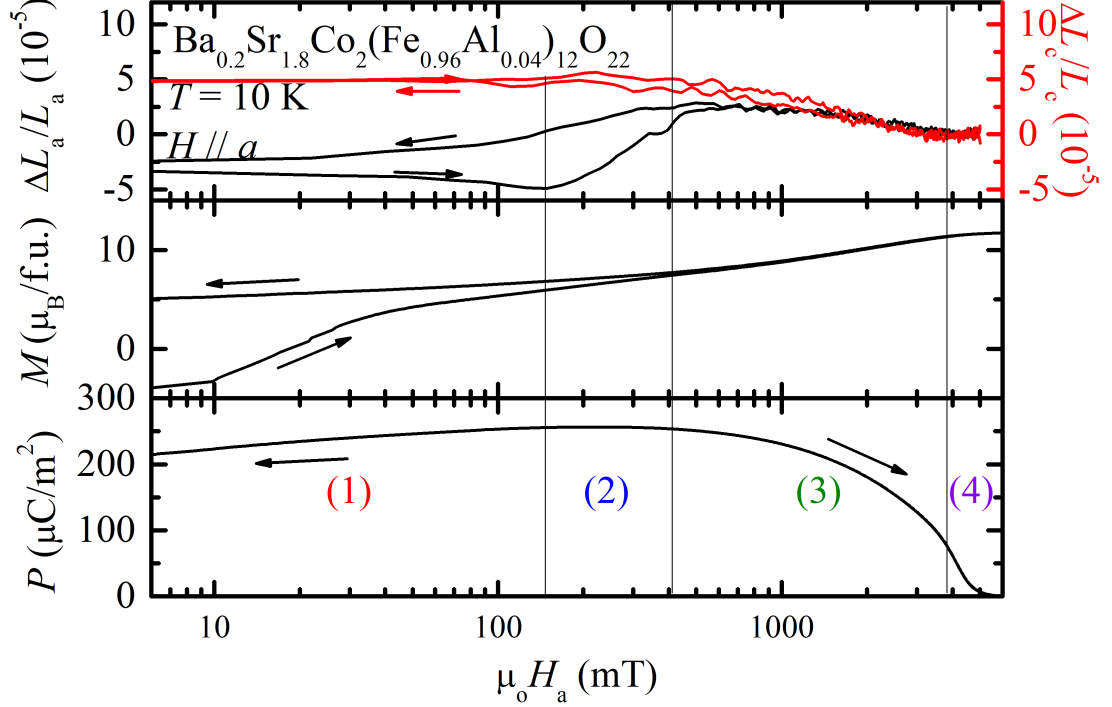


Figure 7.3: Summary of magnetostriction, magnetization, and electric polarization by the in-plane magnetic field in  $\text{Ba}_{0.2}\text{Sr}_{1.8}\text{Co}_2(\text{Fe}_{0.96}\text{Al}_{0.04})_{12}\text{O}_{22}$ .

### 7.1.3 Electric polarization along $c$ -axis induced by the exchange striction mechanism

The alternating longitudinal cone (ALC) phase has a spin ordering with an antiferromagnetic alignment along  $c$ -direction, while the normal longitudinal cone (NLC) phase has a ferromagnetic spin configuration [51]. Therefore, ALC possesses a exotic spin  $\uparrow\uparrow\downarrow\downarrow$  configuration along  $c$ -direction as depicted in Fig. 3.7 and the spin  $\uparrow\uparrow\downarrow\downarrow$  with different charges of the magnetic  $L$  and  $S$  blocks breaks the inversion symmetry, resulting in the ferroelectricity via exchange striction mechanism [66].

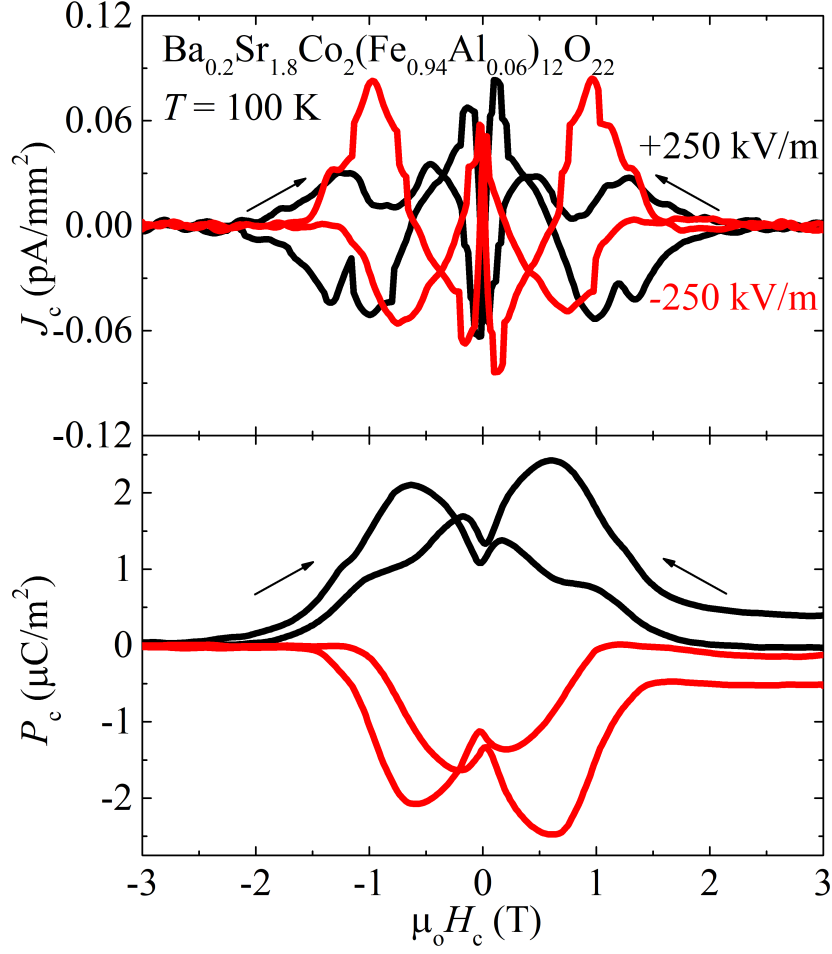


Figure 7.4: (Top) ME current and (Bottom) electric polarization along  $c$ -direction by the application of the magnetization along  $c$ -direction at 100 K in  $\text{Ba}_{0.2}\text{Sr}_{1.8}\text{Co}_2(\text{Fe}_{0.94}\text{Al}_{0.06})_{12}\text{O}_{22}$ .

Fig. 7.4 show the The emergence of polarization along  $c$ -direction at 100 K in  $\text{Ba}_{0.2}\text{Sr}_{1.8}\text{Co}_2(\text{Fe}_{0.94}\text{Al}_{0.06})_{12}\text{O}_{22}$ . The region of ferroelectricity corresponds to that of the ALC phase. It is clearly seen in Fig. 7.5 that the polarization increase as increasing the temperature, indicating that evolution of the ALC phase at the low magnetic field induces the out-of-plane polarization.

To prove that TC phase is most-stabilized in  $y=0.04$ , we performed the mea-



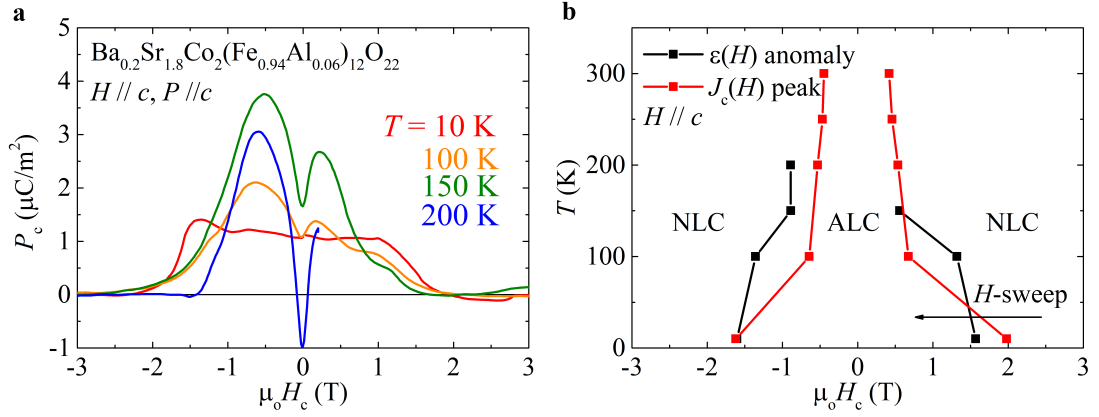


Figure 7.5: (a) Electric polarization along  $c$ -direction and (b) phase diagram constructed from the dielectric constant and ME current measurement in  $\text{Ba}_{0.2}\text{Sr}_{1.8}\text{Co}_2(\text{Fe}_{0.94}\text{Al}_{0.06})_{12}\text{O}_{22}$ .

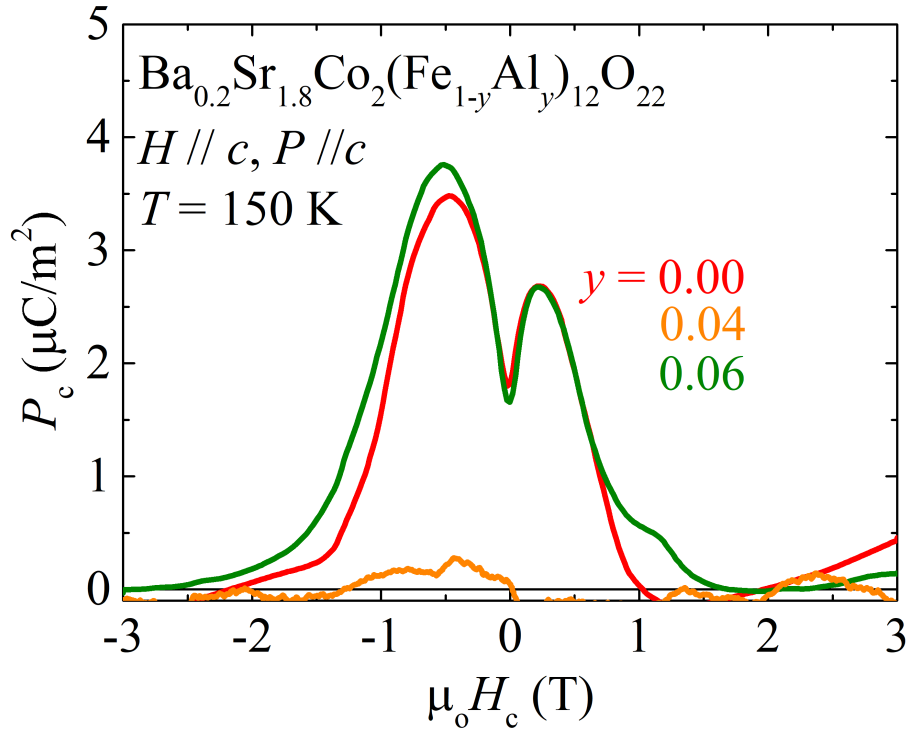


Figure 7.6: Electric polarization along  $c$ -direction by the application of the magnetization along  $c$ -direction at 150 K in  $\text{Ba}_{0.2}\text{Sr}_{1.8}\text{Co}_2(\text{Fe}_{1-y}\text{Al}_y)_{12}\text{O}_{22}$ .

surement with  $\text{Ba}_{0.2}\text{Sr}_{1.8}\text{Co}_2(\text{Fe}_{1-y}\text{Al}_y)_{12}\text{O}_{22}$  samples. Fig. 7.6 shows that the  $P_c$  is not observed in  $y = 0.04$  compound at 150 K, whereas specimens with  $y = 0.00$  and 0.06 have finite magnetic field-induced  $P_c$  values. It demonstrates that TC phase dominantly exists in  $\text{Ba}_{0.2}\text{Sr}_{1.8}\text{Co}_2(\text{Fe}_{0.96}\text{Al}_{0.04})_{12}\text{O}_{22}$  at relatively high temperature, 150 K, even though magnetic field is low. It also supports that the highest ME effect originated from the control of the free energy barrier,  $\Delta E_{\text{barrier}}$  in  $\text{Ba}_{0.2}\text{Sr}_{1.8}\text{Co}_2(\text{Fe}_{0.96}\text{Al}_{0.04})_{12}\text{O}_{22}$ .

## 7.2 Studies on the ME coupling in the CoZnY-type hexaferrites single crystal

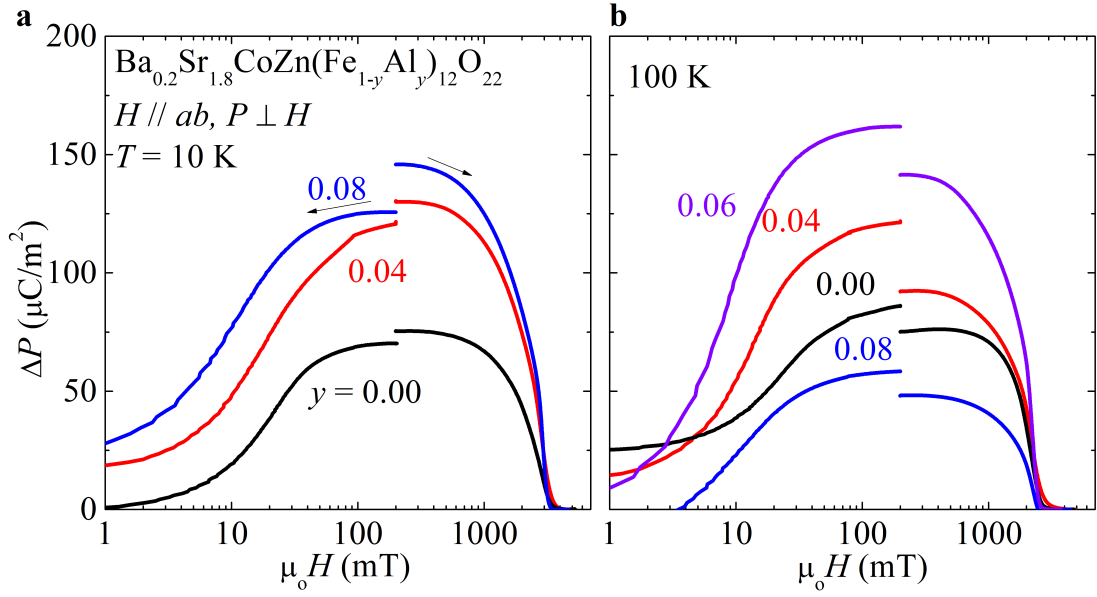


Figure 7.7: (a) Magnetic-field dependent electric polarization of  $\text{Ba}_{2-x}\text{Sr}_x\text{CoZn}(\text{Fe}_{1-y}\text{Al}_y)_{12}\text{O}_{22}$  single crystals at 10 K and 150 K.

$\text{Co}_2\text{Y}$ -type hexaferrites have a higher coercivity than  $\text{Zn}_2\text{Y}$ -type hexaferrites even though  $\text{Co}_2\text{Y}$ -type hexaferrites shows huge ME coupling up to room temperature. It is likely that the high coercivity comes from the strong magnetic anisotropy along  $c$ -direction due to the substitution of cobalt to the octahedral sites. The hexaferrite materials open a new route to realize the novel devices, such as multi-bit memory, if a soft hexaferrite ( $H_c < 1\text{ mT}$ ) with giant ME coupling ( $dP/dH > 25,000\text{ ps/m}$ ) is discovered at room temperature. Here, we chose  $\text{Ba}_{0.2}\text{Sr}_{1.8}\text{CoZn}(\text{Fe}_{1-y}\text{Al}_y)_{12}\text{O}_{22}$  single crystal as a target to control the coercive field. Zinc ions substitute to the tetrahedral sites and do not affect magnetic

anisotropy, while partial cobalt ions control the magnetic anisotropy in the octahedral site. We expected that the moderate cobalt-doping enhances the ME coupling by stabilizing the TC phase and the coercive field remains suitably low.

Fig. 7.7 displays the results. Overall  $P$  vs  $H$  curves are similar to  $\text{Co}_2\text{Y}$ - and  $\text{Zn}_2\text{Y}$ -type hexaferrites cases, meaning that Zn- and Co-doping do not affect the ME coupling via the inverse DM interaction. Fig. 7.8 summarize the results and shows that magnetic field-induced polarization is optimized in the  $\text{Ba}_{0.2}\text{Sr}_{1.8}\text{CoZn}(\text{Fe}_{0.94}\text{Al}_{0.06})_{12}\text{O}_{22}$ . Note that the optimal Al doping ratio  $y$  is 0.04 and 0.08 in  $\text{Co}_2\text{Y}$ -type and  $\text{Zn}_2\text{Y}$ -type hexaferrites, respectively. As discussed in the main content, a certain optimal  $c/a$  ratio exists for the giant ME coupling and  $y=0.06$  seems to correspond to the certain value in the  $\text{CoZnY}$ -type hexaferrites.

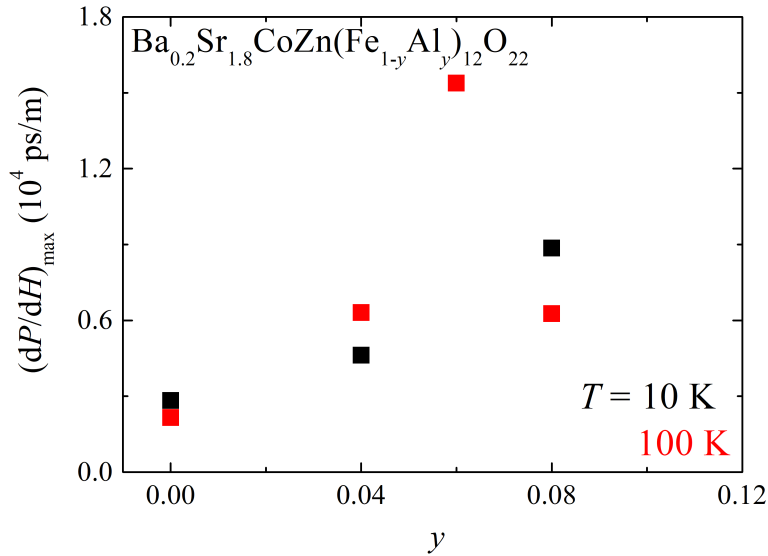


Figure 7.8: The summary of magnetic field-induced polarization at 10 K and 150 K in  $\text{Ba}_{0.2}\text{Sr}_{1.8}\text{CoZn}(\text{Fe}_{1-y}\text{Al}_y)_{12}\text{O}_{22}$ .

### 7.3 Studies on the ME coupling in the $\text{Co}_2\text{Z}$ -type hexaferrites $\text{Ba}_{3-x}\text{Sr}_x\text{Co}_2\text{Fe}_{24}\text{O}_{41}$ poly crystals

The realization of giant ME coupling at room temperature provides significant advantages in multifunctional applications such as multi-bit memory and non-dissipative spintronic devices. Other than Y-type hexaferrite, Z- and U-type hexaferrites show ME effect at room temperature [24,67]. It is known that the TC phase is spontaneously existing in the  $\text{Co}_2\text{Z}$ -type hexaferrites [47,68] and induce the ME coupling via spin-dependent  $p$ - $d$  hybridization mechanism at room temperature [58]. The TC phase of Z-type hexaferrite also can be tailored by Ba/Sr

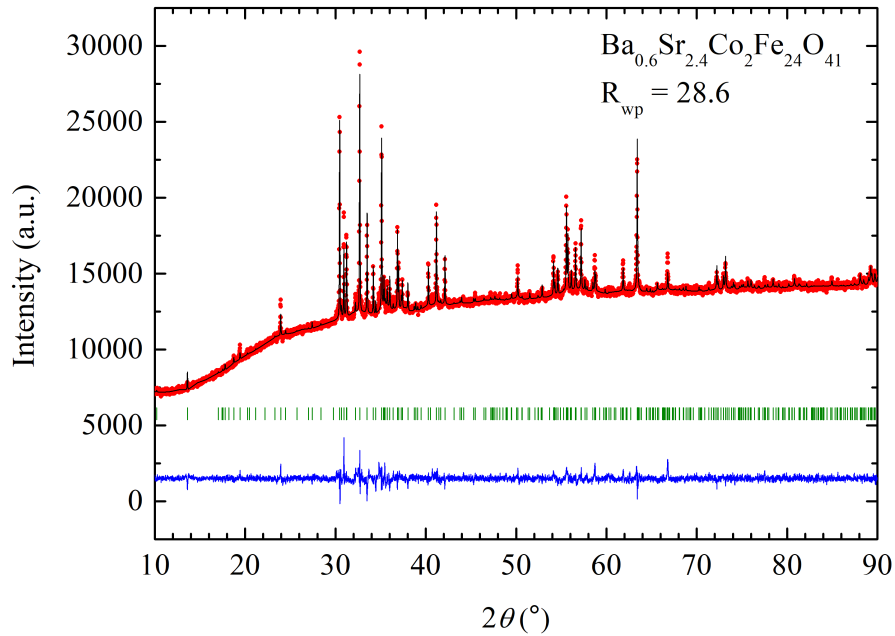


Figure 7.9: An X-ray diffraction pattern of  $\text{Ba}_{3-x}\text{Sr}_x\text{Co}_2\text{Fe}_{24}\text{O}_{41}$  poly crystals and its Rietveld refinement result.

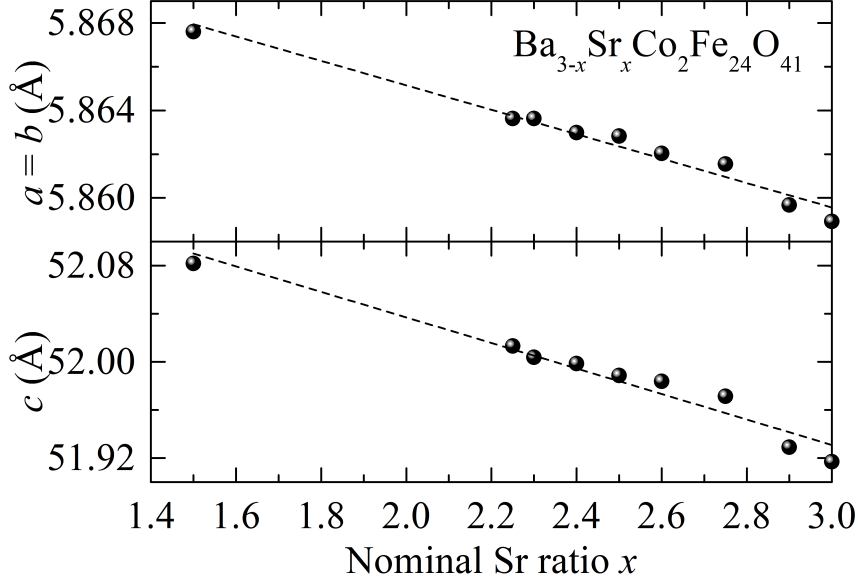


Figure 7.10: The evolution of  $a$ - and  $c$ -axis lattice constants with Sr  $x$  substitution ratio as determined from the X-ray diffraction data and the Rietveld refinement result of  $\text{Ba}_{3-x}\text{Sr}_x\text{Co}_2\text{Fe}_{24}\text{O}_{41}$  poly crystals.

because the smaller ionic radius of Sr cation deforms the bonding nature around the interface between magnetic  $L$  and  $S$  block and makes the spin frustration enhanced, as suggested in the Y-type hexaferrites.

In particular, we found that  $\text{Co}_2\text{Z}$ -type hexaferrite  $\text{Ba}_{0.52}\text{Sr}_{2.48}\text{Co}_2\text{Fe}_{24}\text{O}_{41}$  single crystal shows large ME coupling at room temperature with the ME susceptibility  $(dP/dH) \sim 3200$  ps/m, the highest value at room temperature among the known single-phase ME materials [47]. To investigate the evolution of ME coupling strength with the variation of Ba and Sr ratio, we have synthesized a series of high quality polycrystalline  $\text{Ba}_{3-x}\text{Sr}_x\text{Co}_2\text{Fe}_{24}\text{O}_{41}$  ( $1.5 < x < 3.0$ ) by solid-state reaction methods. XRD data in Fig. 7.9 indicates that the sample has high purity and lattice constant follows the Vegard's law (Fig. 7.10). The poly crystals were annealed in an oxygen atmosphere to guarantee the high resistance

7.3. Studies on the ME coupling in the  $\text{Co}_2\text{Z}$ -type hexaferrites  
 $\text{Ba}_{3-x}\text{Sr}_x\text{Co}_2\text{Fe}_{24}\text{O}_{41}$  poly crystals

---

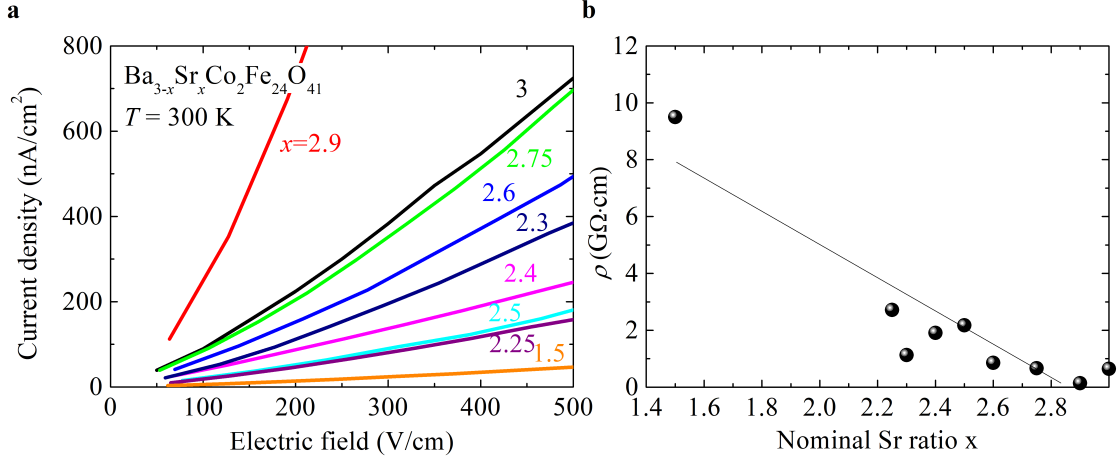


Figure 7.11: (a) Voltage driven by the electric current with two-probe method at 300 K in  $\text{Ba}_{3-x}\text{Sr}_x\text{Co}_2\text{Fe}_{24}\text{O}_{41}$ . (b) Summary of the resistivity at 300 K in  $\text{Ba}_{3-x}\text{Sr}_x\text{Co}_2\text{Fe}_{24}\text{O}_{41}$  poly crystals.

as shown in Fig. 7.11.

The resistivity of the samples is enough to apply the poling electric field and the AC ME susceptibility measurement tool was used to investigate the ME effect in  $\text{Ba}_{3-x}\text{Sr}_x\text{Co}_2\text{Fe}_{24}\text{O}_{41}$  poly crystals. Fig. 7.12 shows that  $\text{Ba}_{0.6}\text{Sr}_{2.4}\text{Co}_2\text{Fe}_{24}\text{O}_{41}$  specimen has the largest ME susceptibility of 380 ps/m and the electric polarization of  $17 \mu\text{C}/\text{m}^2$  is clearly larger than that of  $\text{Sr}_3\text{Co}_2\text{Fe}_{24}\text{O}_{41}$ . The origin of such enhanced ME coupling at the specific doping can be explained by the variation of superexchange interaction in the frustrated spin network, in analogy to the previous results in the  $\text{Zn}_2\text{Y}$ -type hexaferrites [21]. Further studies on the transition of the magnetic structure as a function of Sr ratio  $x$  are needed such as neutron scattering and magnetization measurement.

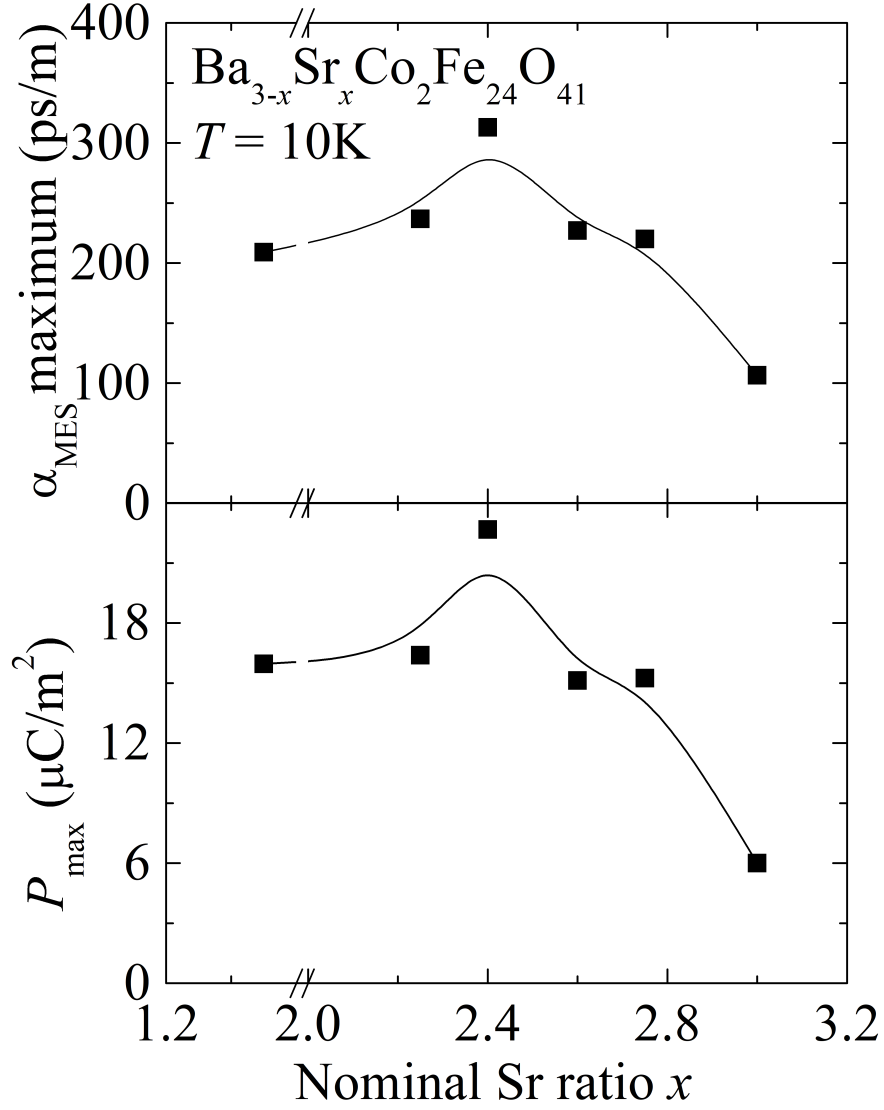


Figure 7.12: Summary of the maximum  $dP/dH$  and  $P$  as a function of Sr ratio  $x$  at 10 K, demonstrating that the specimen with  $x = 2.4$  has the largest magnetic field induced polarization in  $\text{Ba}_{3-x}\text{Sr}_x\text{Co}_2\text{Fe}_{24}\text{O}_{41}$  poly crystals.



## 7.4 Studies on the hybrid improper ferroelectricity in $(\text{Ba},\text{Sr},\text{Ca})_3\text{Sn}_2\text{O}_7$

Hybrid improper ferroelectricity (HIF) induce an electric polarization by the hybridization of the rotating and tilting mode of the octahedron in perovskite structure [70,71]. Perovskite structure has an infinite potential for the novel states and application, thus the discovery of huge polarization in perovskite structure is of importance. The HIF is a new type of ferroelectricity which was not observed before so that HIF is being spotlighted [69].

N. A. Benedek *et al.* first suggested the HIF ferroelectricity mechanism in  $n=2$  Ruddlesden-Poppers structure by two consecutive rotating mode theoretically [70]. Also, it is experimentally proven in 2015 by Y. S. Oh *et al.* [69]. They claim that the large cations in the perovskite ( $P$ ) block and small cations in the rocksalt ( $R$ ) block induce a big polarization and low switching energy in  $n=2$  Ruddlesden-Poppers structure [71]. The site preference results in the modulation of orthorhombicity  $(b-a)/(b+a)$  which enhances the rotating and tilting mode.

To investigate the HIF in the  $(\text{Ba}, \text{Sr}, \text{Ca})_3\text{Sn}_2\text{O}_7$  with  $n=2$  Ruddlesden-

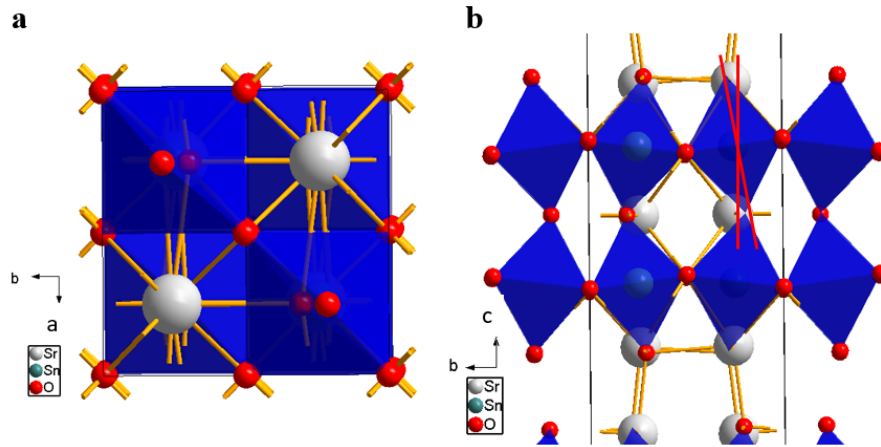


Figure 7.13: Crystal structure of  $\text{Sr}_3\text{Sn}_2\text{O}_7$  projected onto (a)  $ab$ -plane and (b)  $bc$ -plane.

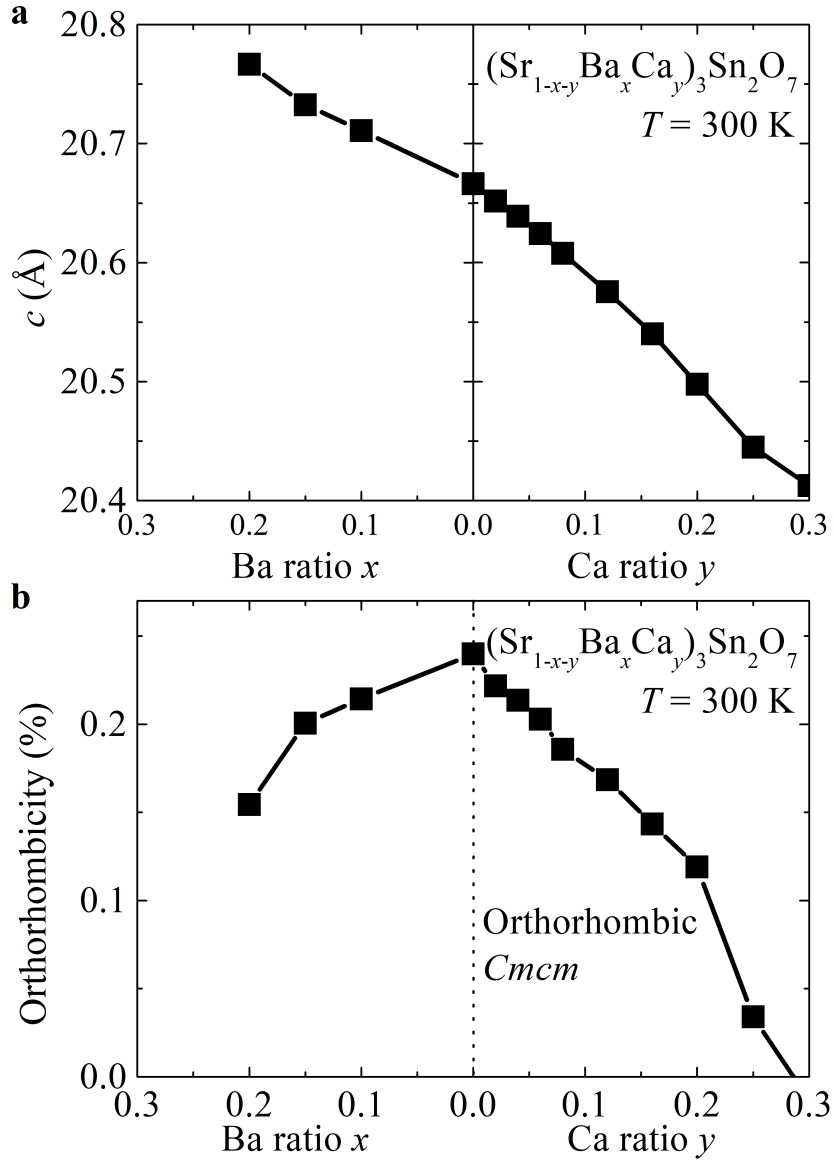


Figure 7.14: (a) The evolution of  $c$ -axis lattice constants with Ba substitution  $x$  and Ca substitution  $y$  ratio calculated from the the Rietveld refinement of  $(\text{Ba},\text{Sr},\text{Ca})_3\text{Sn}_2\text{O}_7$  poly crystals. (b) Orthorhombicity  $(b-a)/(b+a)$  as a function of  $x$  and  $y$ .

Poppers structure, we grew the poly crystal with solid-state reaction method. The structure of  $\text{Sr}_3\text{Sn}_2\text{O}_7$  is exhibited in Fig. 7.13.  $\text{Sr}_3\text{Sn}_2\text{O}_7$  has a centrosymmetric  $Cmcm$  space group and we systematically substituted the Ba and Ca cations to

the Sr sites to make a noncentrosymmetric  $A2_1$  space group. Fig. 7.14 displays the lattice constant along  $c$ -direction and orthorhombicity  $(b - a)/(b + a)$ . It demonstrates that Ba and Ca substitutions rather decrease the orthorhombicity, even though the enhanced orthorhombicity is needed to induce the structural transition to the centrosymmetric space group. Therefore, Ba and Ca are relaxing the distortion of the octahedron, so that tetragonal structure is stabilized other than orthorhombic structure.

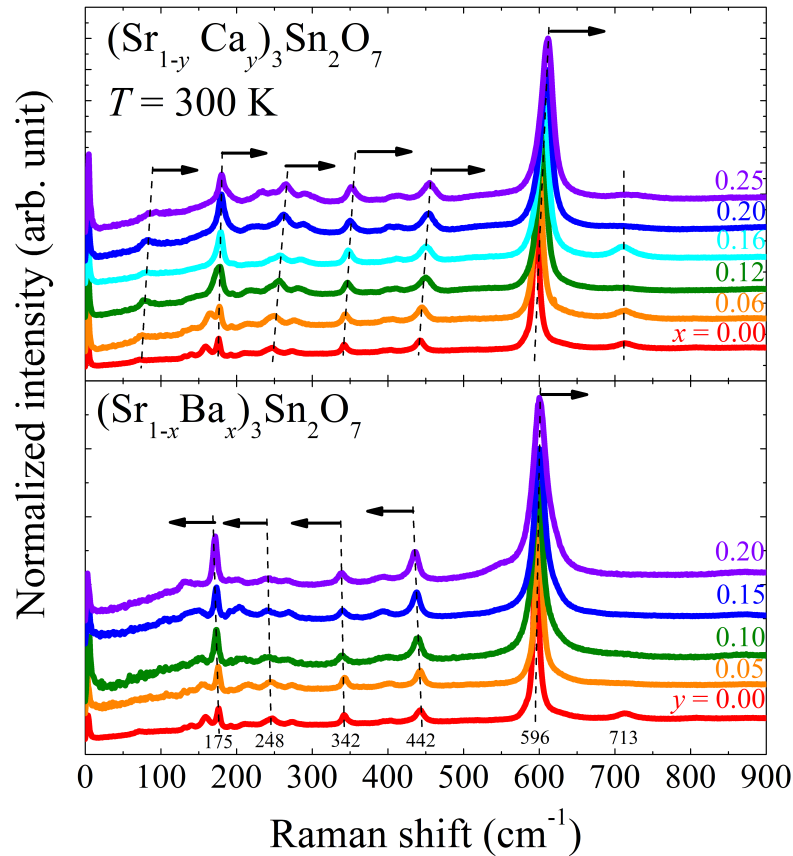


Figure 7.15: Raman shift of (top)  $(\text{Sr}_{1-y}\text{Ca}_y)_3\text{Sn}_2\text{O}_7$  and (bottom)  $(\text{Sr}_{1-x}\text{Ba}_x)_3\text{Sn}_2\text{O}_7$  at 300 K

The origin of the suppressed-orthorhombicity is discussed in this section. Fig. 7.15 presents the Raman shift of  $(\text{Sr}_{1-y}\text{Ca}_y)_3\text{Sn}_2\text{O}_7$  and  $(\text{Sr}_{1-x}\text{Ba}_x)_3\text{Sn}_2\text{O}_7$  at 300 K. As Ca (Ba) atom with an atomic mass of 40.08  $u$  (137.33  $u$ ), the Raman mode shifts on the right (left) side, respectively because the light  $\text{Ca}^{2+}$  makes vibrational frequency get larger.  $710\text{ cm}^{-1}$  mode does not depend on Ca or Ba substitution probably because the mode is relevant to the Sn-O-Sn bonding. However, we found that the  $596\text{ cm}^{-1}$  only moves to a higher frequency when  $x$  and  $y$  are increasing. The high frequency mode is known as the octahedral stretching mode [72–74].

If large cation  $\text{Ba}^{2+}$  prefers to enter the  $R$  block site, then  $P$  block contracts and distance between Sn-O increases so that the vibrational frequency gets harder. On the other hand, small cation  $\text{Ca}^{2+}$  preferring to enter the  $P$  block also shrinks  $P$  block resulting in the same effect with Ba substitution as depicted in Fig. 7.16. XRD result in Fig. 7.17 indicates that small cation in the  $P$  block and large cation in the  $R$  exhibit the better  $R_{up}$  values.

Ferroelectric properties are investigated by the  $P$  vs  $E$  curve and dielectric

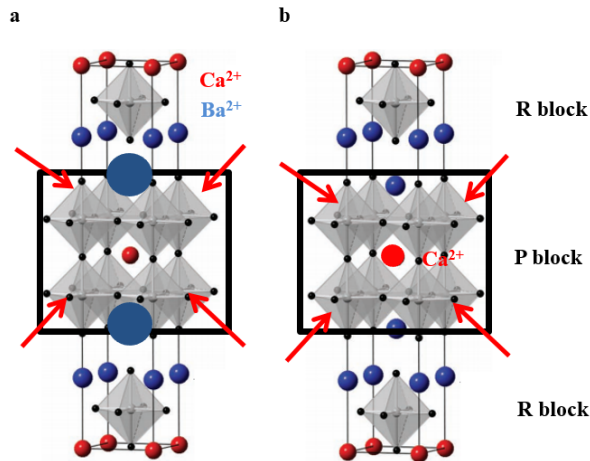


Figure 7.16: The schematic illustration of R-block contraction by selectively substitution of (a) Ba and (b) Ca in  $(\text{Ba,Sr,Ca})_3\text{Sn}_2\text{O}_7$  at 300 K

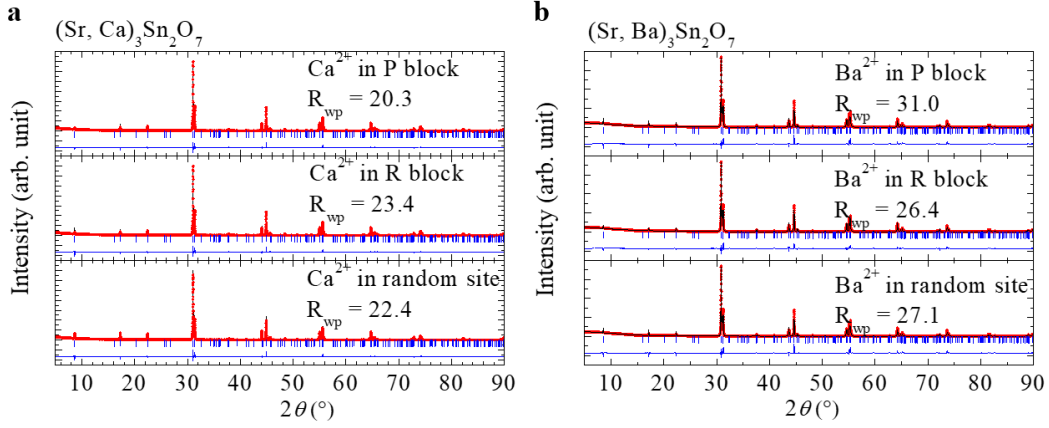


Figure 7.17: The XRD data fitted by the Rietveld refinement by assuming that cations are preferring specific site in (a)  $(\text{Sr}_{1-y}\text{Ca}_y)_3\text{Sn}_2\text{O}_7$  and (b)  $(\text{Sr}_{1-x}\text{Ba}_x)_3\text{Sn}_2\text{O}_7$ .

constant measurement. The  $P$  vs  $E$  curve measurement was performed by Sawyer-Tower method and the dielectric constant was measured in the closed cycle refrigeration system at  $10 \text{ K} < T < 300 \text{ K}$  and in the tube furnace with the lab-made

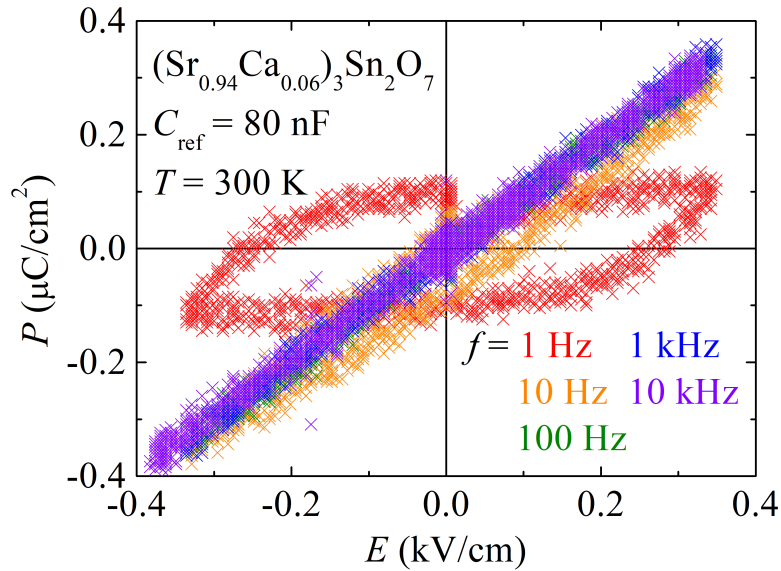


Figure 7.18: Polarization induced by the external electric field measured with the various frequency in  $(\text{Sr}_{0.94}\text{Ca}_{0.06})_3\text{Sn}_2\text{O}_7$  at 300 K. Capacitance of the reference is 80 nF and the Sawyer-Tower method with single-loop is used.

probe at  $300 \text{ K} < T < 600 \text{ K}$ . Fig. 7.18 and Fig. 7.19 depict the  $P$  vs  $E$  curve and temperature-dependent dielectric constant, respectively. As the frequency increase, the ellipse shape changes to the linear shape because the leakage current decreases. It shows the polarization has a linear response to the external electric field, indicating the paraelectricity. To check the existence of the ferroelectric transition as a function of temperature, we tried dielectric constant measurement. However, we could not find any evidence of the ferroelectric transition from 10 K to 600 K [?], which is consistent with suppression of orthorhombicity by the site preference of  $\text{Ba}^{2+}$  and  $\text{Ca}^{2+}$ .

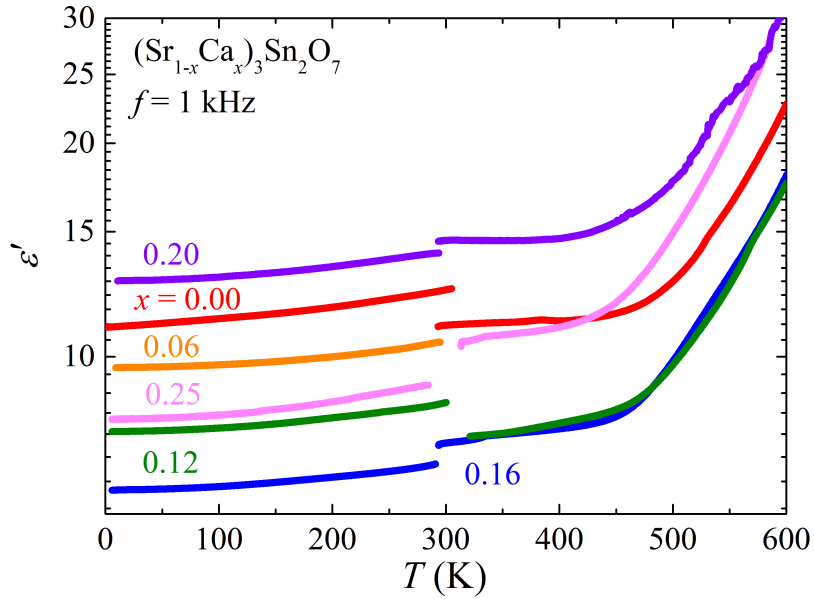


Figure 7.19: Temperature-dependent ( $10 \text{ K} < T < 600 \text{ K}$ ) dielectric constant of  $(\text{Sr}_{1-x}\text{Ca}_x)_3\text{Sn}_2\text{O}_7$ . The excitation frequency is 1 kHz.

## 7.5 Investigation of the topological quantum state via lithium intercalation in a 2D ferromagnet $\text{CrSiTe}_3$

Two-dimensional insulator  $\text{CrSiTe}_3$  has layered honeycomb structure which exhibits a paramagnet (PM) to ferromagnet (FM) transition at 33 K [96]. Recent theoretical calculation predicts that the transition-metal trichalcogenide with chemical formula  $\text{ABX}_3$  (A is transition metal, B is Si, Ge or Sn, and X is chalcogen) can realize magnetic Chern insulator because of its topologically non-trivial nature of its band structure and time reversal symmetry breaking [97]. Herein, we present our recent effort to induce a metallic state in  $\text{CrSiTe}_3$  by lithium ion ( $\text{Li}^+$ ) intercalation and application of hydrostatic pressure. Single crystal pieces of  $\text{CrSiTe}_3$  were dipped into the n-butyllithium solution and the evolution of their electrical resistance with time was monitored. We found that the room temperature resistivity,  $\rho_{300K}$ , of most metallic specimens decreased by four orders of magnitudes and, at the same time, ferromagnetic moment along  $c$ -axis also decreased by 15%. Hall effect measurements reveal an increase of carrier concentration, suggesting that the  $\text{Li}^+$  provides free carriers into the Van der Waals layers. Upon application of hydrostatic pressure, we also observed a metal-insulator transition in a  $\text{Li}_x\text{CrSiTe}_3$  single crystal at 2.57 GPa. Furthermore, longitudinal magneto-resistance (MR) changes negative to positive around 1.46 GPa, indicating the spin reorientation with pressure. The amount of  $\text{Li}^+$  intercalation has not been enough yet to induce metallic behavior at ambient pressure, but various  $\text{Li}^+$  intercalation method and experimental progress will be presented.

### 7.5.1 Sample preparation

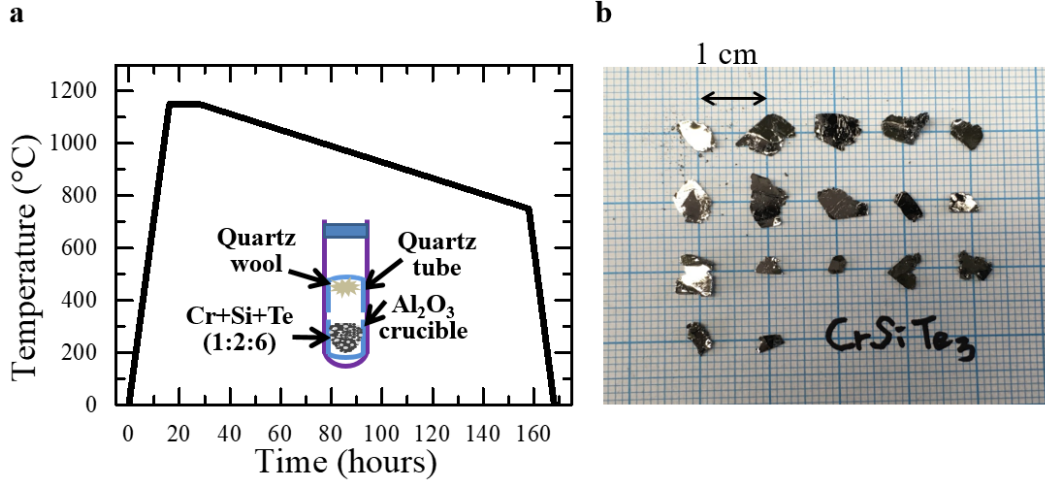


Figure 7.20: (a) Temperature sequence and pictorial illustration of how CrSiTe<sub>3</sub> single crystal is prepared. [96] (b) Real image of CrSiTe<sub>3</sub> single crystals .

CrSiTe<sub>3</sub> single crystal is grown by flux-method. Te powder is used as a self-flux. Cr, Si, and Te powders are weighed with 1:2:6 ratio in the glove box. The mixed powder is transferred to the Al<sub>2</sub>O<sub>3</sub> crucible, sealed inside the quartz tube and put inside box furnace with the temperature sequence described in Fig. 7.20 [96] (a). After the sequence is finished, the remaining flux is removed by the centrifuge. The prepared sample is displayed in the 7.20 (b). We successfully got a CrSiTe<sub>3</sub> single crystal with a size of 1cm × 1cm × 0.2 ×. XRD peaks are also well-assigned to (00L) with the known structure ( $R\bar{3}$  space group) [98].

Li<sup>+</sup> ions are intercalated by the following two methods. First, CrSiTe<sub>3</sub> single crystal is dipped into the n-butyllithium solution. After a few days, the crystal is taken out and cleaned in the pure hexane. This method has widely been used in the various dichalcogenide samples [99,100]. We set up the real-time intercalation monitoring system and found that the resistance of the single crystal is decreasing



7.5. Investigation of the topological quantum state via lithium intercalation in a 2D ferromagnet  $\text{CrSiTe}_3$

---

as the dipping time in the n-Butyllithium passes (Fig. 7.21). After the reaction for 4 days, the resistance of the sample was low enough to measure the resistance and Hall effect.

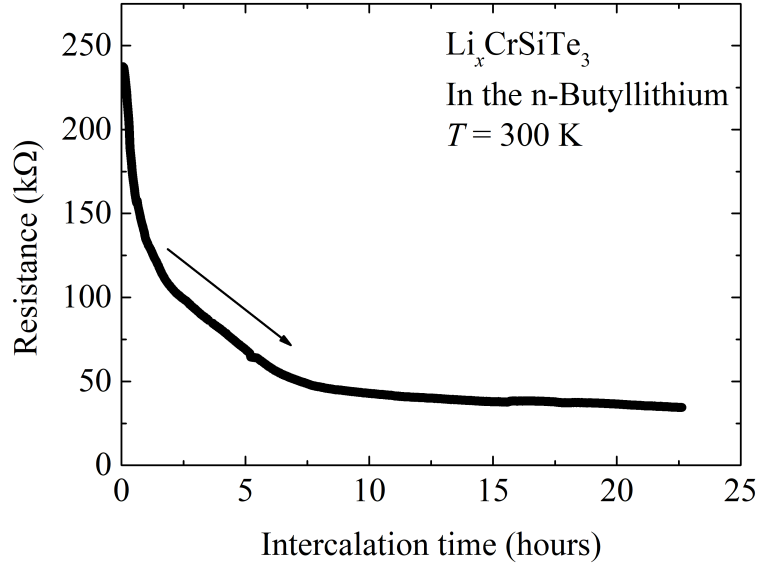


Figure 7.21: Variation of resistance of the  $\text{CrSiTe}_3$  single crystal as a function of time in the n-Butyllithium.

Fig. 7.23 exhibits the comparison between the magnetization and resistivity of the  $\text{Li}_x\text{CrSiTe}_3$ . The magnetic moment along  $c$ -axis is suppressed to 90 % after the Li intercalation. Furthermore, resistivity clearly shows the shoulder at ferromagnetic transition,  $T_c = 33$  K. The anomaly of the resistivity is presumably originated from the correlation of electrons accompanying to FM order. Hall effect results in Fig. 7.22 claims that the major carrier is a hole and the carrier density is  $\sim 4 \times 10^{17} \text{ cm}^{-3}$  at 300 K.

The second method is performed with liquid ammonia. Gas ammonia is generated from the neutral reaction between  $\text{NH}_4\text{Cl}$  and  $\text{KOH}$ . The gas ammonia flows to the bath of the dry ice and is liquefied (Fig. 7.24). Li metal is dissolved

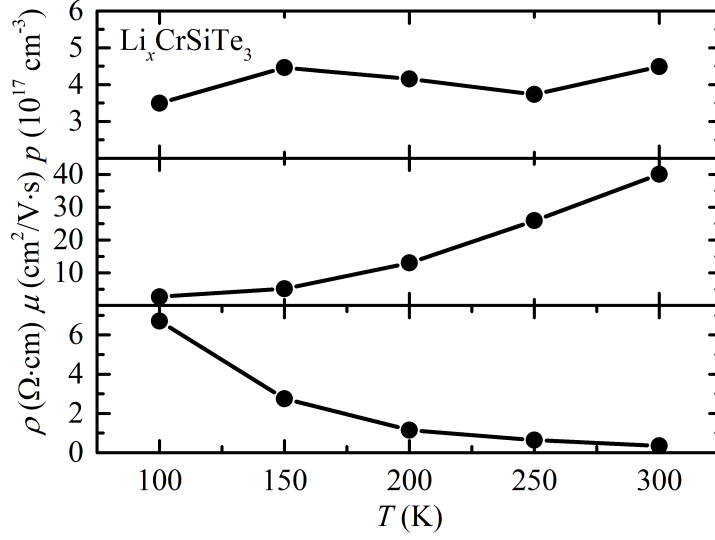


Figure 7.22: Hole carrier density, mobility, and resistivity as a function of temperature from 100 K to 300 K in  $\text{Li}_x\text{CrSiTe}_3$ .

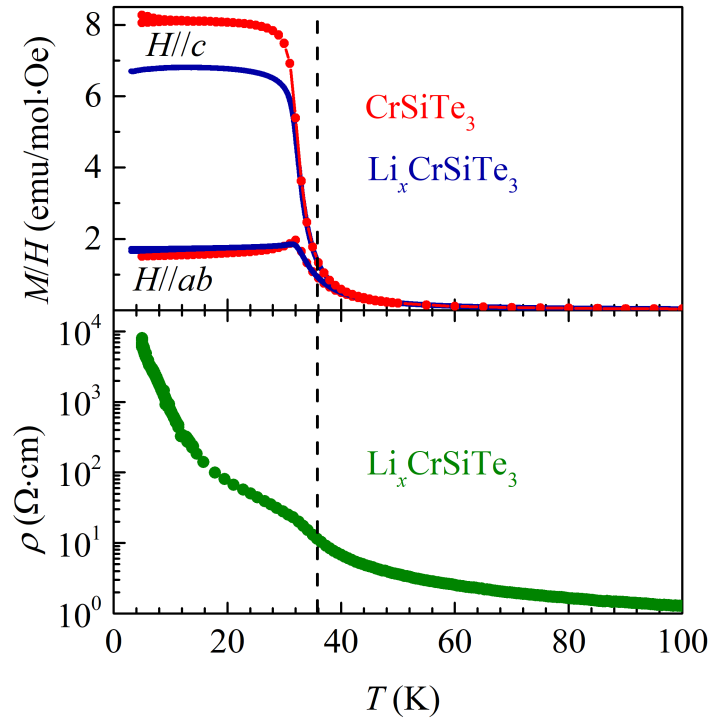


Figure 7.23: Temperature-dependent (top) magnetization and (bottom) resistivity in the  $\text{CrSiTe}_3$  and  $\text{Li}_x\text{CrSiTe}_3$ .

7.5. Investigation of the topological quantum state via lithium intercalation in a 2D ferromagnet  $\text{CrSiTe}_3$

---

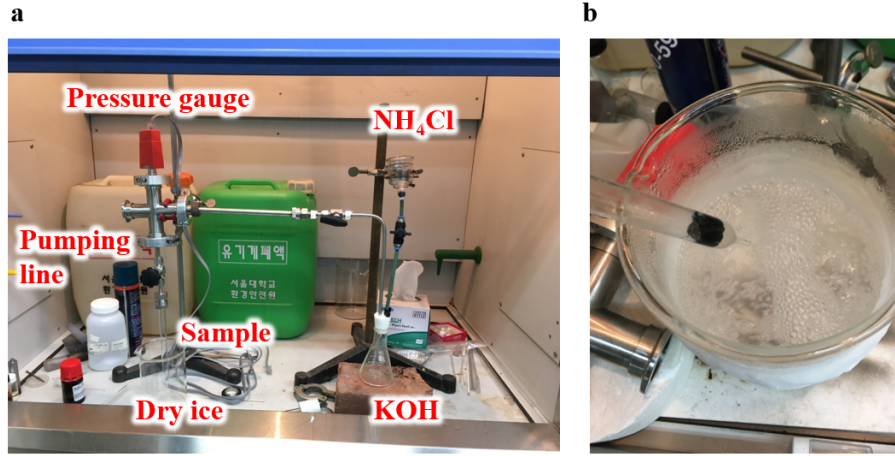


Figure 7.24: (a) The set-up for liquefying the ammonia and the intercalation of  $\text{Li}^+$  ion. (b) The dissolving Li metal into the liquid ammonia.

into the liquid ammonia and ionized to  $\text{Li}^+$ . The  $\text{Li}^+$  ions are absorbed and intercalated into the  $\text{CrSiTe}_3$  layer. Not only Li but also K and Na metals are tested as sources of intercalation. The result is displayed in Fig. 7.25. After the intercalation,  $\text{Na}^+$  is the most effective ion to make the  $\text{CrSiTe}_3$  metallic among alkali metals by decreasing the resistivity (smaller than 1 order of resistivity of pristine  $\text{CrSiTe}_3$ ). However, the ammonia method generally introduces the lower carriers than n-butyllithium method in our experiment.

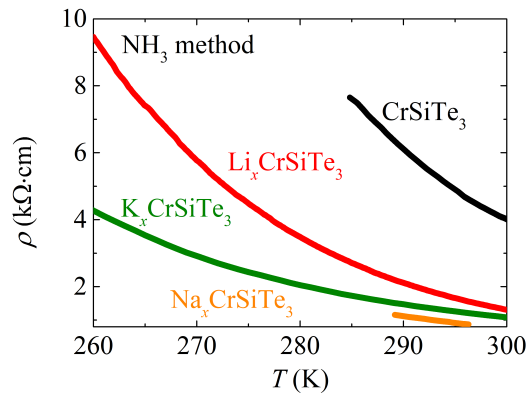


Figure 7.25: Resistivity of the alkali metal-intercalated  $\text{CrSiTe}_3$  single crystal below room temperature.

### 7.5.2 Metal-insulator transition under high pressure

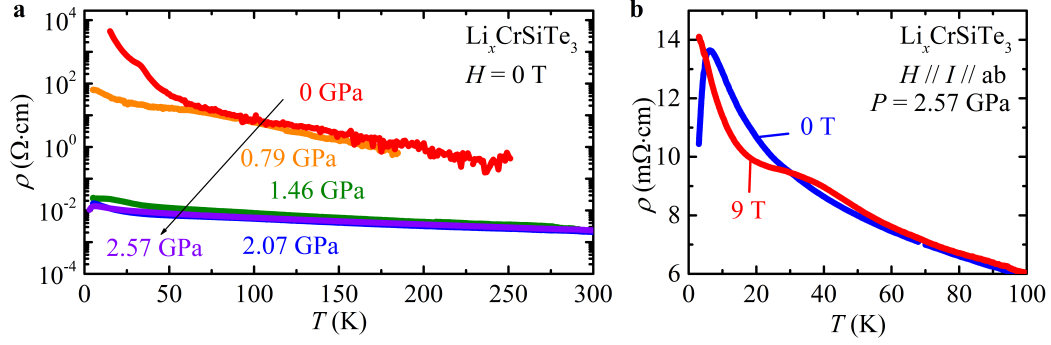


Figure 7.26: (a) Temperature-dependent resistivity of the  $\text{Li}_x\text{CrSiTe}_3$  single crystal under hydrostatic pressure ( $0 \text{ GPa} \leq P \leq 2.57 \text{ GPa}$ ) at the zero field. (b) Temperature-dependent resistivity in 2.57 GPa at 0 T (blue line) and 9 T (red line).

To investigate the topological quantum state by controlling the electronic band structure, we applied hydrostatic pressure to the  $\text{Li}_x\text{CrSiTe}_3$  single crystal with piston cell. Fig. 7.26 (a) shows the temperature dependence of resistivity under high pressure without the magnetic field. As the external pressure increases, resistivity is systematically reduced. Interestingly, the metal-insulator transition (MIT) is observed at 2.57 GPa. Furthermore, the MIT disappears under the magnetic field as shown in Fig. 7.26 (b). Magnetoresistance (MR) at 10 K and 30 K are exhibited in Fig. 7.27. At low pressure, the resistivity decreases with the application of the magnetic field because spin-spin interaction is suppressed. The negative MR changes to the positive MR above 0.79 GPa. The crossover of the positive to negative MR can be explained by spin reorientation [101].

The variation of resistivity in  $\text{Cr}(\text{Si}_{1-x}\text{As}_x)\text{Te}_3$  single crystals is briefly introduced in Fig. 7.28.

7.5. Investigation of the topological quantum state via lithium intercalation in a 2D ferromagnet  $\text{CrSiTe}_3$

---

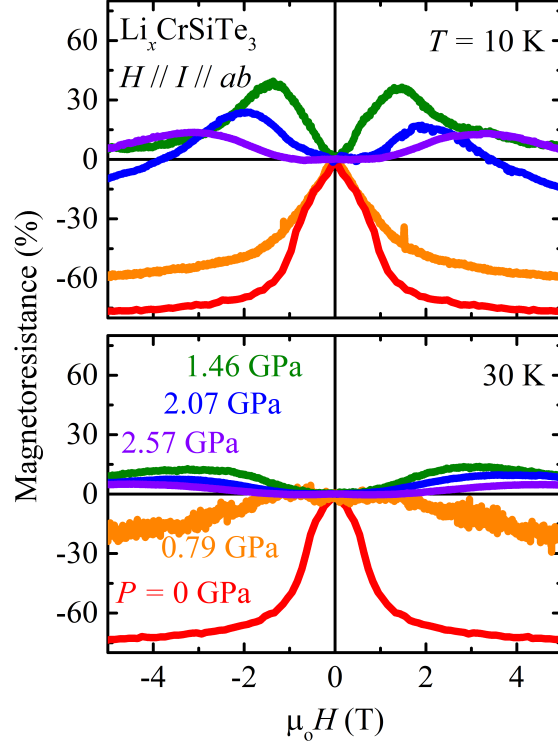


Figure 7.27: Magnetic field-dependent resistivity of the  $\text{Li}_x\text{CrSiTe}_3$  single crystal under hydrostatic pressure at (top) 10 K and (bottom) 30 K.

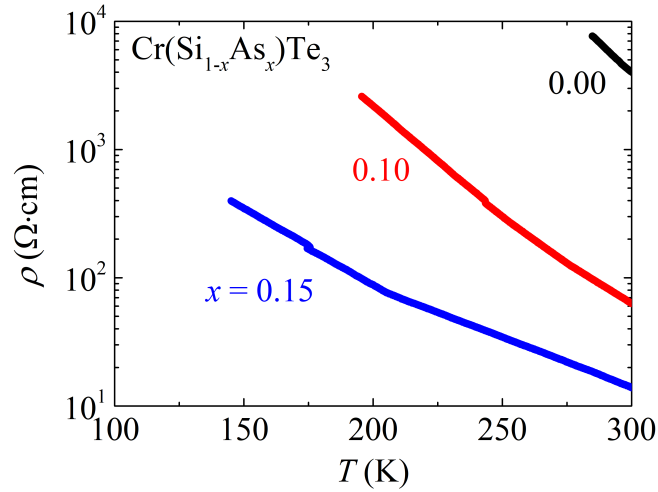


Figure 7.28: Temperature dependence of resistivity in the  $\text{Cr}(\text{Si}_{1-x}\text{As}_x)\text{Te}_3$  single crystals.

## 7.6 The preparation of X-ray diffraction at low temperature

To measure the X-ray diffraction at low temperatures from 13 K to 300 K, low temperature cryostat, PheniX from the Oxford Cryosystems, and closed cycle

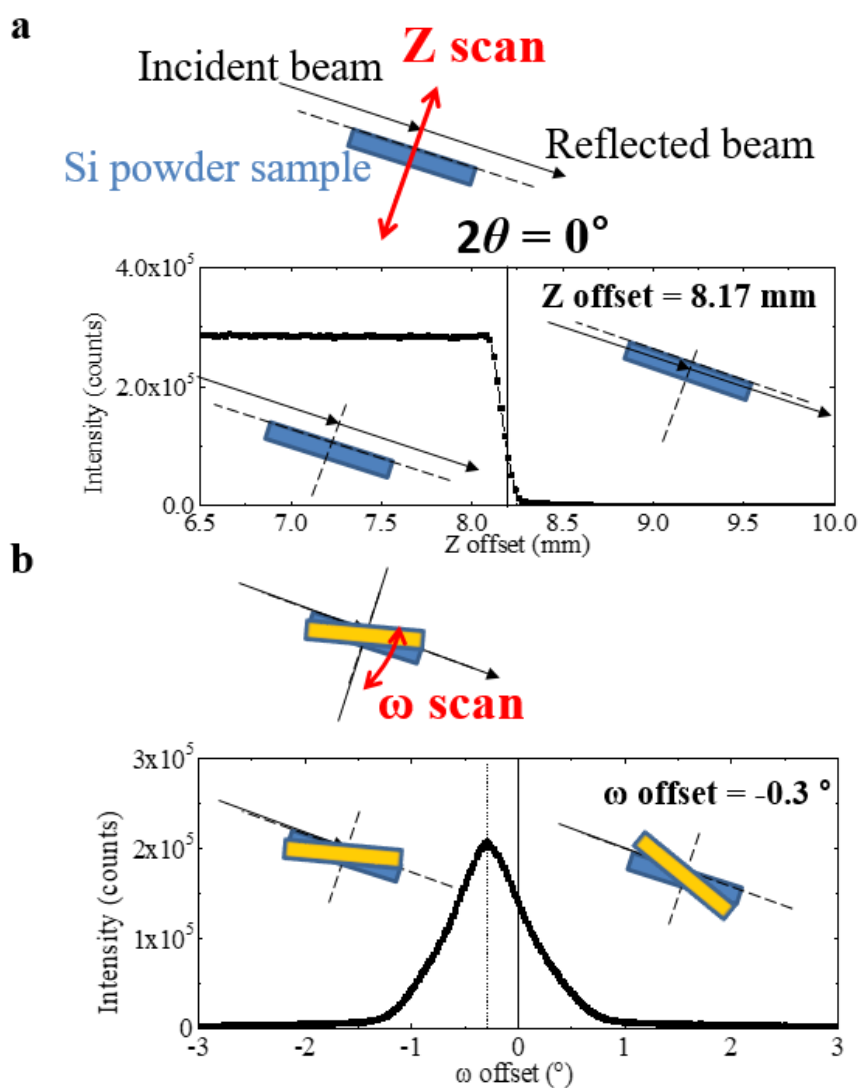


Figure 7.29: a) Z scan and (b)  $\omega$  scan to align the sample position in the cryostat.

### 7.6. The preparation of X-ray diffraction at low temperature

refrigeration system which is embedded in XRD machine (Malvern Panalytical) is utilized. First, prepare the sample in a powder form and load on the holder. It is always better to use a large amount of powder to make a diffracted area wider and achieve a higher diffraction signal. One can use copper blocks to spread powder out to cover the wider area with a limited amount of the sample. Then connect the cryostat to the sample stage and mount the prepared powder. Before covering the lid of the cryostat, one should align the sample position properly. Use a Copper beam mask in front of the detector to protect it from the direct incident beam and then start Z scan. As shown in Fig. 7.29 (a), detected intensity shows step-like feature and the Z offset is the position of the step, 8.17 mm. Subsequently, perform  $\omega$  scan after entering the Z offset in software, then find the  $\omega$  offset,  $-0.3^\circ$ , (Fig.7.29(b)). The Z and  $\omega$  offset values are varying every time depending on how one mounts the powder on the holder. Thus the alignment process should proceed before measurement.

Now pump the cryostat after covering the radiation shield and lid of the cryostat and turn on the compressor. The lowest temperature our machine reaches

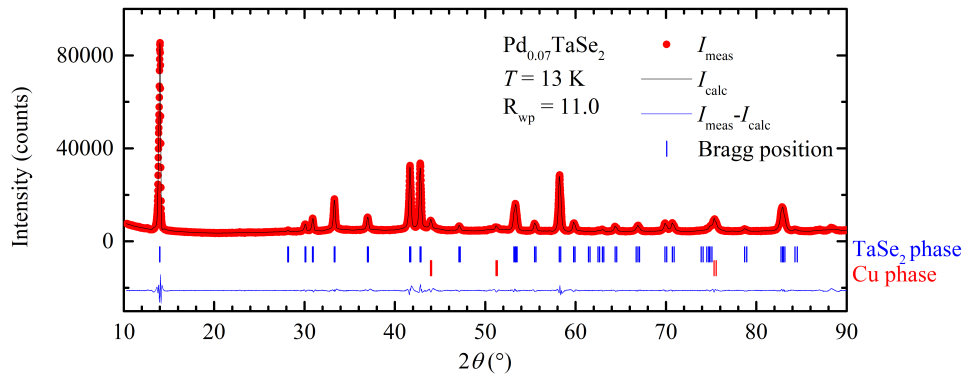


Figure 7.30: XRD result analyzed by profiling fitting of  $\text{Pd}_{0.07}\text{-TaSe}_2$  at 13 K.  $R_{\text{wp}}$  is 11.0.

is 13 K. Fig. 7.30 displays the one example of the XRD data measured at a low temperature with our machine. We could get a good signal with the high intensity even though it is measured for 10 minutes. Fig. 7.31 summarizes the thermal coefficient along  $c$ -direction  $c^{-1}dd/dT$  at the various temperature and shows that mostly follow the Debye model. The thermal coefficient decreases as cooling the sample and it shows a sudden increase at 30 K. The dip-like feature is consistent with the commensurate charge density wave (CCDW) transition with the expansion of the lattice predicted by the density functional theory [102].

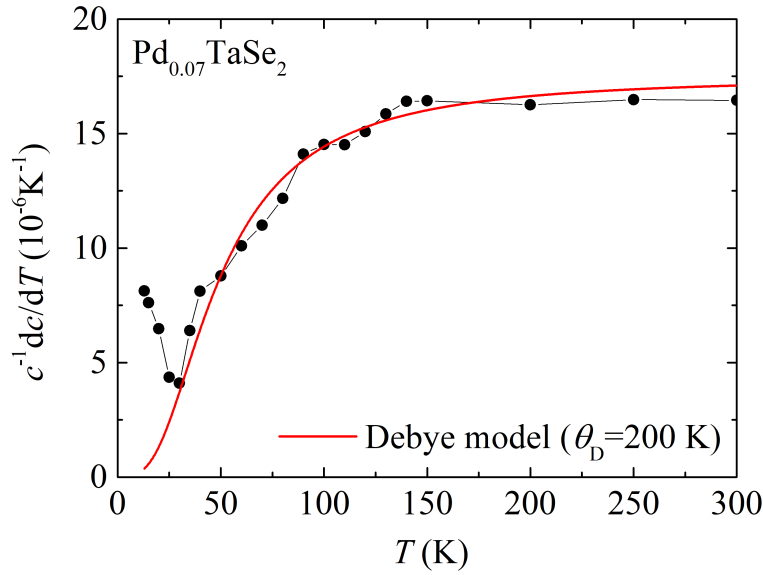


Figure 7.31: Summary of the thermal coefficient of  $\text{Pd}_{0.07}\text{-TaSe}_2$  along  $c$ -direction as a function of temperature. The red line follows the Debye fitting with  $\theta_D = 200$  K.

Fig. 7.32 also introduces another example of the XRD data measured at low temperatures with our machine.



7.6. The preparation of X-ray diffraction at low temperature

---

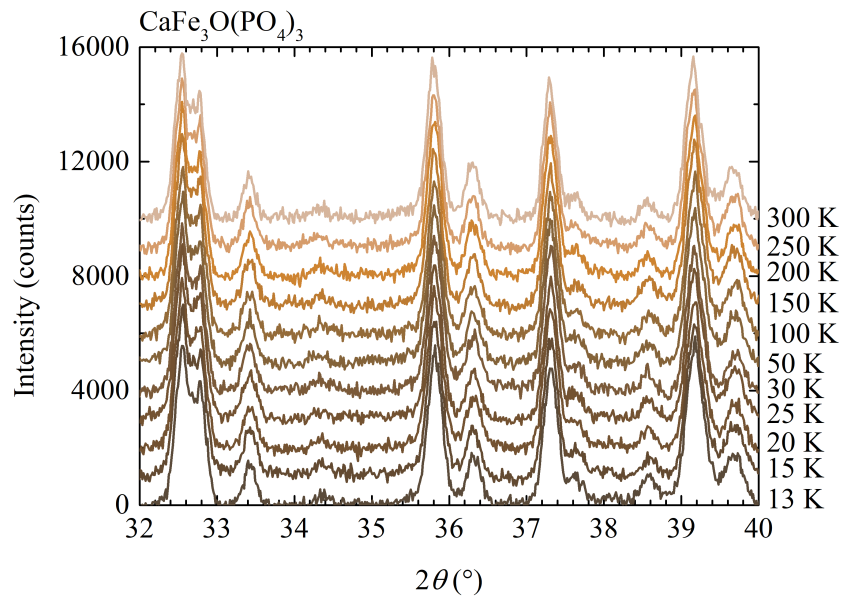


Figure 7.32: XRD results of  $\text{CaFe}_3\text{O}(\text{PO}_4)_3$  at  $13 < T < 300$  K.

# Chapter 8

## Publication List

### 8.1 List of publications

1. *Optimized magnetoelectric coupling from from fine control of magnetic anisotropy in the  $Co_2Y$ -type hexaferrites*

**C. B. Park**, K. W. Shin, S. H. Chun, J. H. Lee, Y. S. Oh, W. -S. Noh, S. M. Disseler, C. A. Heikes, W. D. Ratcliff, J. -H. Park, and K. H. Kim  
*Submitted to Proc. Natl. Acad. Sci.*

2. *Discovery of magnetoelectric coupling in a van der Waals compound  $CuCrP_2S_6$*

**C. B. Park**, A. Shahee, D. R. Patil, N. T. -Oganessian, and K. H. Kim  
*In preparation*

3. *Interactions in the bond-frustrated helimagnet  $ZnCr_2Se_4$  investigated by NMR*

S. Park, S. Kwon, S. Lee, S. Khim, D. Bhoi, **C. B. Park**, and K. H. Kim  
[Sci. Rep. \*\*9\*\*, 16627 \(2019\).](#)

4. *Electric dipoles via  $Cr^{3+}$  ( $d^3$ ) ion off-center displacement in perovskite  $DyCrO_3$*

L. H. Yin, T. F. Shi, R. R. Zhang, **C. B. Park**, K. H. Kim, J. Yang, P. Tong, W. H. Song, J. M. Dai, X. B. Zhu, W. S. Yan, and Y. P. Sun  
[Phys. Rev. B \*\*98\*\*, 054301 \(2018\).](#)

### 8.1. List of publications

---

5. *Fe and Co NMR studies of magnetoelectric Co<sub>2</sub>Y-type hexaferrite BSCFAO*  
B. Choi, S. Kwon, **C. B. Park**, K. W. Shin, K. H. Kim, and S. Lee  
[J. Phys. Condens. Matter \*\*30\*\*, 065802 \(2018\).](#)
6. *Optical Properties of GaFeO<sub>3</sub>*  
T. J. Kim, H. G. Park, V. L. Le, H. S. Kim, C. H. Yoo, H. U. Kim,  
**C. B. Park**, K. Shin, K. H. Kim, and Y. D. Kim  
[Sci. Adv. Mater. \*\*130\*\*, 302-307 \(2018\).](#)
7. *Role of rare earth in the magnetic, magnetocaloric and magnetoelectric properties of RCrO<sub>3</sub> (R=Dy, Nd, Tb, Er) crystals*  
L. H. Yin, J. Y., P. Tong, X. Luo, **C. B. Park**, K. W. Shin, W. H. Song,  
J. M. Dai, K. H. Kim, X. B. Zhu, and Y. P. Sun  
[J. Mater. Chem. C \*\*4\*\*, 11198 \(2016\).](#)
8. *Pressure-induced ferroelectricity and enhancement of Mn-Mn exchange striction in GdMn<sub>2</sub>O<sub>5</sub>*  
L. H. Yin, D. H. Jang, **C. B. Park**, K. W. Shin and K. H. Kim  
[J. Appl. Phys. \*\*119\*\*, 104101 \(2016\).](#)
9. *Giant suppression of phononic heat transport in a quantum magnet BiCu<sub>2</sub>PO<sub>6</sub>*  
B. -G. Jeon, B. Koteswararao, **C. B. Park**, G. J. Shu, S. C. Riggs, E. G.  
Moon, S. B. Chung, F. C. Chou and K. H. Kim  
[Sci. Rep. \*\*6\*\*, 36970 \(2016\).](#)

## Chapter 9

### Korean abstract

## 국문 초록

# Co<sub>2</sub>Y-타입 육방정계 철산화물 Ba<sub>2-x</sub>Sr<sub>x</sub>Co<sub>2</sub>(Fe<sub>1-y</sub>Al<sub>y</sub>)<sub>12</sub>O<sub>22</sub>과 이차원 반데르발스 물질 CuCrP<sub>2</sub>X<sub>6</sub> (X=S, Se)의 자기전기효과에 관한 연구

강자성과 강유전성이 공존하는 다강체 물질과 두 현상이 강하게 상호작용하는 자기전기성체는 그 진기한 과학적 기작뿐만 아니라 멀티비트 메모리와 같은 산업의 응용 가능성 때문에 오랫동안 연구되어 왔다. 지금까지 다양한 다강체 및 자기전기성체가 발견되었지만, 아직 상온 혹은 저차원에서 강한 자기전기효과를 갖는 물질은 흔하지 않다. 특히 상온 혹은 저차원에서 강한 자기전기효과를 갖는 물질의 발견은 나노스케일의 차세대 소자를 구현하는데 굉장히 중요하다. 본 학위 논문에서는 자기전기성체의 응용범위를 넓히기 위하여 상온 자기전기성체 Co<sub>2</sub>Y-타입 육방정계 철산화물 Ba<sub>2-x</sub>Sr<sub>x</sub>Co<sub>2</sub>(Fe<sub>1-y</sub>Al<sub>y</sub>)<sub>12</sub>O<sub>22</sub>과 이차원 반데르발스물질 CuCrP<sub>2</sub>X<sub>6</sub> (X=S, Se)의 자기전기효과에 대해 연구하였다.

Co<sub>2</sub>Y-타입 육방정계 철산화물의 자기전기효과를 극대화하기 위해 바륨(Ba)과 철(Fe) 자리에 스트론튬(Sr)과 알루미늄(Al)을 치환하여 단결정을 성장하였다. 성장시킨 단결정의 자성, 강유전성 및 자기전기성 측정을 통해 물리적 기작을 탐구하였다. 그 결과 스트론튬과 알루미늄이 치환된 모든 물질군에서 황형원뿔스핀구조와 반복종형원뿔스핀구조가 공존하는 것을 확인하였고 그 둘의 비율이 온도 및 자기장 조건에 굉장히 민감하다는 것을 발견하였다. 황형원뿔스핀구조는 주로 저온에서 자기장이 인가되었을 때 안정적인 반면 반복종형원뿔스핀구조는 고온에서 안정적임을 관찰하였다. 특히 스트론튬 비율  $x = 1.8$ , 알루미늄 비율  $y = 0.04$ 이 치환된 시료에서 황형원뿔스핀구조가 가장 안정하며 자기장에 의해 발현되는 전기분극의 변화가 상온에서  $60 \mu\text{C}/\text{m}^2$ , 10 K에서  $430 \mu\text{C}/\text{m}^2$ 로 가장 큰 값을 갖는 것이 확인되었다. 이 결과는 스트론튬과 알루미늄 치환을 통하여 자기비등방성과 교환 상호작용을 조절하고 황형원뿔스핀구조를 안정하게 하는 것이 육방정계 철산화물의 상온 자기전기효과를 극대화하는데 매우 중요함을 시사한다.

두 번째로 구리(Cu), 크로뮴(Cr), 인(P) 쌍이 벌집구조를 이루고 있는 이차원

반데르발스 물질  $\text{CuCrP}_2\text{S}_6$  단결정에서의 자기전기효과에 대하여 보고한다. 자성과 전기분극 측정을 통해 자기장에 의해 조절되는 전기분극을 존재하는 것을 확인하였고 전기분극이 크로뮴의 반강자성정렬에 의해 유도되는 것을 규명하였다. 결과적으로 자기전기 상평형도를 얻었고 그 원리에 대하여 보고하였다. 더 나아가  $\text{CuCrP}_2\text{Se}_6$  물질과의 비교를 통해 전기분극은 크로뮴의 황 팔면체 자리에서의 비중심성에 기인하는  $p$ - $d$  혼성 궤도 메커니즘에 의한 것을 확인하였다. 대칭성 분석을 통하여 성공적으로 자기장 대 전기분극 곡선 및 자기장 회전에 따른 전기분극의 개형을 이해할 수 있었다. 위 결과는 전이금속의 팔면체 자리에서의 비중심성이 저차원 자기전기효과를 구현할 수 있음을 처음으로 시사하였다.

---

· **키워드:** 다강체, 자기전기성체, 강유전체, 육방정계 철산화물, 반데르발스 물질

· **학번:** 2013-20369

## Chapter 10

### Acknowledgements





